

**Optical properties of
3-port-grating coupled cavities**

Von der Fakultät für Mathematik und Physik
der Gottfried Wilhelm Leibniz Universität Hannover
zur Erlangung des Grades

Doktor der Naturwissenschaften
– Dr. rer. nat. –

genehmigte Dissertation
von

Dipl.-Phys. Oliver Burmeister

geboren am 26. Mai 1978 in Hannover

2010

Referent:	Prof. Dr. Roman Schnabel
Korreferent:	Prof. Dr. Karsten Danzmann
Tag der Promotion:	05.01.2010

Abstract

In the past few years, an international network of laser interferometric gravitational wave detectors has been developed. These detectors are currently operating at sensitivities which allow for a direct detection of gravitational waves caused by astrophysical events, such as a nearby supernovae explosions.

A promising technique proposed to improve the sensitivity of future detectors is the replacement of the transmitting optical components of the interferometer by all-reflective alternatives based on reflection gratings. By using all-reflective components, thermal problems due to the residual absorption inside the substrate material can be reduced. One approach uses a low-efficiency grating in 2nd order Littrow mount to replace the partly transmissive coupling mirror of a Fabry-Perot resonator. In contrast to a conventional coupling mirror, this device couples an incoming beam into three instead of two output ports. Consequently the phase relations between input and output ports depend on the diffraction efficiencies of the 3-port-grating.

In this work a theoretical description of a generic 3-port component based on the scattering matrix formalism is given. Furthermore the implications of the derived phase relations on cavities based on binary and thereby symmetrical 3-port-gratings are analyzed analytically as well as experimentally. The commonly used techniques for length sensing and control of cavities are extended to 3-port-grating cavities. In contrast to a conventional mirror, a translational displacement of a grating parallel to its surface in direction perpendicular to the grating grooves will induce a phase shift proportional to the diffraction order. The coupling of this additional noise source is investigated theoretically and the noise coupling to the length sensing signal is verified experimentally. For this experiment a fully suspended 10 m long grating cavity at the University of Glasgow was used. The properties of two resonators coupled by a 3-port-grating are investigated with regard to an application in a power recycling configuration in theory and experiment. Finally a configuration is proposed that allows the use of 3-port-grating cavities with the technique of resonant sideband extraction.

Keywords: Gravitational-wave detectors, diffraction gratings, optical resonators

Kurzfassung

In den vergangenen Jahren ist ein internationales Netzwerk von laser-interferometrischen Gravitationswellendetektoren entstanden. Die Detektoren haben eine Empfindlichkeit erreicht, die es ermöglicht Gravitationswellen astrophysikalische Ereignisse, wie nahegelegene Supernova-Explosionen, zu detektieren. Eine vielversprechende Möglichkeit, die Empfindlichkeit zukünftiger Detektoren zu erhöhen, beinhaltet den Austausch der transmissiven optischen Komponenten des Interferometers durch reinreflektive Alternativen basierend auf Reflektionsgittern. Die Verwendung von reinreflektiven Komponenten ermöglicht eine Reduzierung der absorptionsbedingten thermischen Probleme im Inneren der Substrate.

Ein Ansatz zieht die Verwendung von niedereffizienten Gittern in 2. Ordnung Littrow Konfiguration in Betracht, um den Einkoppelspiegel eines Fabry-Perot Resonators zu ersetzen. Im Gegensatz zu einem konventionellen Spiegel, spaltet diese Komponente einen eintreffenden Strahl in drei anstatt zwei Teilstrahlen auf. Daraus ergibt sich, dass die Phasenbeziehungen zwischen Ein- und Ausgängen der Komponente von den Beugungseffizienzen des 3-Port Gitters abhängen.

Im Rahmen dieser Arbeit wird eine theoretische Beschreibung einer allgemeinen 3-Port Komponente basierend auf dem Streumatrixformalismus präsentiert. Des Weiteren werden die Auswirkungen dieser Phasenbeziehungen auf das Verhalten von Resonatoren, die ein binäres und somit symmetrisches 3-Port Gitter als Einkoppler verwenden, sowohl analytisch als auch experimentell untersucht. Die bisher benutzten Techniken zur Längenstabilisierung von Resonatoren wird auf 3-Port Gitterresonatoren übertragen. Im Gegensatz zu herkömmlichen Spiegeln, bewirkt eine Verschiebung des Gitters parallel zur Oberfläche einen Phasenversatz proportional zur Beugungsordnung. Die Kopplung dieser zusätzlichen Rauschquelle wird theoretisch untersucht, und die Kopplung des Rauschens in das Längenstabilisierungssignal experimentell überprüft. Für dieses Experiment wurde ein aufgehängter 10 m langer Gitterresonator an der Universität Glasgow benutzt. Die Eigenschaften von zwei Resonatoren, welche durch ein 3-Port Gitter miteinander gekoppelt sind, wird im Hinblick auf eine mögliche Anwendung in einer „Power-Recycling“-Konfiguration in Theorie und Experiment untersucht. Abschließend wird eine Topologie vorgeschlagen, welche es ermöglicht 3-Port Gitterresonatoren in einer „Resonant-Sideband Extraction“-Konfiguration zu nutzen. **Schlagwörter:** Gravitationswellendetektoren, Beugungsgitter, optische Resonatoren

Contents

Abstract	i
Kurzfassung	iii
Contents	iv
List of Figures	vi
Glossary	ix
1 Introduction	1
1.1 Laser interferometric gravitational wave detection	2
1.2 Dominant noise sources in interferometers	3
1.2.1 Seismic noise	3
1.2.2 Thermal noise	3
1.2.3 Quantum noise	5
1.3 Thermal effects	6
1.4 All-reflective interferometry	6
1.5 Structure of the thesis	10
2 Phase relations of 3-port-grating cavities	11
2.1 Scattering matrix formalism	11
2.1.1 2-port scattering matrix	12
2.2 3-port scattering matrix	13
2.2.1 General representation of a 3-port scattering matrix	13
2.2.2 Symmetric binary gratings	16
2.3 Light fields at 3-port-grating cavities	19
2.3.1 Linear two mirror cavity	19
2.3.2 Linear cavity with a binary 3-port diffraction grating	21
2.4 Experimental verification of phase relations	26
3 Control of 3-port-grating cavities	29
3.1 Phase modulation and Pound-Drever-Hall technique	29
3.2 Generation of error signals	30
3.2.1 Error signal of a two mirror cavity	32

3.2.2	Error signal of a 3-port-grating coupled cavity	33
3.3	Experimental verification of error signal	42
3.3.1	Error signal with strong asymmetry	42
3.3.2	Error signal with small asymmetry	44
4	Side-motion induced phase noise	47
4.1	Side-motion induced phase shift	47
4.2	Frequency-domain simulation	49
4.3	Time-domain simulation	53
4.3.1	Generation of linear spectra	55
4.4	Experimental verification of side motion phase noise	57
5	Power recycling	63
5.1	Two cavities coupled by a conventional mirror	63
5.2	Two cavities coupled by a 3-port-grating	66
5.3	Experimental realization of a power recycled 3-port-grating coupled cavity	74
5.3.1	Geometrical considerations	74
5.3.2	Experimental set-up	75
5.3.3	Comparison with simulations	77
5.3.4	Control of Power-Recycled 3-port Cavities	84
6	Resonant sideband extraction	87
6.1	Introduction	87
6.2	Conventional mirror settings	89
6.2.1	Signal transfer of a two mirror cavity	89
6.2.2	Signal transfer of a two resonators coupled by a conventional mirror	89
6.3	3-port-grating settings	92
6.3.1	Signal transfer of a 3-port-grating cavity	92
6.3.2	Signal transfer of two cavities coupled by a 3-port-grating	93
6.4	Resonant sideband extraction for 3-port-grating cavities	97
7	Summary and Outlook	101
A	Time-domain Simulation	103
	Bibliography	125
	Acknowledgements	133
	Curriculum vitae	135
	Publications	137

List of Figures

1.1	Topologies of laser interferometric gravitational wave detectors	2
1.2	All-reflective Michelson interferometer	7
1.3	All-reflective cavity topologies	8
2.1	Labeling of 2-port component	12
2.2	Labeling of the ports of a 3-port diffraction grating.	14
2.3	Labeling of amplitude diffraction efficiencies	14
2.4	Restrictions for diffraction efficiencies of generic 3-port-grating	16
2.5	Labeling of amplitude diffraction efficiencies of a binary 3-port-grating	17
2.6	Linear two mirror cavity	19
2.7	Light fields at a linear two mirror cavity	20
2.8	Light field coupling for linear two mirror cavity	21
2.9	Labeling of the fields of a 3-port-grating cavity.	22
2.10	Light power at a 3-port-grating cavity with $\eta_{2\min}$	23
2.11	Light power at a 3-port-grating cavity with $\eta_{2\max}$	24
2.12	Light power at a 3-port-grating cavity with $\eta_2^2 = 0.475$	24
2.13	Light power at 3-port-grating cavity for different input coupling	25
2.14	Experimental set-up to verify the phase-relations for binary 3-port-gratings	27
2.15	Normalized power at G1 3-port-grating cavity	27
2.16	Normalized power at G2 3-port-grating cavity	28
3.1	Error signal of a linear two mirror cavity	33
3.2	Error signal of a 3-port-grating cavity with $\eta_{2\min}$ for $\chi_{\text{dem}} = 0^\circ$	35
3.3	Error signal of a 3-port-grating cavity with $\eta_{2\min}$ for $\chi_{\text{dem}} = 90^\circ$	36
3.4	Error signal of a 3-port-grating cavity with $\eta_{2\max}$ for $\chi_{\text{dem}} = 0^\circ$	37
3.5	Error signal of a 3-port-grating cavity with $\eta_{2\max}$ for $\chi_{\text{dem}} = 90^\circ$	38
3.6	Error signal of a 3-port-grating cavity with $\eta_2 = \eta_0$ for $\chi_{\text{dem}} = 0^\circ$	40
3.7	Error signal of a 3-port-grating cavity with $\eta_2 = \eta_0$ for $\chi_{\text{dem}} = 90^\circ$	41
3.8	Sum of error signals at forward and back-reflected port	41
3.9	Experimental set-up to validate asymmetric error signals	43
3.10	Calculated error signal sum	43
3.11	Measured error signal sum	44
3.12	Schematic of the experimental set-up.	45
3.13	Comparison of modeled and measured error signals	46

4.1	Phase change at grating due to lateral displacement	48
4.2	Labeling of the ports of a 3-port-grating	49
4.3	Internal input ports of 3-port-grating cavity	50
4.4	Frequency domain simulation of lateral displacement noise coupling to length sensing signal	52
4.5	Labeling of ports for time domain simulation	54
4.6	Time domain transfer function of side motion noise	57
4.7	Schematic of the set-up at the Glasgow 10 m prototype	58
4.8	Grating mounted in suspended dummy mass	59
4.9	Magnet-coil actuator attached to the side of the test mass	59
4.10	Calibrated translational displacement measured with a laser-doppler vibrometer	60
4.11	Methods to generate lateral displacement	60
4.12	Measured and predicted responses at the forward-reflected port for translational motion of the grating	61
5.1	Labeling of the fields at a three mirror coupled cavity	64
5.2	Transmitted power at a linear three mirror cavity	66
5.3	Compound mirror reflectivities at linear three mirror cavity	67
5.4	Light-field amplitudes at a power recycled 3-port-grating cavity	67
5.5	Power transfer function at power recycled 3-port-grating cavity with $\eta_{2\min}$	69
5.6	Compound mirror reflectivities at power recycled 3-port-grating cavity with $\eta_{2\min}$	70
5.7	Power transfer function at power recycled 3-port-grating cavity with $\eta_{2\max}$	71
5.8	Power transfer function to forward and back reflected port of a power recycled 3-port cavity	72
5.9	Compound mirror reflectivities at power recycled 3-port-grating cavity with $\eta_{2\max}$	72
5.10	Power transfer function of power recycled 3-port-grating cavity with $\eta_2 = \eta_0$	73
5.11	Compound mirror reflectivities at power recycled 3-port-grating cavity with $\eta_2 = \eta_0$	73
5.12	Geometrical configuration of power recycled 3-port-grating cavity experiment	75
5.13	Experimental set-up of a 3-port-grating cavity with power recycling	76
5.14	Simulation of the power at the back reflected port	78
5.15	Measured power at the back-reflected port	79
5.16	Simulation of the power at the forward reflected port	80
5.17	Measured power at the forward-reflected port	81
5.18	Simulation of the internal power inside the arm cavity	82
5.19	Measured light power that is transmitted at the grating	83
6.1	Schematic of the Advanced LIGO topology	88
6.2	Interaction of gravitational wave with linear two mirror cavity	89
6.3	Signal transfer function of linear two mirror cavity	90
6.4	Schematic of of simplified RSE configuration with mirrors	90
6.5	Signal transfer function of linear three mirror cavity	91

viii List of Figures

6.6	Compound mirror reflectivity of RSE-configuration	92
6.7	Interaction of gravitational wave with a 3-port-grating cavity	93
6.8	Signal transfer function of 3-port-grating cavity	94
6.9	Signal input at two resonators coupled by a 3-port-grating	94
6.10	Signal transfer function to back-reflected port of 3-port-grating cavity with one extraction mirror	96
6.11	Signal transfer function to forward-reflected port of 3-port-grating cavity with one extraction mirror	96
6.12	3-port-grating cavity RSE-topology	97
6.13	Signal transfer function of 3-port-grating cavity RSE-configuration	99
6.14	Signal transfer function of 3-port-grating cavity RSE-configuration for different extraction mirror reflectivities	99
6.15	Schematic of resonant sideband extraction interferometer with 3-port-grating arm cavities	100

Glossary

Abbreviations

BS	Beam splitter
DC	Direct current
EOM	Electro optical modulator
FSR	Free spectral range
FWHM	Full width half maximum
PD	Photo detector
PR	Power recycling
PZT	Piezo electric transducer
RF	Radio frequency
RSE	Resonant sideband extraction

Symbols

c	Speed of light
λ	Laser wavelength
ρ	Amplitude reflectivity
τ	Amplitude transmissivity
η_0	0th order amplitude diffraction efficiency (2nd order Littrow)
η_1	1st order amplitude diffraction efficiency
η_2	2nd order amplitude diffraction efficiency
ρ_0	0th-order amplitude diffraction efficiency (normal incidence)
ϕ_1	Phase shift associated with 1st order diffraction
ϕ_2	Phase shift associated with 2nd order diffraction
p	Grating period
μ	diffraction order
L	Cavity length
Φ	Cavity detuning
ω_0	Angular carrier frequency
ω_m	Angular modulation frequency
G	Transfer function of cavity
H_0	DC component of demodulated Signal
H_{ω_m}	Error signal component of demodulated Signal
f_s	Sampling frequency
f_{res}	Resolution frequency

Introduction

One of the predictions that can be deduced from Albert Einstein's theory of General Relativity is the existence of gravitational waves [1]. These waves are ripples in space time, that are caused by accelerated massive objects and travel at the speed of light. Exemplary sources of gravitational waves are coalescing binary systems consisting of compact astrophysical objects like black holes or neutron stars, or cataclysmic events like supernovae core collapses. The first indirect experimental proof of the existence of such waves was done by Hulse and Taylor in 1974 [2] [3]. Their longtime study of the orbit period of the pulsar PSR 1913+16 around its companion star revealed, that the observed decay fits the predicted energy loss due to emission of gravitational waves as predicted by the theory of General Relativity. In 1993, the Nobel Prize was awarded to Hulse and Taylor for this discovery. Taking into account that present astrophysical observation are completely relying on the detection of electromagnetic radiation, the direct detection of gravitational waves would be the starting point of a new era of astronomy.

The expected gravitational wave amplitude or strain is defined as a relative length change according to [4]:

$$h = \frac{2\delta L}{L}. \quad (1.1)$$

The expected signal for a strong event is of the order $h = 10^{-21}$. Since the signal is extremely weak, the direct detection represents one of the biggest challenges in experimental physics. In the 1960's Joseph Weber's approach was to use large aluminum cylinders with high mechanical Q factors, called resonant bar detectors [5]. An incident gravitational wave should excite the mechanical eigenmode of the cylinder, which is then detected by a transducer that converts the vibration of the cylinder into an electrical signal. Although Weber's instrument was not sensitive enough for an actual detection, many groups all over the world started to develop and improve resonant bar detectors [6]. Similar to the electromagnetic emission of astrophysical objects, gravitational waves are also expected to span over a wide frequency range. Given that bar detectors are only sensitive around their narrowband mechanical resonance, they are not well suited to perform gravitational wave astronomy.

1.1 Laser interferometric gravitational wave detection

In comparison to the narrowband resonant bar detectors, laser interferometric gravitational wave detectors provide a relatively broad detection bandwidth. In order to cover the mHz region the space-borne laser interferometric gravitational wave detector LISA is currently under development [7]. This low frequency regime is inaccessible to ground-based detectors due to local gravitational noise arising from atmospheric effects and seismic activity. LISA will consist of three spacecrafts that act as an interferometer with an armlength of $5 \cdot 10^6$ km. Currently LISA is foreseen to launch in 2018.

For the frequency range between 10 Hz and a few kHz a large international network of ground-based laser interferometric gravitational wave detectors has been established. All these detectors are based on variations of Michelson interferometers (see Figure 1.1). An ideally polarized gravitational wave causes a differential arm-length change. When

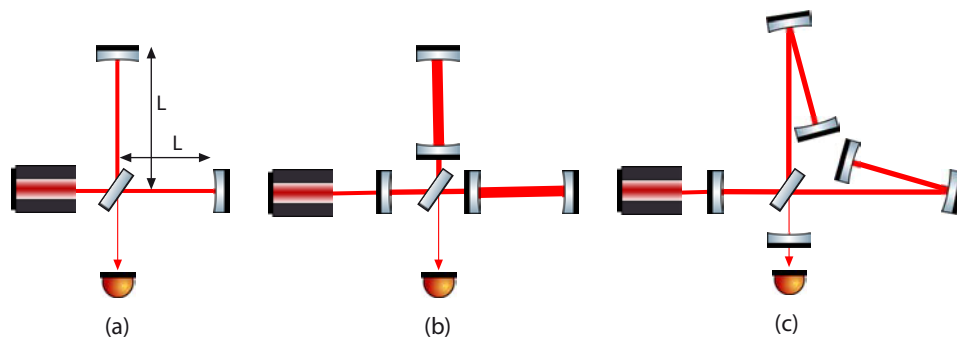


Figure 1.1 — (a) All current laser interferometric gravitational wave detectors are based on a Michelson interferometer. (b) The second configuration includes power-recycling and Fabry-Perot cavities in the arms. This layout is used by LIGO and Virgo. (c) In GEO600 the arms are folded once to double the effective arm length to 1200 m. Power-recycling and signal-recycling is used to enhance the sensitivity of the detector.

the Michelson interferometer is operated at the dark fringe, the differential modulation of the arm-length can be read out at the asymmetric port of the interferometer.

Currently gravitational wave detectors are operated at 5 different sites all over the world. The Laser Interferometer Gravitational wave Observatory (LIGO) involves two sites in the USA. In Livingston (Louisiana) and in Hanford (Washington) interferometers with an arm-length of 4 km have been built [8]. An additional 2 km instrument is sharing the same vacuum system at the Hanford site. A French-Italian cooperation enabled the installation of the 3 km instrument Virgo in Cascina, Italy [9]. GEO600 with an arm-length of 600 m was constructed by a German-British collaboration in Ruthe, Germany [10]. Another 300 m interferometer called TAMA300 is located in Tokyo, Japan [11]. Although there was no direct detection of gravitational waves as of yet, the first generation of ground-based detectors has produced scientifically relevant data [33]. A major upgrade of the US detector called Advanced LIGO will have an increased

sensitivity of a factor 10 [34]. Apart from upgrading the present infrastructure a design study for a European third generation detector is also underway [35].

1.2 Dominant noise sources in interferometers

The dominant noise sources that limit the sensitivity of laser interferometric gravitational wave detectors can be categorized in mainly three classes:

- Seismic noise
- Thermal noise
- Quantum noise

Seismic noise limits the sensitivity at the low frequency end of the detection window, typically below ≈ 40 Hz. Thermal noise limits the interferometric detectors in the mid-frequency range and the effect of photon shot noise typically dominates the noise budget above several hundred Hz.

1.2.1 Seismic noise

Interferometric gravitational wave detectors measure the relative distance between test masses. Any form of ground motion that shifts the center of mass or the surface of the test-mass cannot be distinguished from a signal caused by a gravitational-wave. The typical horizontal seismic noise spectrum above 3 Hz at the GEO600 site is roughly given by $(10^{-7}/f^2)\text{m}/\sqrt{\text{Hz}}$ [12]. In order to reach the required sensitivity of the detector the seismic noise must be decreased by more than ten orders of magnitude. The passive isolation is accomplished by suspending the test masses. Above the resonance frequency f_0 of a pendulum, the excitation due to an external force is reduced by $(f_0/f)^2$. By using n pendulum stages the total isolation amounts to $(f_0/f)^{2n}$ (assuming that all pendulums have the same resonance frequency). At frequencies below 1 Hz the dominant noise contribution is caused by gradients in the gravitational fields in the vicinity of the detector, which will always be present in ground based detectors [13].

1.2.2 Thermal noise

The fluctuation-dissipation theorem [14] indicates that a dissipation process is linked to thermal fluctuations. Basically, the thermal noise that affects gravitational wave detectors can be traced back to two different origins. The so-called suspension thermal noise originates from the dissipation in the wires or fibers used to suspend the test mass [12]. Mirror thermal noise can be traced back to dissipation processes in the test mass itself. The mirror thermal noise can be separated into three different kinds:

- Brownian thermal noise
- Thermo-refractive noise

- Thermo-elastic noise

It is important to note that these thermal noise effects arise from both the substrate material as well as from the dielectric multilayer coatings used to achieve a high optical reflectivity of the test mass.

The underlying dissipation process of Brownian thermal noise is the internal friction that affects the mechanical eigenmodes of the test mass. The mechanical eigenfrequencies of the test masses are typically well above the detection band for gravitational waves. However the off-resonant Brownian thermal noise contribution may limit the sensitivity in the most sensitive region of the detection band. In order to decrease the brownian thermal noise contribution, test masses with low internal friction and therefore low loss angle ϕ are used. For test masses with a small ϕ (high mechanical quality), the thermally driven motion is concentrated in a narrow frequency band around the mechanical eigenfrequencies of the test mass, leading to a smaller contribution below these frequencies.

Thermo-elastic damping is responsible for the thermoelastic contribution to the total thermal noise budget [23]. When a material is flexed, regions are compressed or expanded. In response, the material heats up or cools down, which creates a temperature gradient driving a heat flow. Some of the mechanical energy that was used to produce the flexing is dissipated. The converse also occurs in accordance with the fluctuation-dissipation theorem. The temperature of a macroscopic object like a test mass is an averaged quantity, and local fluctuations are always present, even when the object is in thermal equilibrium. These fluctuations drive mechanical noise in the material through thermal expansion. Therefore the leading parameter is the thermal expansion coefficient of the used material that generates fluctuations in the substrate [22] as well as in the coatings [15]. The dielectric coatings that are commonly used in today's detectors consist of alternating layers of Ta_2O_5 as a high refractive index material and SiO_2 as low index material. Recent studies found that the contribution of the coating is larger than from the bulk material, with the tantala layer providing the dominant contribution. The excess noise is associated with structural relaxations inside this material rather than on boundary effects on the interfaces between the coating layers. Doping the tantala with TiO_2 leads to a significant decrease of the coating thermal noise [17]. Apart from modifying the coating materials, several other techniques have been proposed to solve the coating thermal noise problem. By replacing the end mirror by a double mirror with a high effective reflectivity, the number of coating layers of the end mirror and thus the coating thermal noise can be reduced [18]. Another approach changes the mirror concept completely by using a resonant grating waveguide mirror, which provides a high reflectivity with only a single thin coating layer [19] or even without any additional coating [20].

Thermo-refractive noise originates from the temperature dependence of the index of refraction $\beta = dn/dT$, which is usually not zero. A temperature fluctuation will thus induce a variation of the optical path length [21]. Not only the substrate but also the coatings contribute to the thermo-refractive noise budget.

Thermo-refractive and thermo-elastic noise are often summed up under the term thermo-optic noise. A coherent treatment presented in [24] revealed that for coatings

thermo-elastic and thermo-refractive noise appear with a relative negative sign. Therefore the thermo-optic noise is significantly smaller than previously expected.

Since all these noise sources originate from stored thermal energy, cooling the test masses to cryogenic temperatures promises a significant decrease of the thermal noise budget. The Japanese project LCGT [25] is the first project that plans the deployment of cryogenic techniques.

Apart from decreasing the temperature also a careful choice of materials can be a promising path towards lowering the thermal noise budget. In interferometer topologies where optical components are used in transmission, only materials can be used that are highly transparent at the desired laser wavelength.

1.2.3 Quantum noise

Apart from the classical noise sources, photon quantum noise constitutes a fundamental limit for the sensitivity of the detector. Photon shot noise and radiation pressure noise are both noise sources that originate from vacuum noise impinging on the interferometer dark port. The noise contribution of the photon shot noise of a classical Michelson interferometer is given by [26]

$$h_{\text{shot}}(\Omega) = \frac{1}{2L} \sqrt{\frac{\hbar c \lambda}{\pi P}}, \quad (1.2)$$

where L is the detector arm length, λ the laser wavelength and P the total circulating power. From Equation (1.2) it can be deduced, that the sensitivity of a detector with a given length can be improved by increasing the circulating light power. Although the shot noise limited sensitivity improves for higher power, the radiation pressure noise, that originates from amplitude fluctuations, which gives rise to fluctuations in momentum of the test masses, is enhanced. The contribution of the radiation pressure noise to the linear spectral noise density of the gravitational wave strain amplitude for a simple Michelson interferometer is given by [27]:

$$h_{\text{rp}}(\Omega) = \frac{1}{2m\Omega^2 L} \sqrt{\frac{8\pi\hbar P}{c\lambda}}, \quad (1.3)$$

where m depicts the mass of one test mass. Instead of being frequency independent like the shot noise contribution, radiation pressure noise falls off with a $1/\Omega^2$ slope and is thus only significant at low frequencies. In the first generation of gravitational wave detectors, the radiation pressure noise contribution is below the seismic noise floor. For future generations of detectors however, radiation pressure noise is expected to limit the sensitivity at low frequencies, although heavier test masses are considered.

1.3 Thermal effects

Although the optical quality of substrate materials can be pushed into regions where the residual absorption is less than 1 ppm/cm [28], absorption based thermal effects can limit the storable power inside the interferometer and thus the sensitivity of the detector in the shot noise limited region. The influence of photo-thermal effects on the maximum storable power depends not only on the absorption of the used material, but also on its thermal properties. Almost all materials have an index of refraction that depends on the temperature. When light passes through such substrates in the presence of a temperature gradient, the material will act like a lens. The optical path length will be changed according to the gradient of the index of refraction. This effect is called thermal lensing [29]. The optical path length change δs due to this effect shows the proportionalities:

$$\delta s \propto \frac{\beta}{\kappa} P_A, \quad (1.4)$$

where κ and P_A depicts the thermal conductivity and the total absorbed power, respectively, and $\beta = dn/dT$ describes the temperature dependence of the index of refraction. Another photo-thermal effect originates from the thermal expansion α of the used materials. The optical components are locally heated by the absorbed light power, and consequently deformed which causes a wavefront distortion of the reflected or the transmitted beam. A comprehensive description of the photo-thermal effects and their implications for gravitational wave detectors is given in [30].

1.4 All-reflective interferometry

All-reflective interferometry with diffraction gratings for gravitational wave detectors was first proposed by Drever in 1995 [31]. The basic idea of all-reflective interferometry is to replace all optical components that are used in transmission by an all-reflective devices to avoid absorption based problems that occur when high laser power is transmitted through the bulk material. On the other hand, not being restricted to highly transparent substrate materials, widens the choice of possible candidates for substrate materials in future detectors. As shown in the previous section, material properties such as mechanical Q-factor, thermal expansion and thermal conductivity significantly influence the noise floor of a detector. Silicon for example is a potential candidate that offers excellent mechanical and thermal properties, but because of the high absorption at the currently used laser wavelength of 1064 nm, optics based on silicon substrates can only be used in all-reflective topologies. Given that the dominant contribution to the thermal noise budget originates from the dielectric multilayer coatings, this noise source is even more problematic. In contrast to partly transmissive optics, where some components only need to have a moderate reflectivity, which leads to a reduced number of coating layers, every all-reflective component has to be ultra-high reflective. In order to benefit from the advantages of all-reflective interferometry, it is essential that either the coating

materials are considerably improved in terms of their thermal noise performance, or the new developed techniques of grating waveguide mirrors as described in [19] and [20] are successfully united with the all-reflective schemes that are discussed in the following. In addition to the motivation for all-reflective interferometry given here, a comprehensive discussion can be found in [36].

Dielectric reflection gratings offer various possibilities to implement all-reflective interferometry, because they comprise a high reflectivity with the ability to split an incoming beam into a predefined number of partial beams. For a light field of wavelength λ incident onto a grating with a period p at an angle of incidence θ_{in} measured from the grating normal, the diffraction angle of the m -th order θ_m is given by the well known grating equation [32]:

$$\sin \theta_{\text{in}} + \sin \theta_m = \frac{m\lambda}{p}. \quad (1.5)$$

Note that Equation 1.5 only predefines the number and angles of the diffraction orders, but not the power distribution between them. The actual diffraction efficiency of each order depends not only on the grating period but also on the geometry of the periodic structure and the index of refraction of the used materials. An example for the complex task of grating design can be found in [37]. First experiments on all-reflective interferometry have been done at Stanford University in 1998 [38]. For these experiments, commercially available metal gratings were used. It was shown that a grating can be used as a 50/50 beam splitter in a Michelson or Sagnac Interferometer. (see Figure 1.2).

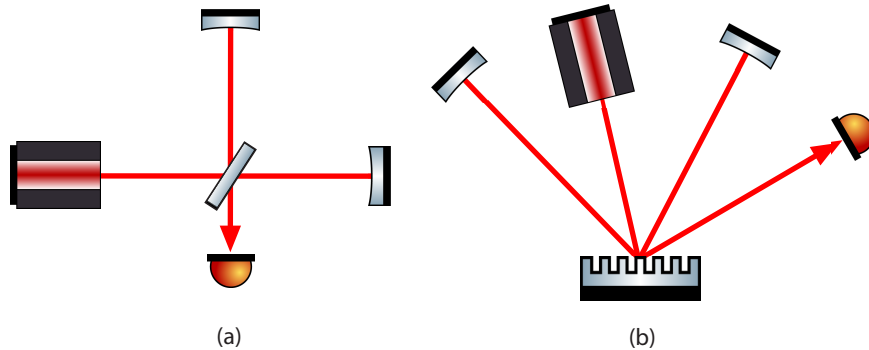


Figure 1.2 — (a) The key component of a Michelson interferometer is the 50/50 beam-splitter. While half of the incoming light field is reflected at the beam splitter, the other half is transmitted. (b) A properly designed reflection grating can split an incoming beam into two partial beams of equal power without relying on transmission. An all-reflective Michelson interferometer can be realized with such gratings.

Furthermore they presented the first experimental implementation of a Fabry-Perot cavity with a high efficiency diffractive coupler (see Figure 1.3 (b)). The metal gratings used by Sun were far away from meeting the strict requirements on optical quality that are valid for the use in gravitational wave detectors. In 2003 a joint project between

the Universities of Hannover and Jena was started to investigate grating based interferometry. Within this project dielectric reflection gratings were especially designed and manufactured by the Institute of Applied Physics in Jena based on the requirements for a possible application in gravitational wave detectors. Within this cooperation a power recycled Michelson interferometer with an all-reflective 50/50 beam splitter based on a dielectric diffraction grating has been set-up [39]. In order to replace a 50/50 beam splitter by a reflection grating, a grating is needed that splits an incoming beam into two partial beams, each of them containing half of the incident light power [40] as illustrated in Figure 1.2. By measuring the finesse of the power-recycling cavity the total optical

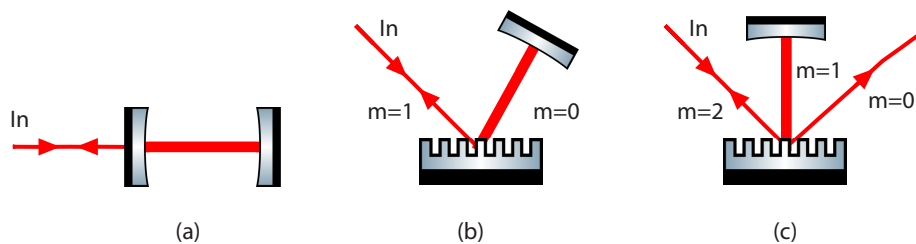


Figure 1.3 — (a) The coupling mirror of a Fabry-Perot cavity splits an incoming beam into two partial beams. While almost all the incoming light power is reflected, a small part is transmitted. (b) A properly designed reflection grating in 1st order Littrow configuration, also splits an incoming light field into two partial beams. While most of the incident light power, is diffracted backwards into the 1st diffraction order, a small amount of light is reflected into the 0th diffraction order. A high efficient grating can be used as an all-reflective cavity coupler. (c) In 2nd order Littrow configuration a low efficiency grating can be used as an all-reflective coupler. Most of the incoming light power is reflected in the 0th order diffraction.

loss of the grating beam splitter could be determined to a very high precision.

In another experiment the coupling mirror of a Fabry-Perot cavity was replaced by a high efficient reflection grating [41]. Therefore the grating was mounted in 1st order Littrow configuration as depicted in Figure 1.3 (b). Measurement of the cavity finesse provided precise information about the grating's diffraction efficiency and its optical loss. This method constitutes a novel method for high precision characterization of diffraction gratings. Recently this method could be improved by minimizing one of the largest measurement uncertainties [42]. In contrast to the previously demonstrated realization by Sun [38], the 1st order diffraction efficiency of $(99.635 \pm 0.016) \%$ was the highest value reported so far, and the total optical loss of the grating could be specified to only 0.185%. Furthermore another topology proposed by Drever in [31] was demonstrated for the first time.

The coupling mirror can also be replaced by a low efficient grating in 2nd order Littrow configuration as depicted in Figure 1.3 (c). In this configuration the finesse of the cavity is limited by the specular reflection under normal incidence, thus only a low diffraction efficiency in 1st and 2nd diffraction order is needed. Drever proposed this

scheme because he thought that low efficiency gratings could be manufactured with a lower optical loss than its high efficiency counterpart. In contrast to a conventional coupling mirror or a grating coupler in 1st order Littrow, this new device couples an incoming beam into three output ports. Therefore this device can be characterized as 3-port device. The first experimental demonstration of a 3-port-grating cavity [43] revealed, that due to the additional port of the coupler, different phase relations between the fields diffracted in each of the ports are valid [44].

1.5 Structure of the thesis

In this work the properties of 3-port-grating cavities are investigated with emphasis on a potential application in future gravitational wave detectors. Chapter 2 provides a theoretical description of a generic 3-port device using the scattering matrix formalism. From this general approach a description for the special case of binary 3-port-gratings is derived. If a binary 3-port-grating is used as a coupling component to a Fabry-Perot cavity, the derived phase relations between input and output ports of the device lead to a different cavity properties. This behavior is investigated theoretically as well as experimentally. In Chapter 3 the influence of the phase relation on length sensing and control of 3-port-grating coupled cavities is analyzed. In contrast to a conventional mirror, a translational displacement of a grating parallel to its surface in direction perpendicular to the grating grooves will induce a phase shift proportional to the diffraction order. The coupling of this additional noise source is investigated theoretically in frequency domain as well as in a time domain representation in Chapter 4. At a fully suspended 3-port-grating cavity the noise coupling to the length sensing signal of the cavity is verified.

The found phase relations between the input and output ports of a binary 3-port-grating also influences the properties of coupled resonator configuration as they are widely used in power-recycling and resonant-sideband extraction topologies. In Chapter 5 the implications on a 3-port-grating cavity with power-recycling are investigated. Furthermore a power-recycled 3-port-grating cavity is demonstrated experimentally. In Chapter 6 a configuration is proposed, that allows the combination of 3-port-grating cavities with the technique of resonant-sideband extraction. Chapter 7 provides some concluding remarks and an outlook. In the appendix additional information regarding simulation computer code can be found.

Phase relations of 3-port-grating cavities

In this chapter the theoretical description of 3-port diffraction gratings is reconsidered by using the scattering-matrix formalism. Initially this formalism will be introduced by deriving the input-output relations of a conventional mirror. Accordingly, the theoretical description of a general non-symmetric 3-port device is presented, using a parameterization of a 3×3 matrix. Moreover the scattering matrix for a binary and thereby symmetric 3-port-grating will be derived following from the general description. This description offers an alternative representation to the one developed in [44]. The scattering matrix is then used to determine the light power distribution of 3-port-grating cavities. Finally the theoretical description for the 3-port-grating cavity light field distribution is validated by an experiment.

2.1 Scattering matrix formalism

Amplitude and phase relations of optical components like mirrors, gratings and beam splitters can be derived by using the scattering matrix formalism [45]. The scattering matrix \mathbf{S} links the complex field amplitudes at the input ports represented by a vector \mathbf{v}_{in} with the complex field amplitudes at the output ports of the components given by the vector \mathbf{v}_{out} . With the help of this formalism the coupling between incident and emerging field at the component is given by:

$$\mathbf{v}_{\text{out}} = \mathbf{S} \times \mathbf{v}_{\text{in}}. \quad (2.1)$$

For loss-less components conservation of energy claims implies:

$$P_{\text{out}} = \mathbf{v}_{\text{out}}^\dagger \mathbf{v}_{\text{out}} = (\mathbf{S} \mathbf{v}_{\text{in}})^\dagger (\mathbf{S} \mathbf{v}_{\text{in}}) = (\mathbf{v}_{\text{in}}^\dagger \mathbf{S}^\dagger) (\mathbf{S} \mathbf{v}_{\text{in}}) = \mathbf{v}_{\text{in}}^\dagger (\mathbf{S}^\dagger \mathbf{S}) \mathbf{v}_{\text{in}} = P_{\text{in}}, \quad (2.2)$$

for input and output Power P_{in} and P_{out} , respectively. Therefore the scattering matrix of a loss-less component needs to be unitary:

$$\mathbf{S}^\dagger \mathbf{S} = \mathbf{1}. \quad (2.3)$$

Most optical components are reciprocal, which means that light paths are reversible. The components of the scattering matrix of a reciprocal component fulfill the relation:

$$S_{ij} = S_{ji}. \quad (2.4)$$

2.1.1 2-port scattering matrix

A conventional loss-less mirror that is illuminated from an angle of incidence of 0° splits an incoming light field into two partial beams, namely a reflected and a transmitted beam (see Figure 2.1). Such a mirror can therefore be considered as a 2-port component,

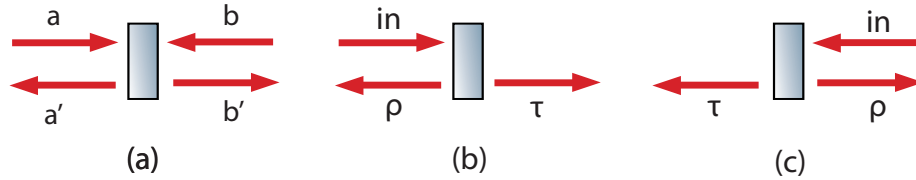


Figure 2.1 — Conventional mirror as a 2-port component: (a) labeling of the ports. Amplitude reflection and transmission coefficients for input from left hand side (b) and from right hand side (c). Reciprocity leads to equal coefficients for both inputs.

and in the most general form equation (2.1) can be written as:

$$\begin{pmatrix} a' \\ b' \end{pmatrix} = \underbrace{\begin{pmatrix} \rho_{11} \exp(i\phi_{11}) & \tau_{12} \exp(i\phi_{12}) \\ \tau_{12} \exp(i\phi_{12}) & \rho_{22} \exp(i\phi_{22}) \end{pmatrix}}_{\mathbf{S}_{2p}} \begin{pmatrix} a \\ b \end{pmatrix} \quad (2.5)$$

Every component of the scattering matrix is given by the amplitude reflection or transmission coefficient ρ or τ of the particular transition between the ports, and a phase ϕ . Since a mirror is reciprocal, $\tau_{12} = \tau_{21} = \tau$ is valid. With this symmetry consideration equation (2.3) leads to:

$$\mathbf{S}_{2p} \mathbf{S}_{2p}^\dagger = \begin{pmatrix} \rho_{11}^2 + \tau^2 & \tau (\rho_{11} e^{i(\phi_{11}-\phi_{12})} + \rho_{22} e^{i(\phi_{12}-\phi_{22})}) \\ \tau (\rho_{11} e^{i(\phi_{12}-\phi_{11})} + \rho_{22} e^{i(\phi_{22}-\phi_{12})}) & \rho_{22}^2 + \tau^2 \end{pmatrix} = \mathbf{1}. \quad (2.6)$$

As a consequence the following equations need to be solved in order to derive the phase relations providing a valid 2-port scattering matrix:

$$\rho_{11}^2 + \tau^2 = \rho_{22}^2 + \tau^2 = 1, \quad (2.7)$$

$$\tau (\rho_{11} e^{i(\phi_{11}-\phi_{12})} + \rho_{22} e^{i(\phi_{12}-\phi_{22})}) = 0. \quad (2.8)$$

From Equation (2.7) directly follows $\rho_{11} = \rho_{22}$, and from Equation (2.8) it can be deduced that $\phi_{11} - \phi_{12} = \phi_{12} - \phi_{22} + \pi$. One possible solution of Equation (2.8) is provided by the choice $\phi_{11} = \phi_{22} = 0$ and $\phi_{12} = \pi/2$. The resulting scattering matrix is given by:

$$S_{2p} = \begin{pmatrix} \rho & i\tau \\ i\tau & \rho \end{pmatrix}. \quad (2.9)$$

Besides another possible set of phases that solves equation (2.8) is the combination $\phi_{11} = \phi_{12} = 0$ and $\phi_{22} = \pi$ leading to the scattering matrix:

$$S_{2p} = \begin{pmatrix} \rho & \tau \\ \tau & -\rho \end{pmatrix}. \quad (2.10)$$

Both scattering matrices are physically equivalent and are both widely used in the literature. Of course these are not the only solutions that are conceivable, but probably the most convenient ones. Note that the phases in a 2-port scattering matrix are independent of the reflection and transmission coefficients.

2.2 3-port scattering matrix

Another device that splits an incoming light field into partial beams is a diffraction grating. Depending on the chosen combination of light wavelength λ , grating period p and angle of incidence θ_{in} (according to the grating equation (1.5)), many different multi-port devices are feasible. A grating with $\lambda < p < 2\lambda$ in 2nd order Littrow configuration is a 3-port device and can therefore be described by a 3×3 scattering matrix. As we will see in the following section, this will lead to phase relations between the ports that are not independent of the scattering coefficients (amplitude diffraction efficiencies), which is in contrast to the 2-port scattering matrix.

All the experiments presented in this thesis are based on binary 3-port diffraction gratings, that are symmetric with respect to the grating normal. Apart from the theoretical description of a symmetric grating, also the scattering matrix for a generic 3-port device without any assumed symmetries will be derived in the following. In [47] there is a generic description given, but further investigations proofed, that the conditions given there are not sufficient to generate a valid scattering matrix for an arbitrary choice of grating parameters.

2.2.1 General representation of a 3-port scattering matrix

First of all the most general form of a 3-port scattering matrix is derived. Again the scattering matrix links the complex amplitude at the inputs with those at the outputs. In analogy to equation (2.1) the input-output relation can be written as:

$$\begin{pmatrix} a' \\ b' \\ c' \end{pmatrix} = \underbrace{\begin{pmatrix} S_{11} & S_{12} & S_{13} \\ S_{12} & S_{22} & S_{23} \\ S_{13} & S_{23} & S_{33} \end{pmatrix}}_{S_{3p}} \begin{pmatrix} a \\ b \\ c \end{pmatrix} \quad (2.11)$$

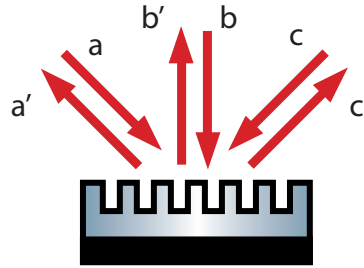


Figure 2.2 — Labeling of the ports of a 3-port diffraction grating.

Note that reciprocity of the device is ensured by choosing $S_{12} = S_{21}$, $S_{13} = S_{31}$ and $S_{23} = S_{32}$. Figure 2.2 shows how the ports are labeled. The magnitude of the scattering coefficients $|S_{ij}|$ or amplitude diffraction efficiencies for every transition are labeled as shown in Figure 2.3. Conservation of energy ensures that the phase independent diagonal elements of $\mathbf{S}^\dagger \mathbf{S}$ fulfill the following equations:

$$1 = \eta_{-1}^2 + \eta_1^2 + \rho_0^2, \quad (2.12)$$

$$1 = \eta_0^2 + \eta_1^2 + \eta_2^2, \quad (2.13)$$

$$1 = \eta_0^2 + \eta_{-1}^2 + \eta_{-2}^2. \quad (2.14)$$

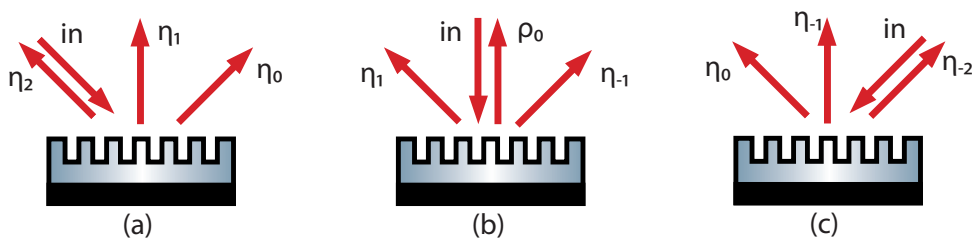


Figure 2.3 — Labeling of amplitude diffraction efficiencies of a non-symmetric 3-port-grating: (a) 2nd order Littrow configuration (b) normal incidence (c) -2nd order Littrow configuration.

According to [46] the 3-port scattering matrix can be parameterized by 6 parameters

$\alpha, \beta, \phi_{11}, \phi_{12}, \phi_{13}, \phi_{22}$ in the following way:

$$S_{11} = \alpha \cdot e^{i\phi_{11}} \quad (2.15)$$

$$S_{12} = \beta \sqrt{1 - \alpha^2} \cdot e^{i\phi_{12}} \quad (2.16)$$

$$S_{13} = \sqrt{(1 - \alpha^2)(1 - \beta^2)} \cdot e^{i\phi_{13}} \quad (2.17)$$

$$S_{22} = (1 - \beta^2) \cdot e^{i\phi_{22}} - \alpha\beta^2 \cdot e^{i(2\phi_{12} - \phi_{11})} \quad (2.18)$$

$$S_{23} = -\beta \sqrt{1 - \beta^2} \cdot (e^{i(\phi_{13} - \phi_{12} + \phi_{22})} + \alpha \cdot e^{i(\phi_{12} + \phi_{13} - \phi_{11})}) \quad (2.19)$$

$$S_{33} = \beta^2 \cdot e^{i(2(\phi_{13} - \phi_{12}) + \phi_{22})} - \alpha(1 - \beta^2) \cdot e^{i(2\phi_{13} - \phi_{11})} \quad (2.20)$$

If we now demand without loss of generality that:

$$\arg(S_{12}) = -\arg(S_{23}), \quad (2.21)$$

$$\arg(S_{11}) = -\arg(S_{33}), \quad (2.22)$$

then there are still four parameters left that still have to be predefined in order to obtain a scattering matrix representation of a specific grating. It is convenient to specify the diffraction efficiencies of 1st, 2nd and -1st order,

$$\eta_1 = |S_{12}| = \beta \sqrt{1 - \alpha^2}, \quad (2.23)$$

$$\eta_2 = |S_{11}| = \alpha, \quad (2.24)$$

$$\eta_{-1} = |S_{23}| = \beta \sqrt{1 - \beta^2} \sqrt{1 + \alpha^2 + 2\alpha \cos(\phi_{11} + \phi_{22} - 2\phi_{12})}. \quad (2.25)$$

With the choice of these parameters, all remaining diffraction efficiencies are fixed due to the conservation of energy (see Equations (2.12)-(2.14)). If we now choose one of the phases - for example ϕ_{12} - than all components of the scattering matrix can be calculated. Solving Equation (2.25) for ϕ_{11} yields:

$$\phi_{11} = 2\phi_{12} - \phi_{22} + \psi \quad (2.26)$$

$$\text{with } \psi := \arccos \left(\frac{1}{2\alpha} \left[\frac{\eta_{-1}^2}{\beta^2(1 - \beta^2)} - (1 + \alpha^2) \right] \right) = \arccos(\zeta) \quad (2.27)$$

From equation (2.21) and (2.22) we can deduce an expression for ϕ_{22} and ϕ_{13} , respectively:

$$\phi_{22} = \pi - [\phi_{13} + \arg(1 + \alpha \cdot e^{-i\psi})], \quad (2.28)$$

$$\phi_{13} = -\frac{1}{2} \arg(\beta^2 \cdot e^{i\psi} - \alpha(1 - \beta^2)). \quad (2.29)$$

Since the phases ϕ_{22}, ϕ_{13} and ϕ_{11} are all real numbers the absolute value of the argument of the arccos-function in equation (2.27) ζ has to be smaller or equal to 1. With equations (2.23) and (2.24) ζ can be written as:

$$\zeta = \frac{1}{2\eta_2} \left[\frac{(1 - \rho_0^2 - \eta_1^2)(1 - \eta_2^2)}{\eta_1^2(1 - \frac{\eta_1^2}{1 - \eta_2^2})} - (1 + \eta_2^2) \right]. \quad (2.30)$$

Due to the restriction of the value of ζ there are constrictions on the combination of diffraction efficiencies which are physically allowed. The colored area in Figure 2.4 marks the allowed combinations of η_1^2 and η_2^2 for gratings with $\rho_0^2 = 0.9$. Note that by fixing this three diffraction efficiencies, the remaining η_{-1}^2 and η_0^2 are given by energy conservation. Gratings can only be designed and manufactured with diffraction efficiencies specified by the colored area in the graph. It can be seen for a symmetric grating, where the

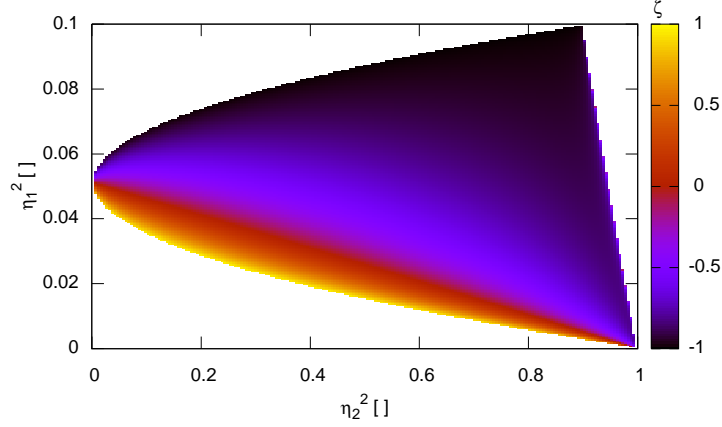


Figure 2.4 — Parameter ζ for $\rho_0^2 = 0.9$ as a function of η_1^2 and η_2^2 . The colored area shows the allowed combinations of η_1^2 and η_2^2 .

diffraction efficiencies of ± 1 st order are identical, that the value of the 2nd order diffraction efficiency η_2 can be very small. If for example the diffraction efficiency of ± 1 st order differ drastically, the 2nd order diffraction efficiency must be very high. As a consequence a strongly asymmetric 3-port-grating needs to be a high efficient grating in the 2nd diffraction order, while the ± 1 st order diffraction efficiency is relatively low. One has to emphasize that the phases are functions of the diffraction efficiencies. Therefore the phase relations vary depending on the properties of the grating. This contrasts with the properties of a 2-port device like the mirror discussed above, where the phases are independent of the transmission and reflection coefficients.

2.2.2 Symmetric binary gratings

If the grating profile is binary the grating is symmetric with respect to its normal. Therefore the diffraction efficiencies of negative and positive diffraction orders are identical ($\eta_2 = \eta_{-2} = \alpha$ and $\eta_1 = \eta_{-1} = \beta\sqrt{1 - \alpha^2}$) and can be labeled as seen in figure 2.5. Energy conservation yields the following equations:

$$1 = \eta_0^2 + \eta_1^2 + \eta_2^2, \quad (2.31)$$

$$1 = \rho_0^2 + 2\eta_1^2. \quad (2.32)$$

If again the parameters α , β and ϕ_{12} are set, then the remaining phases giving the full

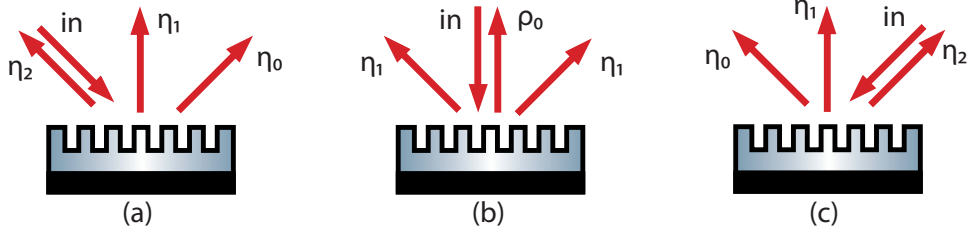


Figure 2.5 — Labeling of amplitude diffraction efficiencies of a binary 3-port-grating: (a) 2nd order Littrow configuration (b) normal incidence (c) -2nd order Littrow configuration.

scattering matrix can be written as:

$$\phi_{11} = 2\phi_{12}, \quad (2.33)$$

$$\phi_{22} = \arccos \left(\frac{1}{2\alpha} \left(\frac{1 - \alpha^2}{1 - \beta^2} - (1 - \alpha^2) \right) \right) = \arccos(z), \quad (2.34)$$

$$\phi_{13} = \arccos \left(-\frac{\beta^2}{2\alpha} \sqrt{\frac{(1 - \alpha^2)}{(1 - \beta^2)}} \right). \quad (2.35)$$

Since the phases are real numbers the absolute value of the argument z must be smaller or equal to 1. Therefore there is an upper and lower limit for η_0 and η_2 which is given by:

$$\eta_{0\min} = \eta_{2\min} = (1 \pm \rho_0)/2. \quad (2.36)$$

As a consequence the symmetric 3-port diffraction grating can only be designed and manufactured with diffraction efficiencies within these boundaries. Due to the symmetry of the system the scattering matrix can be simplified to:

$$\mathbf{S}_{3p} = \begin{pmatrix} \eta_2 \exp(i\phi_{11}) & \eta_1 \exp(i\phi_{12}) & \eta_0 \exp(i\phi_{13}) \\ \eta_1 \exp(i\phi_{12}) & -\alpha\beta^2 + (1 - \beta^2) \cdot \exp(i\phi_{22}) & \eta_1 \exp(-i\phi_{12}) \\ \eta_0 \exp(i\phi_{13}) & \eta_1 \exp(-i\phi_{12}) & \eta_2 \exp(-i\phi_{11}) \end{pmatrix}. \quad (2.37)$$

Of course, this 3-port scattering matrix is not the only valid representation. Analogue to the well known 2-port case there are alternative solutions available. Another option for the symmetric 3-port scattering matrix is presented in [44]. Here the scattering matrix is written as:

$$\mathbf{S}_{3p} = \begin{pmatrix} \eta_2 \exp(i\phi_2) & \eta_1 \exp(i\phi_1) & \eta_0 \exp(i\phi_0) \\ \eta_1 \exp(i\phi_1) & \rho_0 \exp(i\phi_0) & \eta_1 \exp(i\phi_1) \\ \eta_0 \exp(i\phi_0) & \eta_1 \exp(i\phi_1) & \eta_2 \exp(i\phi_2) \end{pmatrix}, \quad (2.38)$$

where the phase shifts associated with 0th, 1st and 2nd order diffraction are denoted ϕ_0 , ϕ_1 and ϕ_2 . respectively. From the requirement that \mathbf{S} needs to be unitary, the phases

can be calculated, yielding the following set of phases:

$$\phi_0 = 0, \quad (2.39)$$

$$\phi_1 = -(1/2) \arccos[(\eta_1^2 - 2\eta_0^2)/(2\rho_0\eta_0)], \quad (2.40)$$

$$\phi_2 = \arccos[-\eta_1^2/(2\eta_2\eta_0)]. \quad (2.41)$$

Since all physically valid scattering matrices are equivalent, this set of phases leads to the same restrictions for the diffraction efficiencies as equation (2.36).

2.3 Light fields at 3-port-grating cavities

The knowledge of the input-output relations of the isolated component permits the calculation of arbitrary interferometric topologies that are based on these components. A commonly used building block of modern interferometers is a linear Fabry-Perot resonator. In general a linear Fabry-Perot resonator, often called linear cavity, consists of two mirrors m_1 and m_2 that are spatially separated and oriented orthogonally to the light path (see Figure 2.6). The coupling mirror of such a cavity can be replaced by a 3-port diffraction grating in 2nd order Littrow configuration in order to construct an all-reflective cavity. In this section the expressions describing the resonance features of a

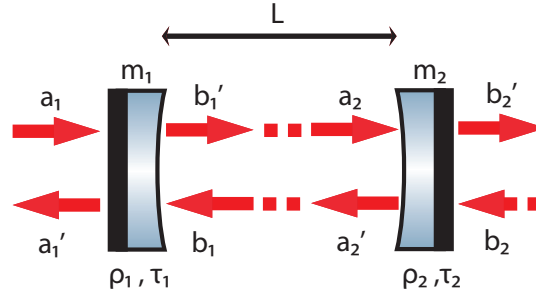


Figure 2.6 — Linear cavity of length L with two mirrors m_1 and m_2 with reflection and transmission coefficients ρ_i and τ_i . The light field couples into the system at port a_1 , while there is no input at port b_2 .

monochromatic light field of wavelength λ at both types of cavities will be discussed. In the following it is assumed that all optical components are loss-less.

2.3.1 Linear two mirror cavity

With the help of the scattering matrix of a mirror derived in 2.1.1 the fields at a linear cavity like the one shown in Figure 2.6 can be written as a function of the input field a_1 [48]:

$$b'_1 = \frac{i\tau_1}{1 - \rho_1\rho_2e^{2i\Phi}}a_1 = (i\tau_1d)a_1, \quad (2.42)$$

$$b'_2 = -\frac{\tau_1\tau_2e^{i\Phi}}{1 - \rho_1\rho_2e^{2i\Phi}}a_1 = (-\tau_1\tau_2e^{i\Phi}d)a_1, \quad (2.43)$$

$$a'_1 = \frac{\rho_1 - (\tau_1^2 + \rho_1^2)\rho_2e^{2i\Phi}}{1 - \rho_1\rho_2e^{2i\Phi}}a_1 = (\rho_1 - \rho_2e^{2i\Phi})d \cdot a_1, \quad (2.44)$$

with the resonance factor of the cavity $d = (1 - \rho_1\rho_2e^{2i\Phi})^{-1}$. Apart from the reflection and transmission coefficients of the mirrors, the internal field b'_1 , the field that is reflected

a'_1 and the transmitted field of the cavity b'_2 , also depend on the tuning parameter Φ . This parameter expresses the length of the cavity and is given by:

$$\Phi = \frac{\omega L}{c}, \quad (2.45)$$

where L depicts the length of the cavity, ω the angular frequency and c the speed of light. The cavity is on resonance for a tuning of $\Phi \bmod \pi = 0$ leading to a power build-up inside the cavity. The internal power $|b'_1|^2$ as well as the transmitted and reflected light power, $|b'_2|^2$ and $|a'_1|^2$, respectively, inside a two mirror cavity are shown in Figure 2.7 as a function of the cavity tuning Φ for exemplary values of the mirror reflectivities.

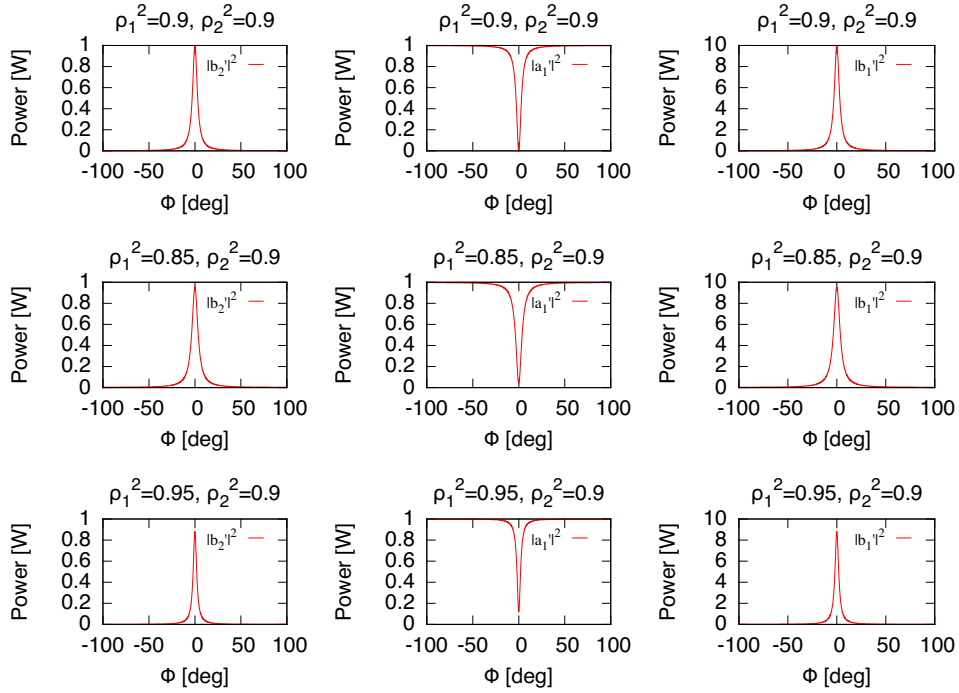


Figure 2.7 — Light fields at a two mirror cavity as a function of the tuning Φ for exemplary values of mirror reflectivities.

The field distribution strongly depends on the relation of coupling mirror and end mirror reflectivity as it is shown in Figure 2.8. Here the end mirror reflectivity is fixed with $\rho_2^2 = 0.9$ and the cavity is tuned to the resonance at $\Phi = 0^\circ$, while the reflectivity of the coupling mirror ρ_1^2 is varied. In the loss-less case a cavity is called impedance matched if $\rho_1^2 = \rho_2^2$ is fulfilled. In this setup, the internal power build-up is maximized. In this configuration the power reflected at the cavity is zero when the cavity is tuned to resonance ($\Phi \bmod \pi = 0$). Decreasing or increasing of ρ_1 will both lead to a power reflectivity of the cavity greater than zero and also a lower power build-up inside the cavity than in the impedance matched case. If $\tau_1 > \tau_2$ the configuration is called over-coupled and if $\tau_1 < \tau_2$ the cavity is under-coupled. For a detailed analysis of different cavity configurations that also consider lossy mirrors see [48].

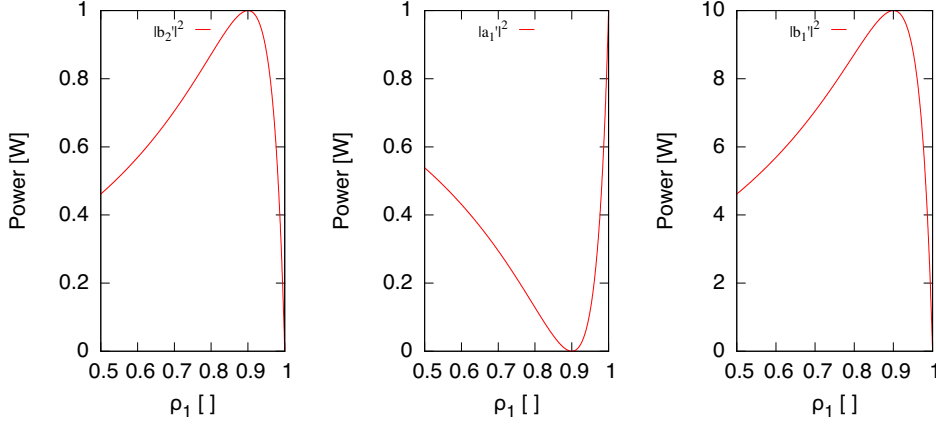


Figure 2.8 — Light field distribution for a loss-less cavity with $\rho_2^2 = 0.9$ as a function of coupling mirror reflectivity. For $\rho_1^2 = \rho_2^2$ the cavity is impedance matched, leading to the highest power build-up. In this configuration no light is reflected at the resonant cavity, hence the full light power is transmitted. Decreasing or increasing the coupling mirror reflectivity leads to a power reflectivity of the cavity greater than zero and a lower power build-up inside the resonator.

Two important parameters that are used to characterize cavities are the free spectral range FSR and the finesse \mathcal{F} . The spectral separation of two adjacent resonance peaks is called the free spectral range and is given by:

$$\text{FSR} = \frac{c}{2L}. \quad (2.46)$$

The finesse of a cavity is the ratio of the free spectral range and the full width at half maximum of the resonance FWHM. The finesse can also be approximated in terms of the reflectivities of the mirrors:

$$\mathcal{F} = \frac{\text{FSR}}{\text{FWHM}} \approx \frac{\pi\sqrt{\rho_1\rho_2}}{1 - \rho_1\rho_2} \quad (2.47)$$

If one mirror of the cavity is already thoroughly characterized measuring the finesse allows for a very accurate determination of the unknown reflectivity of the second mirror [41].

2.3.2 Linear cavity with a binary 3-port diffraction grating

If the coupling mirror m_1 is replaced by a 3-port-grating in 2nd order Littrow configuration as shown in Figure 2.9 an all-reflective cavity is realized. In contrast to the conventional mirror cavity, this cavity provides two ports in reflection denoted by a and c . The fields at such a 3-port-grating coupled cavity as a function of the input field a_1 can be written as:

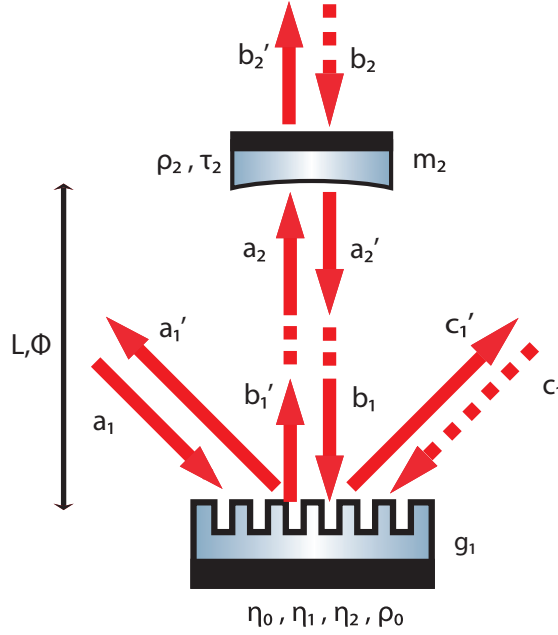


Figure 2.9 — Labeling of the fields of a 3-port-grating cavity.

$$a_1' = (\eta_2 e^{i\phi_2} + \eta_1^2 \rho_2 e^{2i(\phi_1 + \Phi)} d) \cdot a_1, \quad (2.48)$$

$$b_1' = \eta_1 e^{i\phi_1} d \cdot a_1, \quad (2.49)$$

$$c_1' = (\eta_0 + \eta_1^2 \rho_2 e^{2i(\phi_1 + \Phi)} d) \cdot a_1, \quad (2.50)$$

$$b_2' = i\tau_2 \eta_1 e^{i(\phi_1 + \Phi)} d \cdot a_1, \quad (2.51)$$

with $d = [1 - \rho_0 \rho_2 \exp(2i\Phi)]^{-1}$. The phase shift associated with diffraction at the grating depends on the diffraction efficiencies of the device, thereby also the cavity properties strongly depend on these parameters.

For the following discussion of the cavity properties the end mirror m_2 was chosen to be a perfect reflector with $\rho_2^2 = 1$. The 1st order diffraction efficiency was chosen to be $\eta_1^2 = 0.05$ which leads to a reflectance under normal incidence of $\rho_0^2 = 0.9$ (according to the energy conservation: $1 = \rho_0^2 - 2\eta_1^2$). For a given length of the cavity, this choice of grating parameters already determines the finesse and the internal build-up of the cavity. By specifying the balancing between η_0 and η_2 only the field distribution at the two reflection ports of the cavity are affected. As known from equation (2.36) not every combination of diffraction efficiencies is possible because η_0 and η_2 are only valid within the given boundaries. In the following this set-up will be investigated for different values of η_2 and unity input ($a_1^2 = 1$).

Light fields at a 3-port-grating cavity in $\eta_{2\min}$ -configuration

Let us first consider a grating with $\eta_2 = \eta_{2\min} = (1 - \rho_0)/2$. Since the transmission of the end mirror is zero, no light is transmitted through the cavity. Therefore the internal light power as well as the power at the two reflection ports of the cavity for unity input is shown in Figure 2.10 for a grating with $\eta_1^2 = 0.05$. On resonance ($\Phi = 0$) the power of the light field being reflected in forward direction is zero and all the light is back-reflected towards the input light source. Taking this into consideration, the configuration is similar to the impedance matched case of a two mirror cavity, where the back-reflected port of the grating cavity corresponds to the transmission port, and the forward-reflected port shows the same behavior as the reflection port of the conventional two mirror cavity. In contrast to the two mirror cavity case, this behavior is independent of the choice of ρ_0^2 . As long as the end mirror is a perfect reflector and the grating is in $\eta_{2\min}$ -configuration, this argumentation holds.

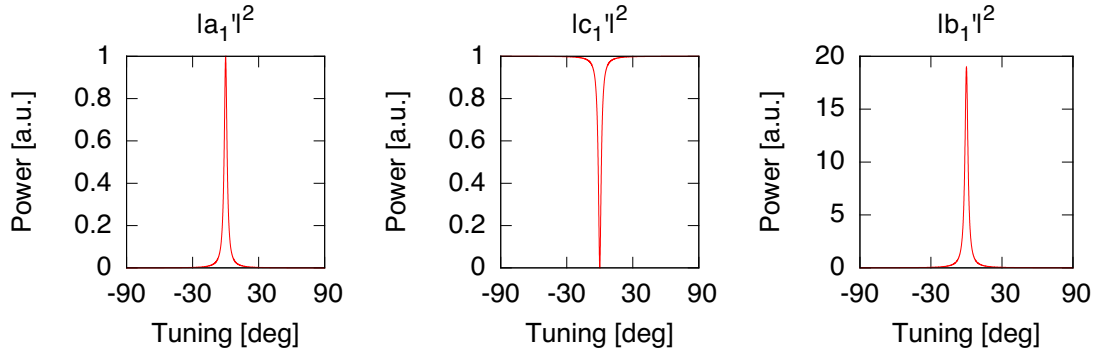


Figure 2.10 — Light power at a 3-port-grating coupled cavity, with $\rho_2^2 = 1$, $\eta_1^2 = 0.05$ and $\eta_2 = \eta_{2\min} = (1 - \rho_0)/2$.

Light fields at a 3-port-grating cavity in $\eta_{2\max}$ -configuration

In $\eta_{2\max}$ -configuration ($\eta_2 = (1 + \rho_0)/2$) the two reflection ports are inverted. The forward-reflected port is bright, while the back-reflected port is completely dark on resonance. However, the internal power remains unchanged, since only the balancing between η_0 and η_2 was altered. The parameters determining the internal field of the cavity are ρ_0 and η_1 , which remain unchanged compared to the previous example. The light power at the two ports of the cavity with a perfect reflecting end mirror as well as the internal power is shown in Figure 2.11.

Light field at a 3-port-grating with $\eta_2^2 = 0.475$

Let us now consider a grating with a 2nd order diffraction efficiency of $\eta_2^2 = 0.475$, which is far away from the two extreme values. Again only the balancing of η_0 and η_2 is altered and all other cavity parameters remain unchanged. In this configuration the

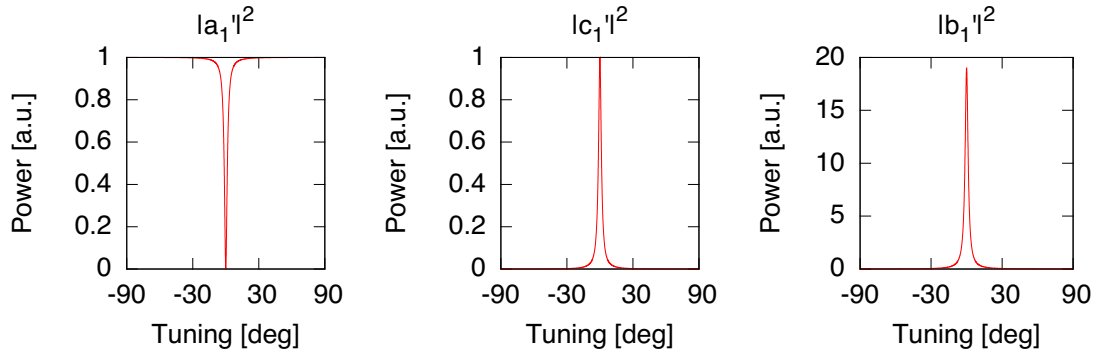


Figure 2.11 — Light power at a 3-port-grating coupled cavity, with $\rho_2^2 = 1$, $\eta_1^2 = 0.05$ and $\eta_2 = \eta_{2,\max} = (1 + \rho_0)/2$.

resonance peak at the two reflection ports is no longer symmetric with respect to the resonant tuning $\Phi = 0$ as can be seen in Figure 2.12.

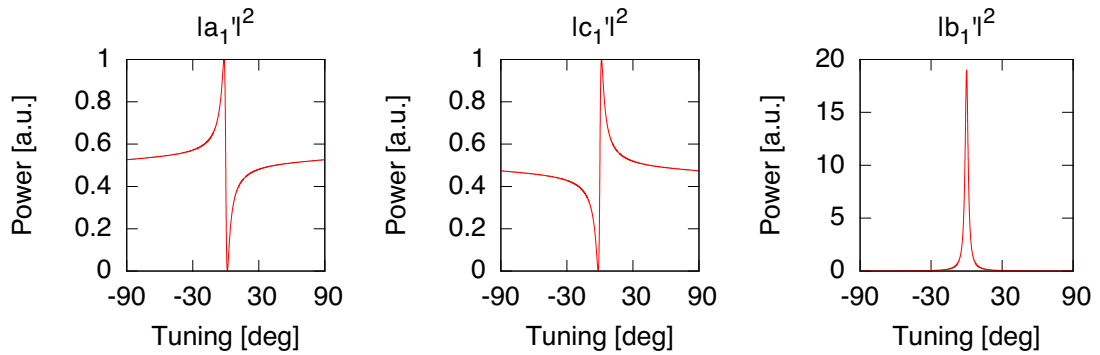


Figure 2.12 — Light power at a 3-port-grating coupled cavity, with $\rho_2^2 = 1$, $\eta_1^2 = 0.05$ and $\eta_2^2 = 0.475$.

Light field for different input coupling

The light field distribution at the output ports of a 3-port-grating cavity also depends on the relation between coupling reflectivity ρ_0 and end mirror reflectivity ρ_2 . Figure 2.13 shows the light power of a resonant 3-port-grating cavity ($\Phi = 0^\circ$) in $\eta_{2\min}$ -configuration as a function of ρ_0^2 . It can be seen that for $\rho_0^2 = \rho_2^2$ the internal power build-up is maximized. Hence the transmitted power is maximized as well in this configuration. In contrast to the two mirror cavity case discussed before only half of the light is transmitted and the other half splits equally between forward and back reflected port. Due to the different coupling of a 3-port-grating coupler, the internal power buildup is a factor of two lower than in the two mirror cavity case. This can be easily understood when looking at the energy conservation constraints of the two different couplers:

$$1 = \rho_0^2 + 2 \cdot \eta_1^2, \quad (\text{for 3-port-grating}) \quad (2.52)$$

$$1 = \rho_1^2 + \tau_2^2 \quad (\text{for mirror}). \quad (2.53)$$

For a given reflectivity $\rho_0^2 = \rho_1^2$ the light that is coupled into the grating cavity via the 1st order diffraction amounts to only half of the coupling by transmission in a conventional cavity.

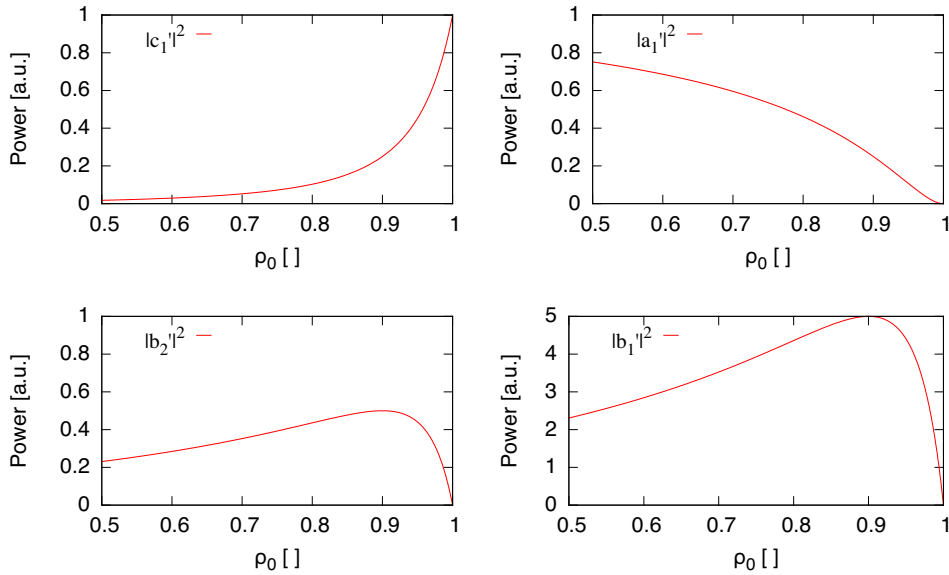


Figure 2.13 — Light power on resonance at the different ports of a 3-port-grating cavity in $\eta_{2\min}$ -configuration and $\rho_2^2 = 0.9$ as a function of ρ_0^2 . For $\rho_0^2 = \rho_2^2$ one half of the input light is transmitted through the cavity, while the other half is split equally to forward and back-reflected port, respectively. For this set-up the internal power buildup is maximized. Decreasing or increasing ρ_0^2 leads to a lower internal power build-up.

2.4 Experimental verification of binary 3-port-grating phase relations

In order to verify the phase relations of a symmetric 3-port-grating coupler derived in this chapter, two gratings with essentially the same 1st order diffraction efficiency but substantially different balancing between 2nd and 0th order diffraction efficiency have been designed and manufactured at the IAP in Jena. The gratings consist of a fused silica substrate with a dielectric multilayer stack made of alternating layers of Ta₂O₅ and SiO₂. Into the top-layer that was made of 880 nm SiO₂ a binary structure with a grating period of 1450 nm was etched by means of reactive ion beam etching. In order to reach the desired diffraction efficiencies the etching process was stopped after reaching a groove depth of 500 nm for the first grating (G1) and at 850 nm for the second grating (G2). For a detailed description of the manufacturing process see [49]. The measured diffraction efficiencies of the gratings G1 and G2 are given in Table 2.1. Note that the measurement of the diffraction efficiencies was done by using a conventional power-meter with an accuracy of $\approx 5\%$. Therefore the ports of the grating with a low diffraction efficiency were measured directly and all other grating parameters were determined using the identities given in equations (2.31) and (2.32). However it was also tested that the calculated values were within the error bars of the direct measurement.

	η_1^2	η_0^2	η_2^2
G1	0.10	-	0.15
G2	0.10	0.10	-

Table 2.1 — Measured diffraction efficiencies of G1 and G2

The experimental set-up that was used to verify the phase relation for these two exemplary gratings is shown in Figure 2.14. A diode pumped Nd:YAG non-planar ring oscillator (Model Mephisto from Innolight GmbH) was spatially filtered by a mode cleaner. The grating was illuminated in 2nd order Littrow configuration and formed a cavity with a conventional mirror with a transmission of $\tau_2^2 = 300$ ppm. The cavity length was controlled by a piezo-electrical-transducer (PZT), and the three output ports of the cavity were monitored using photodetectors (PD).

The measured data agrees very well with the theoretical predictions as shown in Figure 2.15 and 2.16. The small deviations that are present are probably due to imperfect mode matching that is not included in the theoretical model. Furthermore the theory postulates loss-less gratings. Hence any losses that are caused by residual transmission and scattering are not incorporated in the theoretical description. However, as predicted the asymmetric behavior around the resonance of the cavity can clearly be seen and therefore the phase relation derived in this chapter offer a valid model for the description of a binary 3-port-grating. For further details on the experimental verification see [50].

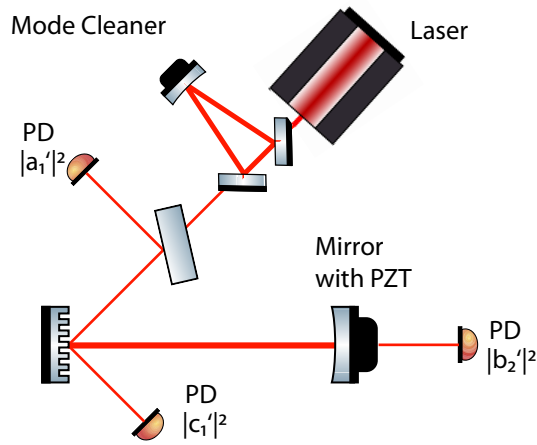


Figure 2.14 — Experimental set-up used to verify the phase-relations for binary 3-port-gratings.

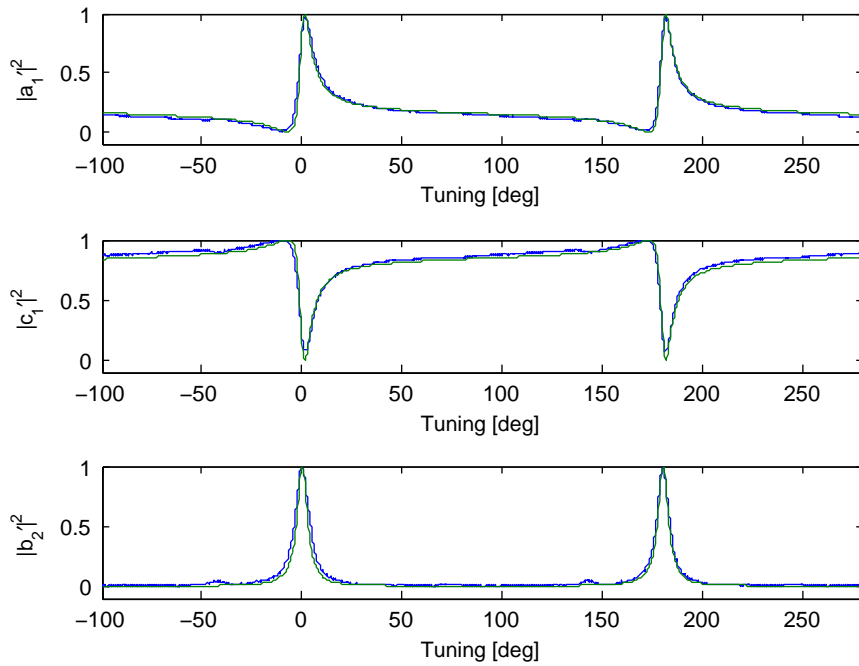


Figure 2.15 — Normalized power at the three output ports of a cavity formed by grating G1 and an end-mirror with $\tau_2^2 = 300$ ppm (blue trace). The cavity length was varied linearly with a PZT by more than one FSR. The theoretical predictions are plotted in green. Theoretical prediction and experimental data agree to a very high extent. The small deviations can be explained by imperfect mode matching of the incoming beam to the eigenmode of the cavity. Furthermore the theoretical model does not incorporate any optical loss of the grating.

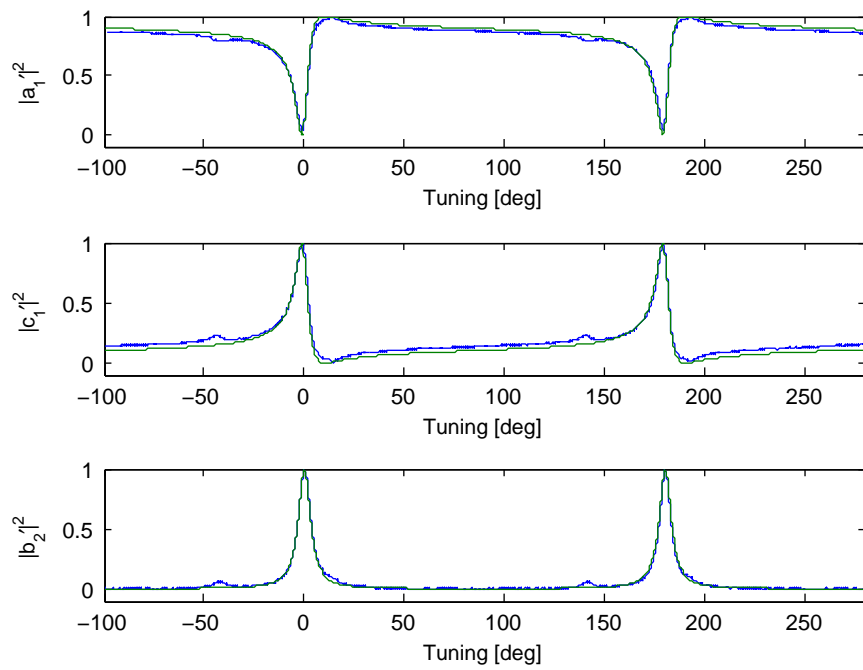


Figure 2.16 — Normalized power at the three output ports of a cavity formed by grating G2 and an end-mirror with $\tau_2^2 = 300$ ppm (blue trace). The cavity length was varied linearly with a PZT by more than one FSR. The theoretical predictions are plotted in green.

Control of 3-port-grating cavities

A widely used method for the stabilization of Fabry-Perot resonators is the Pound-Drever-Hall technique (PDH) [51]. In this chapter it will be shown, that this technique can be extended to be used for length control and stabilization of 3-port-grating cavities. Therefore the diffraction efficiency dependent phase relations between input and output ports have to be taken into account. In the first part of this chapter the theoretical background of PDH error signal generation for conventional mirror as well as 3-port grating cavities is presented. In the second part, the derived model for 3-port-grating cavities is validated for 3-port-grating couplers with different diffraction efficiencies.

3.1 Phase modulation and Pound-Drever-Hall technique

In order to stabilize the length of a resonator, the Pound-Drever-Hall technique is commonly used [51]. Therefore, phase-modulated sidebands are imprinted on the light field before entering the resonator. In general a sideband frequency of a few MHz is chosen such that it is typically well outside the line-width of the cavity. The light that is reflected at the cavity is detected by a photodetector and demodulated at the RF modulation frequency. The resulting error signal is a measure for the matching between the frequency of an eigenmode of the cavity and the frequency of the incident carrier light. Apart from being a measure of the detuning, it also contains information about the sign of the detuning. The resonance condition of the cavity can thus be maintained by feeding back this signal to an actuator via an appropriate electronic filter (servo). As discussed in chapter 2, not only the power at the two reflection ports of a 3-port-grating coupler depends on the balance of η_2 and η_0 but also the shape of the resonance peaks. This feature of 3-port-grating cavities affects the error signals needed for stabilization of the cavity, that will be derived in the following.

The electrical field of a laser beam at a fixed point in space can be written as:

$$E(t) = E_0 e^{i\omega_0 t}. \quad (3.1)$$

A phase modulation with an angular frequency of ω_m and modulation depth m yields:

$$E_{\text{PM}}(t) = E_0 e^{i\omega_0 t} e^{im \cos(\omega_m t)}. \quad (3.2)$$

Expanding into a series by using the identity given in [52] leads to

$$E_{\text{PM}}(t) = E_0 e^{i\omega_0 t} \sum_{k=-\infty}^{\infty} i^k J_k(m) e^{ik\omega_m t}, \quad (3.3)$$

where the J_k terms are the Bessel functions of the first kind of order k given by:

$$J_k(m) = \sum_{j=0}^{\infty} \frac{(-1)^j}{j!(j+k)!} \left(\frac{m}{2}\right)^{k+2j}, \quad (3.4)$$

$$J_{-k}(m) = (-1)^k J_k(m). \quad (3.5)$$

For small modulation indices ($m \ll 1$) equation (3.3) can be approximated by:

$$E_{\text{PM}}(t) \approx e^{i\omega_0 t} (J_0(m) + iJ_1(m)e^{i\omega_m t} + iJ_1(m)e^{-i\omega_m t}), \quad (3.6)$$

with the first terms of the Taylor series of the Bessel function being:

$$J_0(m) = 1 - \frac{m^2}{4} + \mathcal{O}(m^4), \quad (3.7)$$

$$J_1(m) = \frac{m}{2} - \frac{m^3}{16} + \mathcal{O}(m^5). \quad (3.8)$$

Therefore, phase modulation with a small modulation index m can be interpreted as the generation of sidebands with a frequency offset of $\pm\omega_m$ against the carrier and a phase shift of $i = 90^\circ$ each.

If the relative phase between the carrier and the sidebands remains unchanged, the terms at ω_m and $2\omega_m$ will be zero. The relative phase can be altered by interaction of the light field with an interferometer. Then the detected field contains information about the state of the interferometer and can be used to stabilize the system to a certain state.

3.2 Generation of error signals

Let us consider a modulated light beam a consisting of a carrier a_c and a lower and upper sideband a_l and a_u , respectively. In contrast to equation (3.2) the common factor $e^{i\omega_0 t}$ has been omitted:

$$a = a_c + a_l e^{-i\omega_m t} + a_u e^{i\omega_m t}. \quad (3.9)$$

If such a light field enters an interferometer the field components will change individually corresponding to the frequency dependent transfer function of the interferometer. The complex amplitude of the field at the output of the interferometer can be written as:

$$b = b_c + b_l e^{-i\omega_m t} + b_u e^{i\omega_m t}, \quad (3.10)$$

$$= G(\omega_0) a_c + G(\omega_0 - \omega_m) a_l e^{-i\omega_m t} + G(\omega_0 + \omega_m) a_u e^{i\omega_m t}, \quad (3.11)$$

with $G(\omega)$ being the frequency depend transfer function that is specified by the actual interferometer setup. The photo-current at a photodetector is proportional to the power of the light field rather than to the light field amplitude. Therefore, the output signal that is detected by a photodetector can be calculated by multiplying the light field amplitude with its complex conjugate. For the case of an unmodulated beam this will result in a DC signal representing the power of the beam. If the beam is phase modulated the signal will not only consist of DC terms for the carrier and the sidebands, but also of terms at the modulation frequency ω_m arising from the sidebands beating with the carrier and at $2\omega_m$ where the upper sideband beats with the lower one. Therefore the detected photo current I_{det} can be understood as:

$$I_{\text{det}} = |b|^2 = |b_c + b_1 e^{-i\omega_m t} + b_u e^{i\omega_m t}|^2 \quad (3.12)$$

This sum can also be written as a sum of five components [53]:

$$I_{\text{det}} = H_0 + 2H_{1p} \cos(\omega_m t) - 2H_{1q} \sin(\omega_m t) + 2H_{2p} \cos(2\omega_m t) - 2H_{2q} \sin(2\omega_m t), \quad (3.13)$$

where the following expressions were used:

$$H_0 = |b_c|^2 + |b_1|^2 + |b_u|^2, \quad (3.14)$$

$$H_{1p} = \Re\{b_1^* b_c + b_c^* b_u\}, \quad (3.15)$$

$$H_{1q} = \Im\{b_1^* b_c + b_c^* b_u\}, \quad (3.16)$$

$$H_{2p} = \Re\{b_1^* b_u\}, \quad (3.17)$$

$$H_{2q} = \Im\{b_1^* b_u\}. \quad (3.18)$$

Hence, H_0 yields the DC component of the detected photocurrent, whereas H_{1p} and H_{1q} represent the component of the photocurrent at ω_m . Here H_{1p} is the so called in-phase component, while H_{1q} is the quadrature component of the detected signal. Analogue, H_{2p} and H_{2q} are the in-phase and quadrature component of the detected signal at $2\omega_m$. In most cases one is only interested in the term at ω_m , which in the experiment has to be extracted from the other terms by demodulation at the modulation frequency. This can be done with the help of a mixer that electronically multiplies I_{det} by a local oscillator at the modulation frequency and thereby shifting all components at that frequency to DC. The phase of the local oscillator is called the demodulation phase χ_{dem} . Additionally a low pass filter after the mixer suppresses all higher frequency components so that only a linear combination of H_{1p} and H_{1q} remains as a function of the demodulation phase:

$$H_{\omega_m}(\chi_{\text{dem}}) = H_{1p} \cos(\chi_{\text{dem}}) + H_{1q} \sin(\chi_{\text{dem}}) = \Re\{(b_1^* b_c + b_c^* b_u) e^{-i\chi_{\text{dem}}}\}. \quad (3.19)$$

This signal can be used as a feedback signal to keep the resonator at the desired state and thus is often called error signal. In general one is not only interested in demodulating at one demodulation phase, since it is likely that the two quadratures contain different information about the state of the interferometer. Therefore one not only demodulates at χ_{dem} but also at $\chi_{\text{dem}} + 90^\circ$ in order to access the other quadrature. The quadratures are often referred to as in-phase and quadrature signal. In the following error signals will be derived for a two mirror cavity and a 3-port-grating coupled cavity.

3.2.1 Error signal of a two mirror cavity

In order to generate an error signal for a two mirror cavity, the incident light beam is phase modulated prior to the resonator. The light beam incident on the cavity can thus be described by:

$$a_{\text{in}} = (J_0 + iJ_1e^{-i\omega_m t} + iJ_1e^{i\omega_m t})a_0. \quad (3.20)$$

For a two mirror cavity the transfer function for the carrier in reflection G_r and transmission G_t of the cavity is given by:

$$G_r(\omega_0) = \frac{-\tau_1^2 \rho_2 e^{2i\Phi}}{1 - \rho_1 \rho_2 e^{2i\Phi}} + \rho_1, \quad (3.21)$$

$$G_t(\omega_0) = \frac{-\tau_1 \tau_2 e^{i\Phi}}{1 - \rho_1 \rho_2 e^{2i\Phi}}. \quad (3.22)$$

In order to derive the transfer function for the upper and lower sideband one has to replace the tuning factor for the carrier $\Phi = \omega_0 L/c$ by the corresponding value for the sidebands according to:

$$\Phi \Rightarrow \Phi_l = (\omega_0 - \omega_m)L/c, \quad (3.23)$$

$$\Phi \Rightarrow \Phi_u = (\omega_0 + \omega_m)L/c. \quad (3.24)$$

The transfer functions for the sideband fields are thus given by:

$$G_r(\omega_0 - \omega_m) = \frac{-\tau_1^2 \rho_2 e^{2i\Phi_l}}{1 - \rho_1 \rho_2 e^{2i\Phi_l}} + \rho_1, \quad (3.25)$$

$$G_t(\omega_0 - \omega_m) = \frac{-\tau_1 \tau_2 e^{i\Phi_l}}{1 - \rho_1 \rho_2 e^{2i\Phi_l}}, \quad (3.26)$$

$$G_r(\omega_0 + \omega_m) = \frac{-\tau_1^2 \rho_2 e^{2i\Phi_u}}{1 - \rho_1 \rho_2 e^{2i\Phi_u}} + \rho_1, \quad (3.27)$$

$$G_t(\omega_0 + \omega_m) = \frac{-\tau_1 \tau_2 e^{i\Phi_u}}{1 - \rho_1 \rho_2 e^{2i\Phi_u}} \quad (3.28)$$

With the knowledge of the transfer functions for carrier and sidebands, the error signal H_{ω_m} can be calculated using equation (3.19). Figure 3.1 shows H_{ω_m} as a function of the tuning Φ of a cavity, with $\rho_1^2 = 0.95$ and $\rho_2^2 = 0.99$. Demodulation in both quadratures is shown ($\chi_{\text{dem}} = 0^\circ$ and $\chi_{\text{dem}} = 90^\circ$). The calculations were done for a cavity length of $L = 10.64$ m and a modulation frequency of $f_{\text{mod}} = 10$ MHz. The modulation frequency was chosen to be well outside the line-width of the cavity. Note that the error signal at the reflection port shows a zero-crossing around the resonant tuning of the carrier for a demodulation phase of $\chi_{\text{dem}} = 0^\circ$, where the error signal in transmission is minimal for this setting. Demodulating with $\chi_{\text{dem}} = 90^\circ$ maximizes the signal in transmission. Since the error signal is generated by the beat between carrier and sideband, the overall signal level at the transmission port is significantly lower than at the reflection port. Analogue to the DC signal discussed in section 2.3.1, the error signal of a two mirror cavity is symmetric around the carrier resonance at $\Phi = 0$.

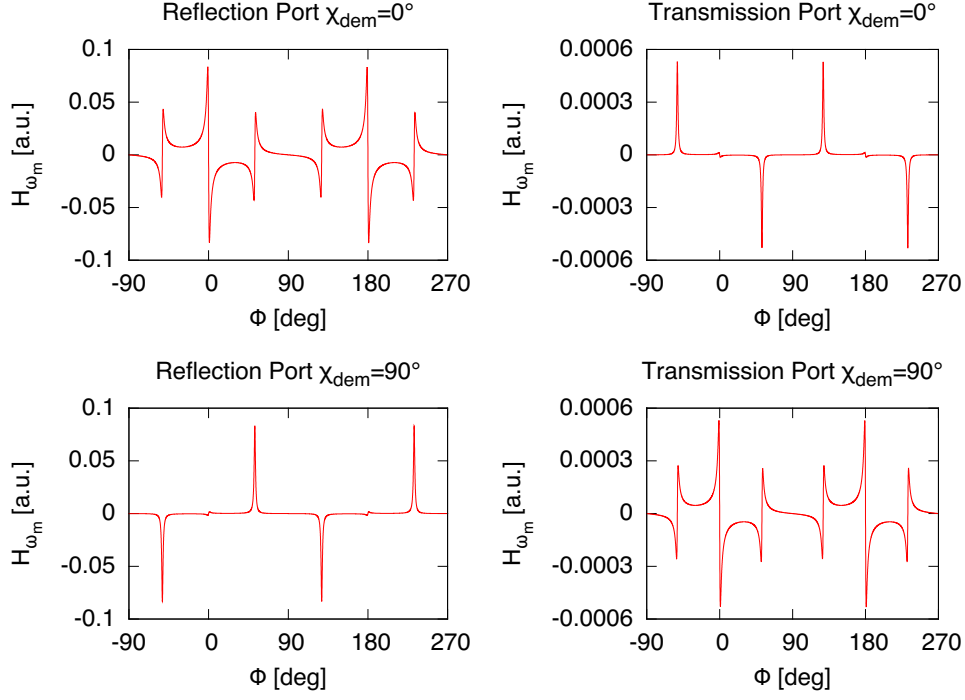


Figure 3.1 — Error signal at the transmission and reflection port of a two mirror cavity consisting of loss-less mirrors with $\rho_1^2 = 0.95$ and $\rho_2^2 = 0.99$. The modulation frequency of $f_{\text{mod}} = 10$ MHz is well outside the line-width of the cavity. The demodulation phase is chosen to be $\chi_{\text{dem}} = 0^\circ$ and $\chi_{\text{dem}} = 90^\circ$.

3.2.2 Error signal of a 3-port-grating coupled cavity

In order to calculate the error signal for a 3-port-grating coupled cavity, again a phase modulated input beam according to equation (3.20) is assumed. For a 3-port-grating cavity the transfer function of the carrier for the back reflection (G_{br}), forward reflection G_{fr} and transmission port G_t are given by:

$$G_{br}(\omega_0) = \frac{\eta_1^2 \rho_2 e^{2i(\Phi + \phi_1)}}{1 - \rho_0 \rho_2 e^{2i\Phi}} + \eta_2 e^{i\phi_2}, \quad (3.29)$$

$$G_{fr}(\omega_0) = \frac{\eta_1^2 \rho_2 e^{2i(\Phi + \phi_1)}}{1 - \rho_0 \rho_2 e^{2i\Phi}} + \eta_0, \quad (3.30)$$

$$G_t(\omega_0) = \frac{i\eta_1 e^{i\phi_1} \tau_2 e^{i\Phi}}{1 - \rho_0 \rho_2 e^{2i\Phi}} \quad (3.31)$$

The transfer functions for the upper and lower sideband result from replacing the factor for the carrier $\Phi = \omega_0 L/c$ by $\Phi_l = (\omega_0 - \omega_m)L/c$ and $\Phi_u = (\omega_0 + \omega_m)L/c$, respectively. The error signal can then be calculated according to equations (3.11) and (3.19). Just like the DC Signal discussed in section 2.3 also the error signal of the back and forward reflected port depend strongly on the balancing of η_0 and η_2 . In the following the

properties of the error signal of gratings with different balancing of η_0 and η_2 will be discussed.

Error signal for $\eta_2 = \eta_{2,\min}$

For a grating with $\eta_2 = \eta_{2,\min} = (1 - \rho_0)/2$ the DC signal of a grating coupled cavity H_0 of the forward and back reflected port behave just like the transmission and reflection port of a two mirror cavity. On resonance ($\Phi = 0^\circ$), H_0 of the back reflected port is maximal, while on anti-resonance ($\Phi = 90^\circ$) the DC signal is minimal. The forward reflection port behaves diametrically opposed and therefore analogue to the reflection port of a two mirror cavity. As seen in the previous section the error signal H_{ω_m} depends on the modulation phase. Figure 3.2 shows H_0 and H_{ω_m} for all three output ports of a grating cavity in $\eta_{2,\min}$ -configuration for a demodulation phase of $\chi_{\text{dem}} = 0^\circ$. Just like the two mirror cavity, the error signal of the 3-port-grating coupled cavity is symmetric around the carrier resonance $\Phi = 0^\circ$. Figure 3.3 shows the same signals for a demodulation phase of $\chi_{\text{dem}} = 90^\circ$. Analogue to the reflection and transmission port of a two mirror cavity, the error signal at the back and forward reflection port of the grating cavity are maximized in different quadratures. The DC signal as well as the error signal are always symmetric with respect to the carrier resonance at $\Phi = 0^\circ$.

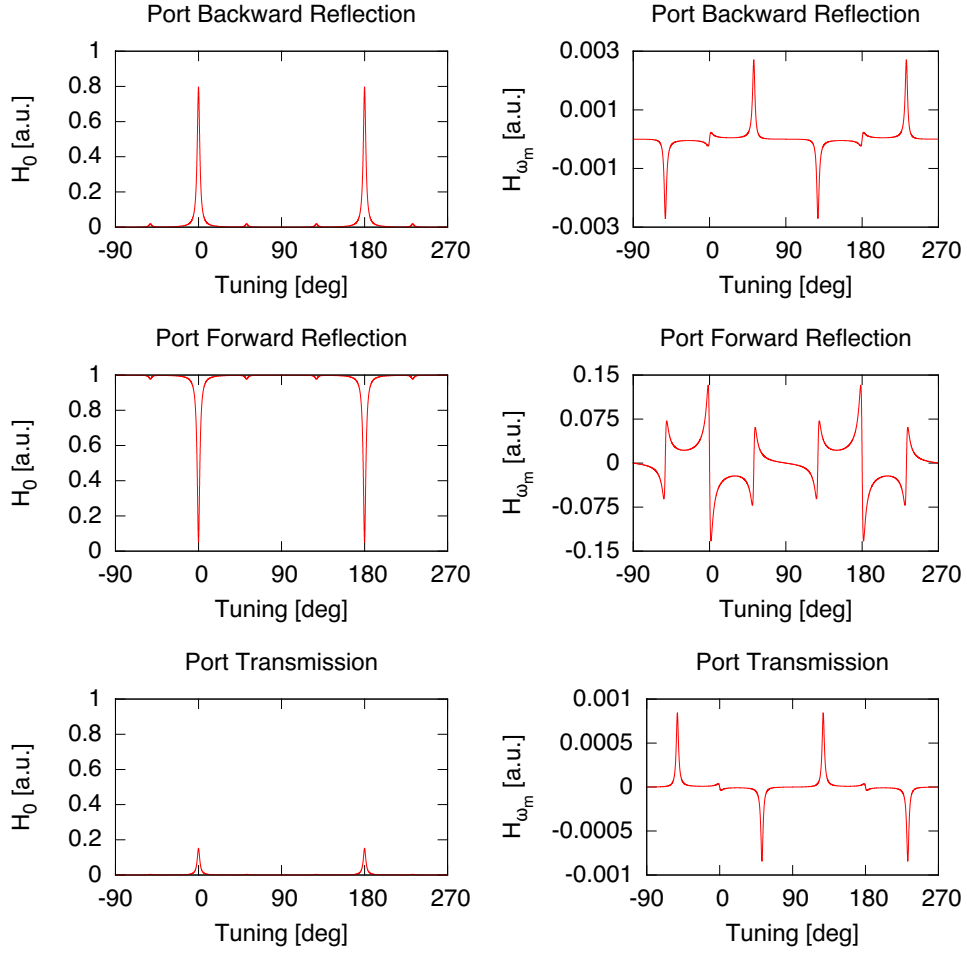


Figure 3.2 — DC signal H_0 and error signal H_{ω_m} for a 3-port-grating coupled cavity in $\eta_{2,\min}$ -configuration. The demodulation phase is chosen to be $\chi_{\text{dem}} = 0^\circ$. Cavity parameters: $L = 10.64$ m, $f_{\text{mod}} = 10$ MHz, $m = 0.3$, $\rho_0^2 = 0.9$, $\eta_1^2 = 0.05$, $\eta_2 = \eta_{2,\min}$, $\rho_2^2 = 0.99$.

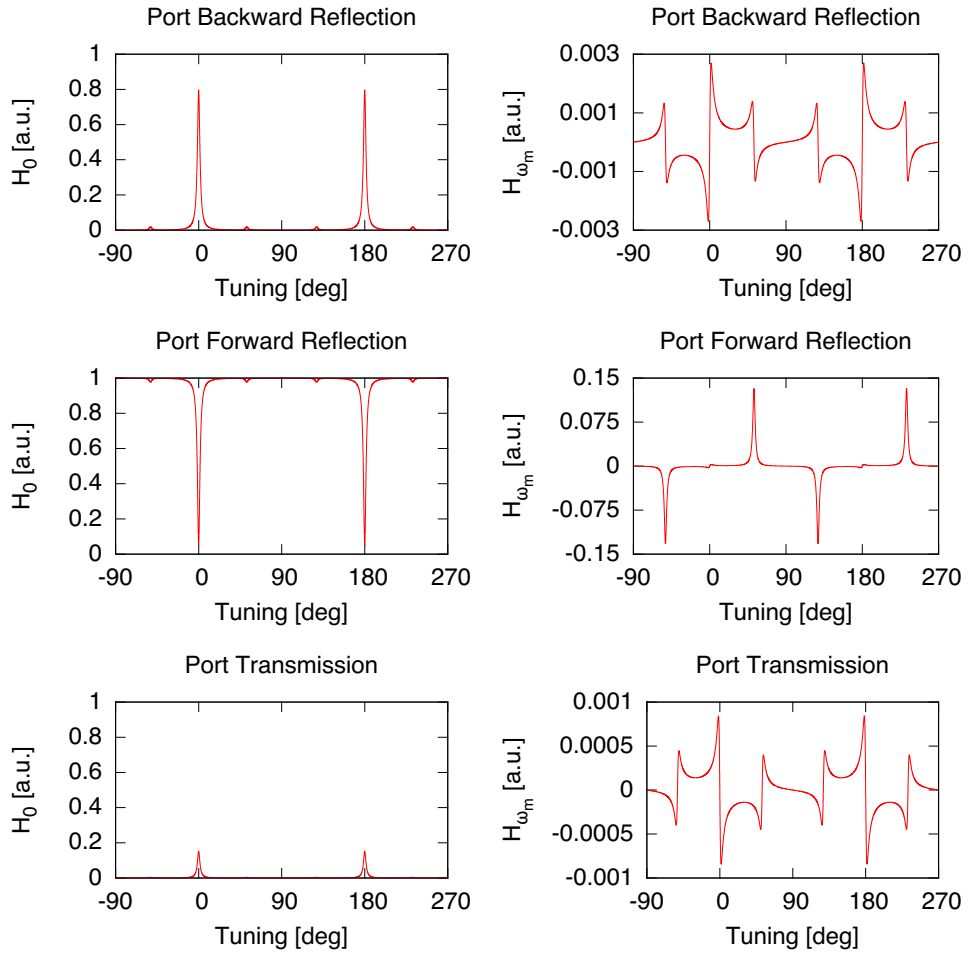


Figure 3.3 — DC signal H_0 and error signal H_{ω_m} for a 3-port-grating coupled cavity in $\eta_{2,\min}$ -configuration. The demodulation phase is chosen to be $\chi_{\text{dem}} = 90^\circ$. Cavity parameters: $L = 10.64$ m, $f_{\text{mod}} = 10$ MHz, $m = 0.3$, $\rho_0^2 = 0.9$, $\eta_1^2 = 0.05$, $\eta_2 = \eta_{2,\min}$, $\rho_2^2 = 0.99$.

Error signal for $\eta_2 = \eta_{2,\max}$

For a grating with $\eta_2 = \eta_{2,\max} = (1 + \rho_0)/2$ the signals at back and forward reflected port are interchanged. The DC signal H_0 and the error signal H_{ω_m} are shown in Figures 3.4 and 3.5 for demodulation in the two quadratures. Since the ports are just interchanged, the symmetry of DC and error signal is also present for this configuration. Obviously all signals at the transmission port are not affected by the different balancing between η_0 and η_2 and remain unchanged.

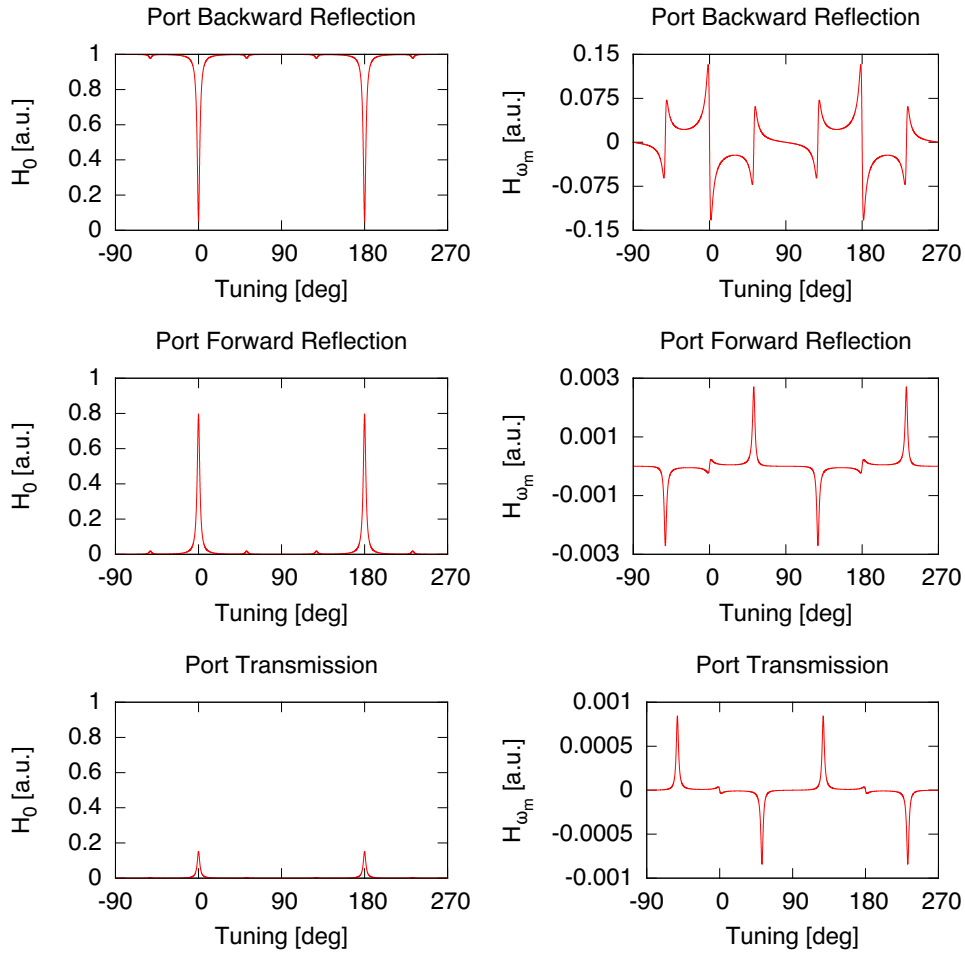


Figure 3.4 — DC signal H_0 and error signal H_{ω_m} for a 3-port-grating coupled cavity in $\eta_{2,\max}$ -configuration. The demodulation phase is chosen to be $\chi_{\text{dem}} = 0^\circ$. Cavity parameters: $L = 10.64$ m, $f_{\text{mod}} = 10$ MHz, $m = 0.3$, $\rho_0^2 = 0.9$, $\eta_1^2 = 0.05$, $\eta_2 = \eta_{2,\max}$, $\rho_2^2 = 0.99$.

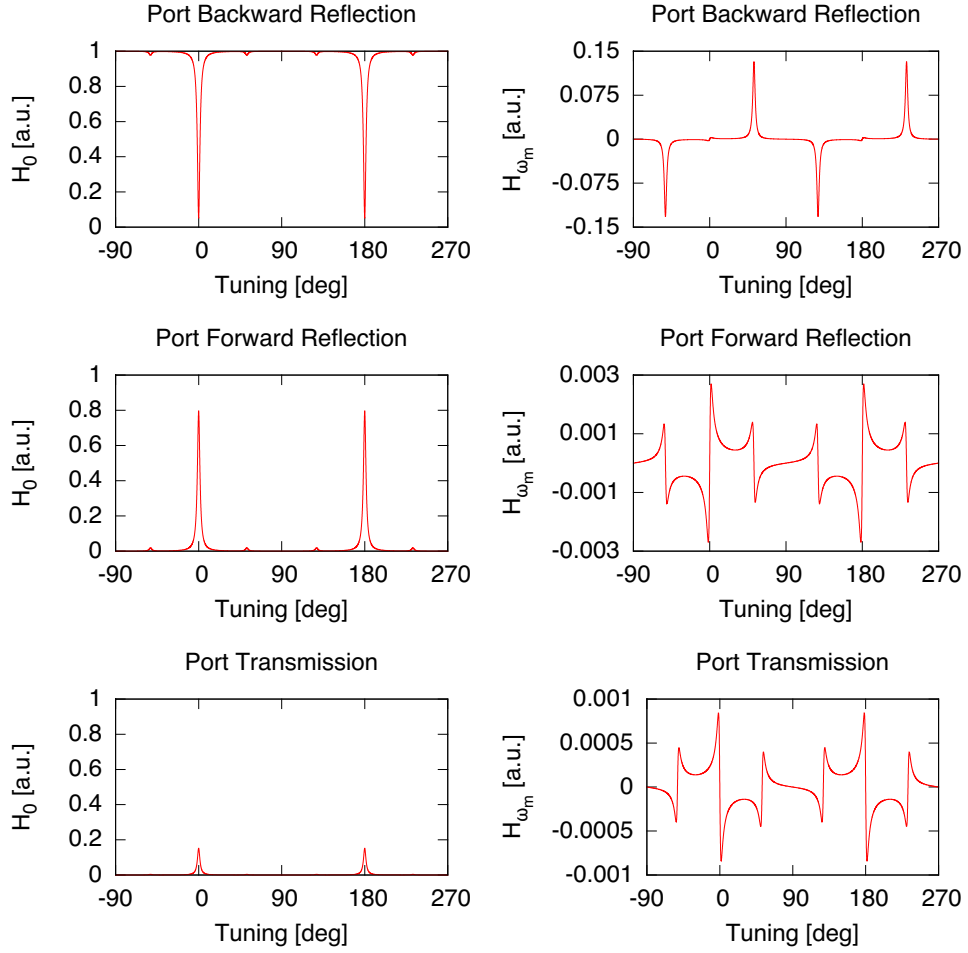


Figure 3.5 — DC signal H_0 and error signal H_{ω_m} for a 3-port-grating coupled cavity in $\eta_{2,\max}$ -configuration. The demodulation phase is chosen to be $\chi_{\text{dem}} = 90^\circ$. Cavity parameters: $L = 10.64$ m, $f_{\text{mod}} = 10$ MHz, $m = 0.3$, $\rho_0^2 = 0.9$, $\eta_1^2 = 0.05$, $\eta_2 = \eta_{2,\max}$, $\rho_2^2 = 0.99$.

Error signal for $\eta_2 = \eta_0$

For a grating with $\eta_2 = \eta_0$ the DC signal as well as the error signal will no longer be symmetric with respect to the carrier resonance at $\Phi = 0^\circ$. The asymmetric signals are shown in Figure 3.6 and 3.7 for demodulation of the two quadratures. For this configuration the zero crossing of the error signal is not at the resonance of the cavity $\Phi = 0^\circ$. Therefore, the error signal detected at either the forward or the back reflected port is not well suited to stabilize the cavity on resonance. However, summation of the error signals at the two ports results in a signal that is symmetric around $\Phi = 0^\circ$ and shows a zero crossing of the signal at the resonance of the carrier. Therefore, in order to generate a signal that is capable of stabilizing the system it is necessary to detect the sum of the error signals from both ports as depicted in Figure 3.8.

A slight asymmetry is also present for gratings that are designed to have diffraction efficiencies close to the extreme values. Since it is impossible to reach the theoretical limits in the manufacturing process, this asymmetry will appear for every grating. However, the degree of the asymmetry can be very small. For these gratings not the asymmetry of the error signal poses the problem but the fact that the zero crossing of the error signal is not exactly at $\Phi = 0^\circ$. In an experiment, this small deviation can be eliminated by applying an offset to the error signal in order to correct the point of the zero crossing. Therefore for gratings with very small η_2 , it is possible to use only the H_{ω_m} signal from one port as an error signal for the cavity control.

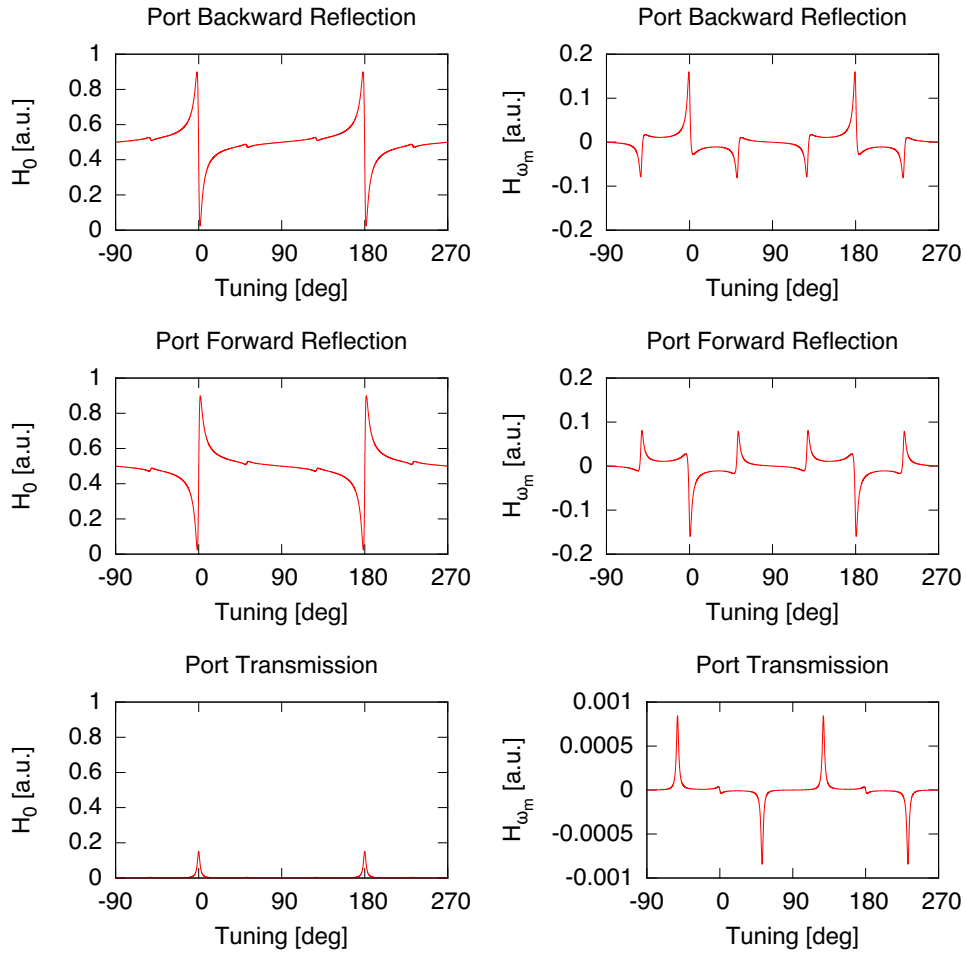


Figure 3.6 — DC signal H_0 and error signal H_{ω_m} for a 3-port-grating coupled cavity with $\eta_2 = \eta_0$. The demodulation phase is chosen to be $\chi_{\text{dem}} = 0^\circ$. Cavity parameters: $L = 10.64$ m, $f_{\text{mod}} = 10$ MHz, $m = 0.3$, $\rho_0^2 = 0.9$, $\eta_1^2 = 0.05$, $\eta_2^2 = \eta_0^2 = 0.475$, $\rho_2^2 = 0.99$.

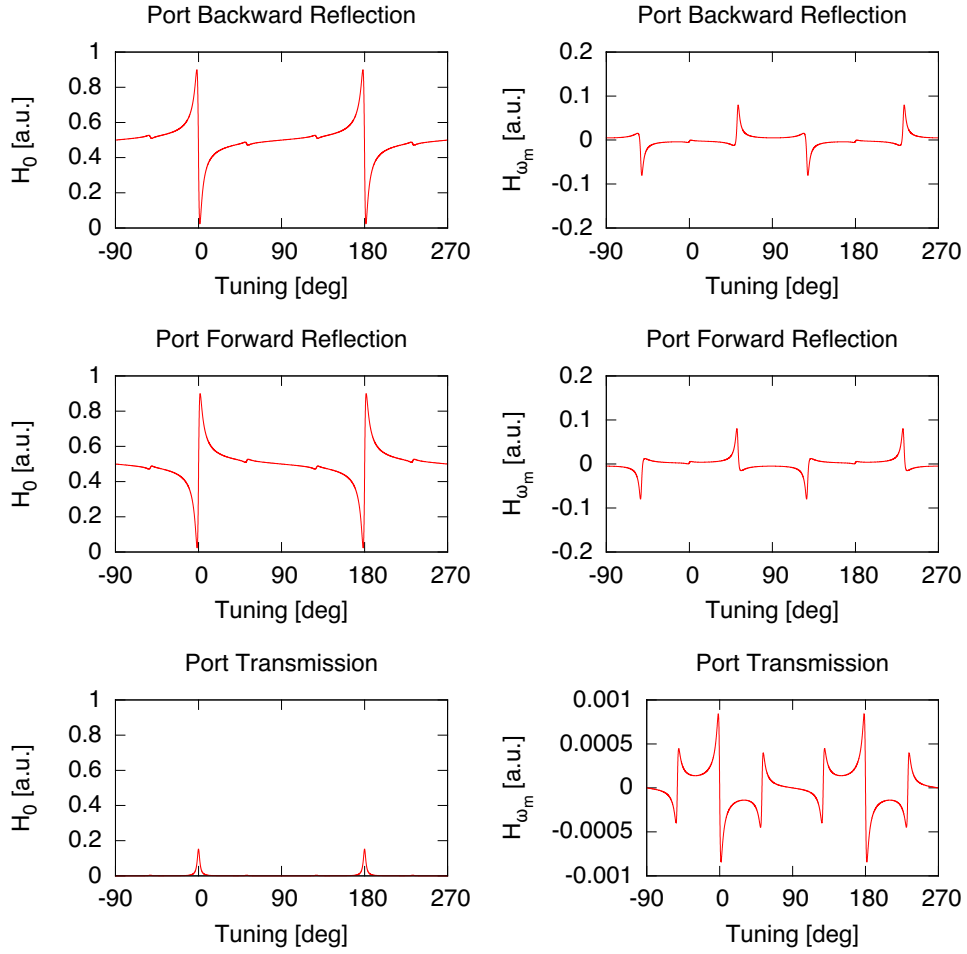


Figure 3.7 — DC signal H_0 and error signal H_{ω_m} for a 3-port-grating coupled cavity with $\eta_2 = \eta_0$. The demodulation phase is chosen to be $\chi_{\text{dem}} = 0^\circ$. Cavity parameters: $L = 10.64$ m, $f_{\text{mod}} = 10$ MHz, $m = 0.3$, $\rho_0^2 = 0.9$, $\eta_1^2 = 0.05$, $\eta_2^2 = \eta_0^2 = 0.475$, $\rho_2^2 = 0.99$.

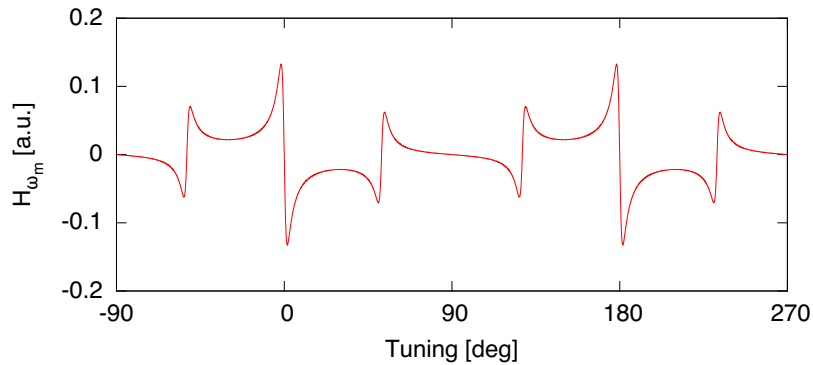


Figure 3.8 — The sum of H_{ω_m} at the forward reflected port and H_{ω_m} at the back reflected port results in a symmetric error signal, that can be used to control the cavity.

3.3 Experimental verification of error signal

In the following the implications of the 3-port-grating phase relations on the error signal of a 3-port-grating cavity, will be verified for gratings with different diffraction efficiencies. In the first part a grating was chosen that has an intermediate 2nd-order diffraction efficiency η_2 , which is far away from the upper and lower limit for the diffraction efficiency that was derived in Chapter 2. As discussed in the last section, this choice leads to an error signal at the reflection ports of the cavity, that shows a strong asymmetry with respect to the carrier resonance. In the second part a grating was chosen with a 2nd-order diffraction efficiency close to the lower boundary of diffraction efficiencies $\eta_{2\min}$. In this configuration the error signal at the reflection ports of the grating cavity only shows a small asymmetry.

3.3.1 Error signal with strong asymmetry

In order to verify that the 3-port-grating theory developed in section (2.2.2) leads to correct predictions for the error signal of a 3-port-grating coupled cavity, a grating with a large degree of asymmetry was designed and manufactured by the IAP in Jena. Therefore the grating design was chosen such that the 2nd order diffraction efficiency is far away from the upper and lower boundaries that could be determined by the scattering matrix of a 3-port-grating. Initially the grating was characterized via a Finesse measurement using the standard set-up discussed in [43] leading to the diffraction efficiencies given in table 3.1.

Parameter	Measured Value
η_0^2	78.242(± 4.01) %
η_1^2	1.710(± 0.088) %
η_2^2	19.470(± 0.950) %
ρ_0^2	96.451(± 0.113) %
Loss	0.129(± 0.175) %

Table 3.1 — Measured diffraction efficiencies of a 3-port-grating that was used to validate the error signal asymmetry predicted by the grating phase relations.

The laser light at a wavelength of 1064 nm from a commercially available light source (Model Mephisto from InnoLight) was spatially filtered using a mode-cleaner [54]. The light was phase modulated at a frequency of $f_{\text{mod}} = 15$ MHz by an electro-optical modulator (EOM). This frequency is well outside the measured linewidth of the cavity of $\text{FWHM} = 1.94 \pm 0.06$ MHz. The light was detected at all three output ports of the cavity and demodulated at the modulation frequency and low pass filtered. A schematic of the experimental set-up is shown in Figure 3.9. In order to adjust the signal strength at the forward and back reflected port for the summation a polarizing beam splitter and a $\lambda/2$ -plate is placed in front of each photodetector.

Figures 3.10 and 3.11 show a comparison between modeled and measured error signals at all three output ports of the cavity.

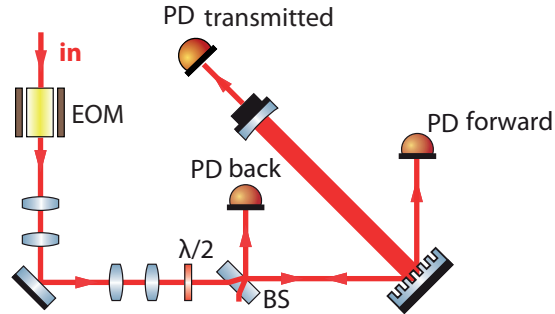


Figure 3.9 — Experimental setup used to validate the predicted asymmetry of the error signals due to the non-extreme values of η_0 and η_2 .

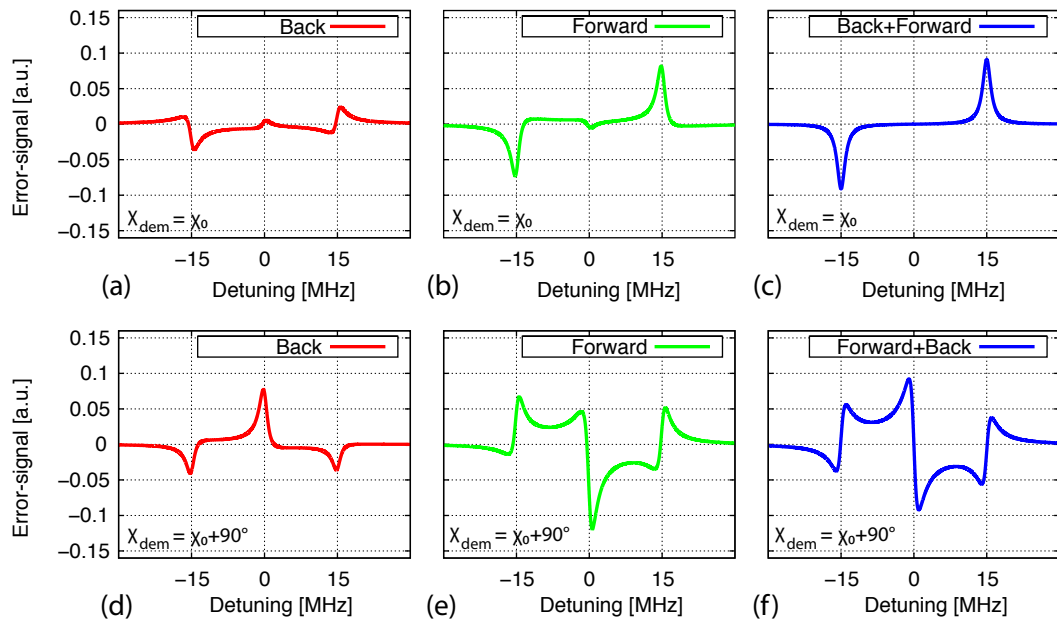


Figure 3.10 — Calculated error signals at the back-reflected port (left column) and forward reflected port (center column). The sum of the two signals (right column) leads to a proper error signal with a zero crossing at the resonance of the cavity.

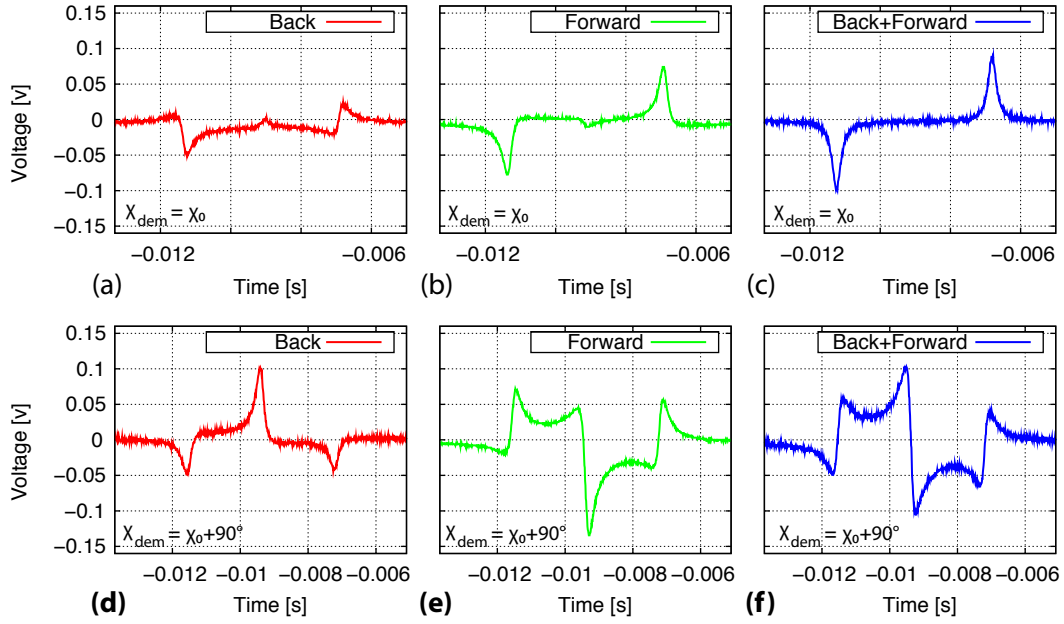


Figure 3.11 — Measured error signals at the back-reflected port (left column) and forward reflected port (center column). The sum of the two signals (right column) leads to a proper error signal with a zero crossing at the resonance of the cavity.

3.3.2 Error signal with small asymmetry

In the following the error signal of a 3-port-grating cavity composed of a grating with a very small 2nd order diffraction efficiency η_2^2 will be compared with the theoretical model. The diffraction efficiencies for the 1st and 2nd order were determined using a direct measurement with a power meter. The reflectivity under normal incidence ρ_0^2 was obtained by measuring the finesse of a cavity composed of the grating and a well characterized end-mirror as described in [43]. The 0th order diffraction efficiency η_0^2 in 2nd order Littrow set-up was specified to match the energy conservation given in Equation (2.31). These investigations lead to the diffraction efficiencies given in Table 3.2.

Parameter	Measured Value
η_0^2	99.560(± 2.4) %
η_1^2	0.077(± 0.008) %
η_2^2	0.018(± 0.002) %
ρ_0^2	99.669(± 0.006) %
Loss	0.177(± 0.025) %

Table 3.2 — Measured diffraction efficiencies of 3-port-grating used to validate the error signal asymmetry predicted by the grating phase relations.

The experimental data for the following comparison of model and experiment were

recorded at the 10 m prototype at the Institute of Gravitational Research at the University of Glasgow. Some details on the experimental set-up at the Glasgow prototype are given in Chapter 4. For a detailed description of the infrastructure see [55]. A schematic of the experimental set-up is shown in Figure 3.12.

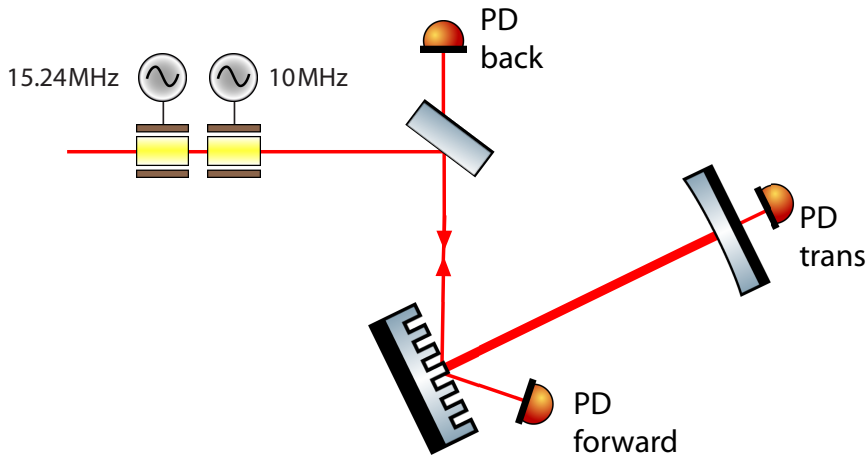


Figure 3.12 — Schematic of the experimental set-up.

To enable error signal extraction at all three ports of the grating cavity, the light was phase modulated at two modulation frequencies by two electro-optical modulators (EOM). The first modulation frequency was chosen to be $f_{\text{mod}_1} = 10$ MHz. This frequency is well outside the linewidth of the cavity, which could be determined to $\text{FWHM} = 13.80 \pm 0.64$ kHz. Therefore demodulation at this frequency generates a proper error signal at the forward and back reflected port of the cavity. In order to obtain an error signal at the transmission port of the 3-port cavity, the second modulation frequency $f_{\text{mod}_2} = 15.24$ MHz was chosen just off-resonance close to the $\text{FSR} = 15.27$ MHz of the cavity. In contrast to the previous experiment not the cavity length was scanned around the resonance state of the cavity, but the laser frequency was swept. This has the advantage that it does not risk causing alignment changes of the cavity, which could cause higher order modes to become excited thus distorting the pure error signals. A comparison between modeled and measured error signals is shown in Figure 3.13. The result indicates that the experimental data agrees very well with the theoretical predictions. To calibrate the demodulated signals detected at all three ports, the relative size of the in-phase slopes were compared to the slope of the signal from the transmitted port. The ratios of the signal response are presented in Table 3.3. The experimental data indicates a good quantitative agreement with the model, hence it can be stated, that generation for 3-port-grating cavities can be considered well understood.

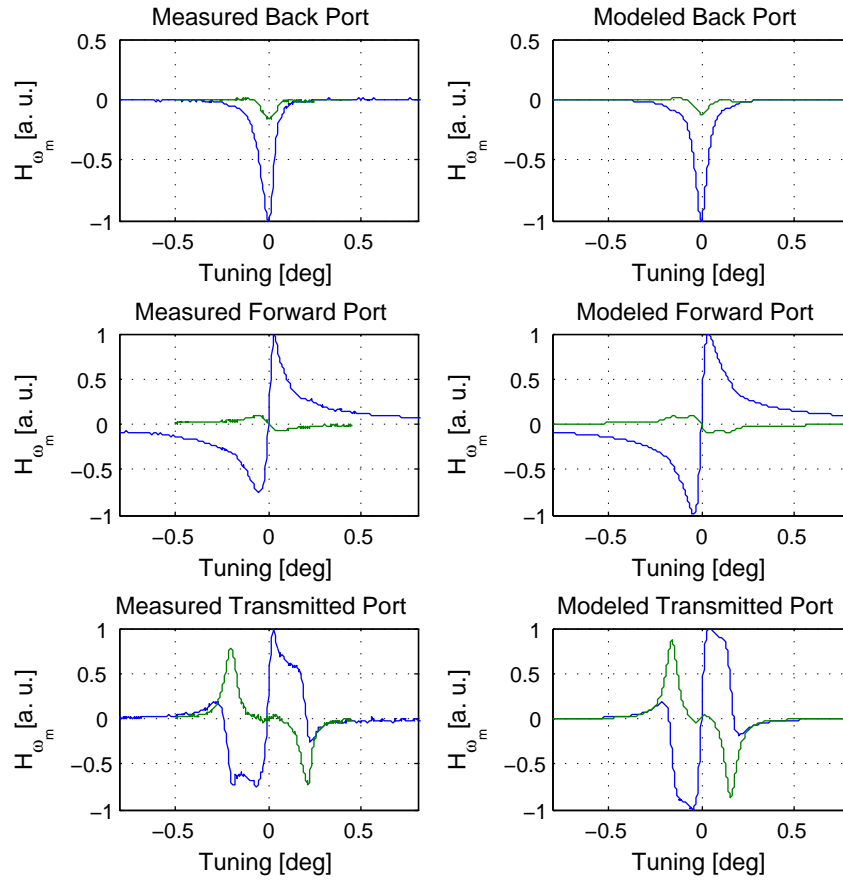


Figure 3.13 — Comparison of modeled and measured error signals. The blue trace represents the in-phase signal, and the green trace depicts the quadrature phase signal. The absolute scaling between back, forward and transmitted port is 2:1:163, respectively.

Parameter	Measured Value [dB]	Modeled Value [dB]
back/transmitted	-26.93	-22.51
transmitted/transmitted	0	0
forward/transmitted	43.07	44.74

Table 3.3 — The measured signal response shows the expected scaling relative to the transmitted port.

Side-motion induced phase noise in 3-port-grating cavities

A translational displacement of a grating parallel to its surface in direction perpendicular to the grating grooves will induce a phase shift proportional to the diffraction order [56]. In this chapter the coupling of this noise source in a 3-port-grating cavity is analyzed theoretically as well as experimentally. A theoretical model for the coupling of the side-motion induced phase noise to the length sensing signal of a 3-port grating cavity is derived, using a frequency-domain representation as well as a time-domain representation. At a fully suspended 3-port-grating cavity, the coupling of this noise source to the length sensing signal detected at the forward-reflected port of the cavity is measured. The experimental data shows an excellent agreement to the theoretical model. Therefore the noise coupling can be considered well understood.

4.1 Side-motion induced phase shift

Compared to conventional partly transmissive mirrors, diffraction gratings show a reduced symmetry. Mirrors like the ones that are used as test masses in gravitational wave detectors generally show a cylindrical symmetry. Therefore their roll movement does not affect the reflected light. In contrast plane diffraction gratings are merely invariant against translation parallel to the grating grooves, but they are certainly not invariant for rotation. The roll movement can be considered as an additional degree of freedom that needs to be taken into account in the design process of interferometers [58]. Furthermore also a translational displacement of the grating parallel to its surface in direction perpendicular to the grating grooves will induce a phase shift on the diffracted light. This phase change is due to a path length difference between parallel wavefronts and is given by [56]:

$$\Delta\phi = \Delta x \frac{m\lambda}{p}, \quad (4.1)$$

with m denoting the diffraction order and p the grating period. Figure 4.1 shows how the 1st order diffracted beam is affected by a lateral displacement of a grating in 2nd order Littrow configuration.

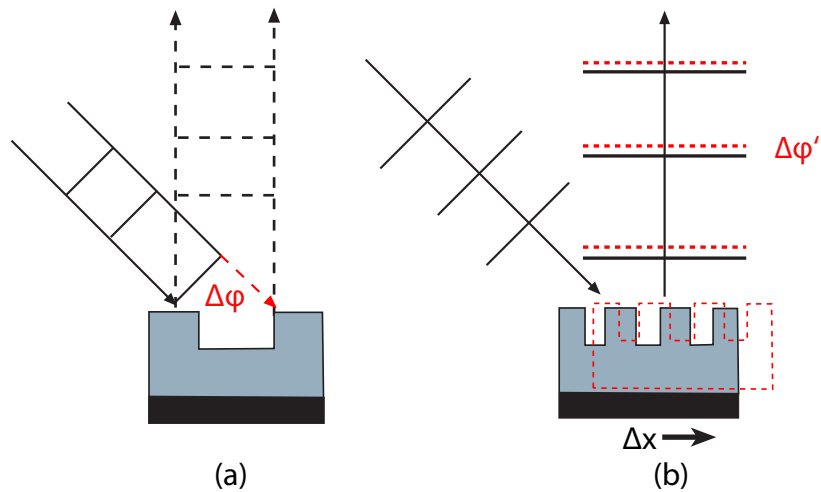


Figure 4.1 — (a) For 1st order diffraction, the angle of incidence is not equal to the output angle. The wavefronts are always perpendicular to the direction of propagation. In order to assure this, 1st order diffraction will introduce a phase shift that compensates the path length difference $\Delta\phi = \Delta x m \lambda / p$. (b) Due to this effect translation of the grating will lead to a phase shift $\Delta\phi'$, that is proportional to the displacement of the grating Δx .

4.2 Frequency-domain simulation

As long as the lateral displacement Δx of the grating is small compared to the grating period p , it is convenient to describe the coupling of the phase noise introduced by grating displacement in the frequency domain [57]. For a 3-port-grating we have to distinguish between two cases. The light can either be incident onto the grating in second order Littrow configuration as depicted in Figure 4.2 (a), or in case (b) under normal incidence. To begin with case (a) will be considered. An oscillating grating will

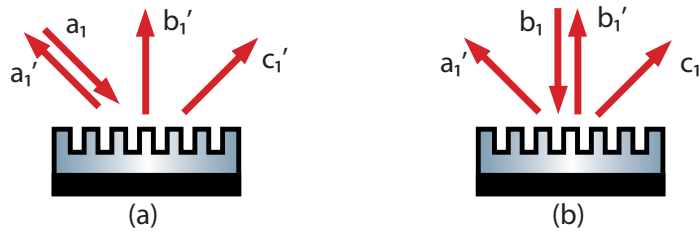


Figure 4.2 — Labeling of the ports of a 3-port-grating. For the lateral displacement of a 3-port-grating two cases have to be distinguished: (a) incidence in 2nd order Littrow configuration and (b) normal incidence.

phase modulate the light field that is diffracted in the 1st diffraction order. The light fields at the grating are thus related as:

$$b'_1 = \eta_1 e^{i\phi_1} e^{-im \cos(\omega_m t)} \cdot a_1, \quad (4.2)$$

with ω_m denoting the angular frequency of the lateral oscillation of the grating. The complex field amplitude can be expanded using the Bessel function $J_k(m)$ as described in Chapter 3. For $m \ll 1$ only the terms linear in m have to be considered, leading to:

$$b'_1 = \eta_1 e^{i\phi_1} \cdot a_1 \left(1 + i \frac{m}{2} e^{i\omega_m t} + i \frac{m}{2} e^{-i\omega_m t} \right). \quad (4.3)$$

When the grating is laterally oscillated to a maximum displacement Δx the modulation index is given by:

$$m = \frac{2\pi\Delta x\mu}{p}. \quad (4.4)$$

Therefore the complex field amplitude of the first order diffracted beam can be written as:

$$b'_1 = \eta_1 e^{i\phi_1} \cdot a_1 \left(1 + i \frac{\pi\Delta x\mu}{p} e^{i\omega_m t} + i \frac{\pi\Delta x\mu}{p} e^{-i\omega_m t} \right). \quad (4.5)$$

The lateral oscillation of the grating generates phase modulation sidebands. The amplitude of the sidebands generated by 1st order diffraction in 2nd order Littrow configuration is given by:

$$s_1 = i \frac{\pi \Delta x}{p} \eta_1 e^{i\phi_1} \cdot a_1. \quad (4.6)$$

Since the modulation index is proportional to the diffraction order μ , there will be no sidebands generated by a 0th order diffraction from port a_1 to c_1 . The 2nd order diffraction from port a_1 to a'_1 leads to a sideband amplitude of

$$s_2 = i \frac{2\pi \Delta x}{p} \eta_2 e^{i\phi_2} \cdot a_1. \quad (4.7)$$

In case (b) again 0th order diffraction occurs between ports b_1 and b'_1 and thus no sidebands are generated. Between b_1 and c'_1 -1st order diffraction occurs leading to a sideband amplitude of:

$$s_3 = -i \frac{\pi \Delta x}{p} \eta_1 e^{i\phi_1} \cdot b_1, \quad (4.8)$$

and for the first order diffraction between b_1 and a'_1 :

$$s_4 = i \frac{\pi \Delta x}{p} \eta_1 e^{i\phi_1} \cdot b_1. \quad (4.9)$$

In order to determine the coupling of the side motion induced sidebands to the output ports of a 3-port cavity, the description deduced in Section 2.3 needs to be expanded by three additional internal inputs. At these internal inputs the side motion induced sidebands enter the system (see Figure 4.3). To incorporate these additional

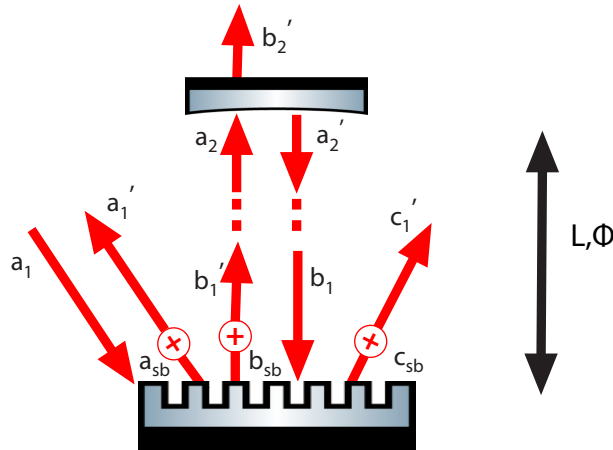


Figure 4.3 — Lateral displacement noise sidebands are entering the system at the internal input ports a_{sb} , b_{sb} and c_{sb} .

inputs, the fields at the ports of the cavity given in Equations (2.48)-(2.51) need to be changed to:

$$a'_1 = \eta_2 e^{i\phi_2} \cdot a_1 + (\eta_1 e^{i\phi_1} a_1 + b_{sb}) d \rho_2 \eta_1 e^{i(\phi_1+2\Phi)} + a_{sb}, \quad (4.10)$$

$$b'_1 = \left[(\eta_1 e^{i\phi_1} + b_{sb}) e^{i\Phi} d \right] \cdot a_1, \quad (4.11)$$

$$c'_1 = \eta_0 \cdot a_1 + (\eta_1 e^{i\phi_1} \cdot a_1 + b_{sb}) d \rho_2 \eta_1 e^{i(\phi_1+2\Phi)} + c_{sb}, \quad (4.12)$$

$$b'_2 = (\eta_1 e^{i\phi_1} a_1 + b_{sb}) d e^{i\Phi} i\tau_2, \quad (4.13)$$

where $d = (1 - \rho_0 \rho_2 e^{2i\Phi})^{-1}$ is the resonance factor of the carrier. According to Section 2.3, the carrier field inside the cavity for no internal input ($b_{sb} = a_{sb} = c_{sb} = 0$) can be written as:

$$b_1 = \rho_2 \eta_1 e^{i(\phi_1+2\Phi)} d \cdot a_1, \quad (4.14)$$

with a_1 being of the form $a_1 = E_0 e^{i\omega_c t}$, where ω_c denotes the angular frequency of the incident carrier laser light. Using Equations (4.6)-(4.9) and (4.14) the sideband field amplitudes are given by:

$$a_{sb} = \left(i\eta_2 e^{i\phi_2} \frac{2\pi\Delta x}{p} + i\eta_1^2 e^{2i\phi_1} \frac{\pi\Delta x}{p} B_c \right) \cdot E_0, \quad (4.15)$$

$$b_{sb} = i\eta_1 e^{i\phi_1} \frac{\pi\Delta x}{p} \cdot E_0, \quad (4.16)$$

$$c_{sb} = -i\eta_1^2 e^{2i\phi_1} \frac{\pi\Delta x}{p} \cdot E_0, \quad (4.17)$$

where the abbreviation $B_c = \rho_2 e^{2i\Phi} \cdot d$ was used.

To determine the sideband field we consider the total field at the output ports of the cavity given by Equations (4.10),(4.12),(4.13). Since we are only interested in the sideband fields, the external input b_0 is set to zero. Therefore only the terms containing the internal inputs a_{sb}, b_{sb}, c_{sb} are left. Now we substitute Equations (4.15)-(4.17) for the internal inputs. Taking into account that the sideband fields have different frequencies ($\omega_u = \omega_c + \omega_m$ for the upper sideband and $\omega_l = \omega_c - \omega_m$ for the lower sideband), analogous to the previously defined B_c , we find the term describing the interaction of the upper sideband field with the cavity as:

$$B_u = \frac{\rho_2 e^{i\Phi_u}}{1 - \rho_0 \rho_2 e^{i\Phi_u}}, \quad (4.18)$$

with $\Phi_u = \omega_u L / c$ the effective tuning parameter for the upper sideband. The sideband field amplitude at the output ports of the cavity depending on the input amplitude E_0 is thus given by:

$$a'_1 = \left(i\eta_1^2 e^{2i\phi_1} \frac{\pi\Delta x}{p} (B_u + B_c) + i\eta_2 e^{i\phi_2} \frac{2\pi\Delta x}{p} \right) \cdot E_0, \quad (4.19)$$

$$c'_1 = i\eta_1^2 e^{2i\phi_1} \frac{\pi\Delta x}{p} (B_u - B_c) \cdot E_0, \quad (4.20)$$

$$b'_2 = -\tau_2 \eta_1 e^{i\phi_1} \frac{\pi\Delta x}{p} \frac{B_u}{\rho_2 e^{i\Phi_u}}. \quad (4.21)$$

Note that it can be shown, that for the lower sideband the magnitude of the sidebands at the output port is identical to the upper sideband case discussed here. It was shown in [57], that the forward-reflected port c'_1 shows the strongest suppression of the lateral phase noise in the gravitational wave channel. Therefore in the following only this detection port is taken into account. In order to read out these side motion induced sidebands the Pound-Drever-Hall technique as described in Chapter 3 can be used. Therefore the incident laser light is phase modulated at an RF frequency ω_{RF} using an electro-optical modulator. Given that in the sideband picture, that is valid for small modulation indices, it is assumed that the carrier light field remains constant. For small side motion modulation index it can also be assumed, that there are no sidebands of sidebands present, so that the RF sidebands are not affected by the lateral displacement of the grating. Therefore we only need to consider the beat between the constant RF sidebands and the side motion induced sidebands, in order to verify the lateral displacement noise at a 3-port-grating cavity. According to Equation (3.19) the relevant field is given by:

$$H(\omega_m) = \Re\{(c'_1(-\omega_{\text{RF}}) \cdot c'^*_1(\omega_m) + c'_1(-\omega_m) \cdot c'^*_1(\omega_{\text{RF}})) \cdot e^{-i\chi_{\text{dem}}}\} \\ + \Re\{(c'_1(-\omega_{\text{RF}}) \cdot c'^*_1(-\omega_m) + c'_1(\omega_m) \cdot c'^*_1(\omega_{\text{RF}})) \cdot e^{i\chi_{\text{dem}}}\}.$$

In Figure 4.4 this quantity is shown as a function of the side motion frequency $f_m = \omega_m / (2\pi)$ for exemplary grating cavity with a linewidth of ≈ 5 kHz. It can be seen, that the side motion induced phase noise increases linearly for frequencies well within the linewidth of the cavity. Therefore the phase noise can be distinguished from a purely longitudinal motion of grating or end mirror, because this motion leads to a frequency independent response for frequencies well inside the linewidth of the cavity. A longitudinal motion of the cavity components gives the same response as the interaction of a cavity with a gravitational wave as discussed in Chapter 6.

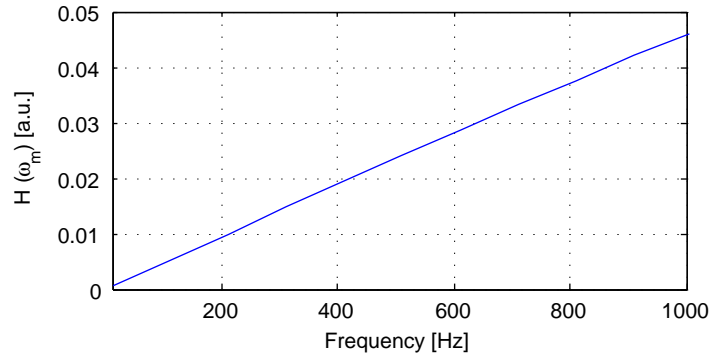


Figure 4.4 — Interaction between constant RF sidebands and side motion induced sidebands for exemplary grating cavity with a linewidth of ≈ 5 kHz. The side motion induced phase noise increases linearly with the frequency for frequencies well inside the linewidth of the cavity.

4.3 Time-domain simulation

For a large number of problems in interferometry, it is convenient to use a frequency domain representation. The widely used simulation tool Finesse[59] is completely based on the frequency domain approach. In frequency domain, generally the sideband picture is used, as it is described in chapter 3. In the sideband picture, phase modulation generates upper and lower sidebands that are frequency shifted with respect to the carrier by the modulation frequency. This approximation is only feasible if the modulation index of the phase modulation $m \ll 1$. A lateral displacement of a grating by one grating period results in a phase change of the 1st diffraction order of 2π . Therefore it is possible to reach a regime where the approximation used in the sideband picture are not valid anymore. As a consequence a time domain analysis offers the possibility to describe a grating set-up without relying on such approximations. Unfortunately with the experimental set-up used in the following, it was not possible to enter the regime of large lateral displacements. Nevertheless the frequency domain representation is presented here for the sake of completeness.

For convenience, throughout this chapter the 3-port-grating is described using the scattering matrix representation given in Equation (2.37). This scattering matrix can be parametrized by the parameters α, β and ϕ_{12} . The parameters α and β determine the diffraction efficiencies of 1st and 2nd order, via $\alpha = \eta_2$ and $\beta\sqrt{1-\alpha} = \eta_1$. Furthermore ϕ_{12} gives the phase shift associated with 1st order diffraction which is modulated due to a lateral motion of the grating. With the choice of these three parameters the scattering matrix is completely determined. This representation is beneficial for analyzing the side motion induced phase noise effects, because the phase change at the laterally displaced grating can be described by the scattering matrix directly just by changing the parameter ϕ_{12} . Note that the elements of the matrix corresponding to ± 1 st and 2nd diffraction order are linked according to

$$\arg(S_{12}) = -\arg(S_{23}), \quad (4.22)$$

$$\arg(S_{11}) = -\arg(S_{33}) \quad (4.23)$$

and therefore it is assured that the side motion induced phase shift is proportional to the diffraction order as it is demanded in [58].

In the following the coupling of the side motion induced phase noise to the three outputs of a 3-port-grating coupled cavity will be analyzed using a time domain simulation of the cavity. In a time domain analysis we can investigate how the light field inside the cavity evolves with time by taking a snapshot of the field at a given time t . The time difference T between subsequent snapshots is determined by the sampling frequency f_s :

$$T = \frac{1}{f_s}. \quad (4.24)$$

If the sampling frequency is chosen to be $f_s = c/L$, the points where the snapshots of the fields are taken, can be labeled as shown in Figure 4.5. The light field $b'_1(n)$

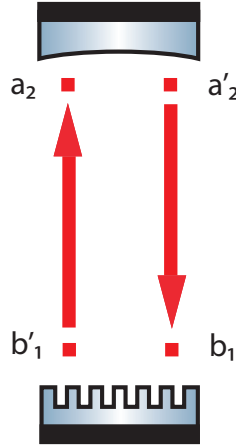


Figure 4.5 — Labeling of the amplitudes of a 3-port-grating cavity in a time domain simulation with a sampling frequency of $f_s = c/L$.

depicts the amplitude of the field directly at the grating inside the cavity at the time $t = n \cdot T (n \in \mathbb{N})$. The amplitudes inside the cavity full-fill the following relations:

$$b_1(n+2) = a'_2(n+1) \cdot \exp(i\Phi), \quad (4.25)$$

$$a'_2(n+1) = a_2(n+1) \cdot \rho_2, \quad (4.26)$$

$$a_2(n+1) = b'_1(n) \cdot \exp(i\Phi), \quad (4.27)$$

$$b'_1(n) = b_1(n) \cdot S_{22} + \eta_1 \exp(i\phi_{12}) a_1, \quad (4.28)$$

With the field inside the cavity at $n = 0$ which is given by:

$$b'_1(0) = \eta_1 \exp(i\phi_{12}) a_{in}, \quad (4.29)$$

every subsequent time step can be calculated. As long as the input field does not change with time, after several round-trips (the actual number of round-trips needed to reach the steady state depends on the finesse of the cavity) the cavity will be in a steady state and the field does no longer change with time. If the grating moves lateral in a sinusoidal fashion at frequency f_l , the phases ϕ_{11} and ϕ_{12} change with time, and therefore the light field inside the cavity is no longer independent of time. Here the modulation index m_l is defined such that an index of $m_l = 1$ corresponds to a lateral movement by one grating period, leading to a phase modulation of the first order diffracted beam of 2π . Hence the relevant phases of the scattering matrix are given as a function of time accordingly:

$$\phi_{12}(t) = m\pi \sin(2\pi f \cdot t) + m\pi \quad (4.30)$$

$$\phi_{11}(t) = 2\phi_{12}(t). \quad (4.31)$$

The field inside of the cavity will no longer reach a steady state and will oscillate depending on the lateral motion of the grating.

When the field is coupled out of the cavity, again a time- (respectively position-) dependent phase-shift occurs when the light field exits the cavity via the ± 1 st diffraction order of the grating. The resulting fields at the two output ports of the cavity is either a sum of 2nd or 0th order diffraction of the incoming light field and the light field coupled out of the cavity via the ± 1 st diffraction order of the grating, respectively. In the case of the back reflected port (2nd order diffraction of incoming light field + 1st order diffraction of internal cavity field), the directly back diffracted light is also affected by the side-motion induced phase shift, but the modulation index is doubled according to equation 4.31. At the forward reflected port, the 0th order diffracted beam of the incoming light, that does not get any side motion induced phase change, interferes with the -1st order diffracted field from inside the cavity.

Therefore the amplitude at the output ports of the cavity at the time $t = nT$ can be written as:

$$a'_1(n) = a_1(n) \cdot \eta_2 \exp(i\phi_{11}) + b_1(n) \cdot \eta_1 \exp(i\phi_{12}) \quad (4.32)$$

$$c'_1(n) = a_1(n) \cdot \eta_0 \exp(i\phi_{13}) + b_1(n) \cdot \eta_1 \exp(-i\phi_{12}) \quad (4.33)$$

$$b'_2(n) = a_2(n) \cdot i\tau_2 \exp(i\Phi). \quad (4.34)$$

The light power at each of the ports can be recorded as a time series by calculating the absolute squared of these amplitudes for each time step. In a real experiment, the cavity will always be stabilized on resonance and therefore the oscillations of the internal field will be cancelled to a certain extend by the feedback loop. However the signal will be present in the error signal that is used for stabilizing the cavity. If the cavity stabilization is done using the Pound-Drever-Hall scheme described in chapter 3, the input light field will be phase modulated at an RF frequency and can thus be written as:

$$a_1(n) = E_0 e^{im_{\text{RF}} \cos(\omega_{\text{RF}} nT)}, \quad (4.35)$$

with ω_{RF} and m_{RF} being angular modulation frequency and the RF modulation index, respectively. In order to access the error signal at a specific port the time series data needs to be demodulated by multiplication by a local oscillator at the RF frequency leading to the demodulated time series given by:

$$a'_{1\text{dem}} = |a'_1(n)|^2 \cos(\omega_{\text{RF}} nT + \chi_{\text{dem}}), \quad (4.36)$$

$$c'_{1\text{dem}} = |c'_1(n)|^2 \cos(\omega_{\text{RF}} nT + \chi_{\text{dem}}), \quad (4.37)$$

$$b'_{2\text{dem}} = |b'_2(n)|^2 \cos(\omega_{\text{RF}} nT + \chi_{\text{dem}}), \quad (4.38)$$

where χ_{dem} depicts the demodulation phase.

4.3.1 Generation of linear spectra

The simulated time series data can be used to get information about the spectral content of the signals at the different outputs of the cavity, by calculating a linear spectrum.

For this purpose the FFTW library [60] is used to calculate a Discrete Fourier Transform (DFT) of the time series data. From the Nyquist theorem it follows that the highest

useful frequency is $f_{Ny} = f_s/2$. In order to achieve the needed frequency resolution f_{res} the number of samples N have to be chosen so that

$$f_{res} = \frac{f_s}{N}, \quad (4.39)$$

is fulfilled. Since the DFT implicitly assumes that the finite time series repeats in a cyclic manner, it is very likely that there is a discontinuity between the last and the first sample. In order to assure a proper assignment of the spectral content of the time series to frequency bins of the DFT the time series data is multiplied with a window function before applying the DFT. The window function weighs the first and last samples of a time series to a different degree than samples in the middle of the time series. In this way the effect of the discontinuity can be decreased. A comprehensive overview on window functions can be found in [61]. For the following investigation a flat top window called SFT4 was chosen that consists of a weighted sum of cosine terms of the form [61]:

$$z = \frac{2\pi j}{N}, \quad j = 0 \dots N-1 \quad (4.40)$$

$$w_j = \sum_{k=0}^m c_k \cos(k \cdot z), \quad (4.41)$$

with the coefficients of the SFT4 window:

$$c_0 = 0.21706, \quad (4.42)$$

$$c_1 = -0.42103, \quad (4.43)$$

$$c_2 = 0.28294, \quad (4.44)$$

$$c_3 = -0.07897. \quad (4.45)$$

For the normalization of the spectra the window sum is needed:

$$S_1 = \sum_{j=0}^{N-1} w_j. \quad (4.46)$$

According to equation (23) in [61] the linear spectrum can be calculated by:

$$LS(f_m = mf_{res}) = \sqrt{\frac{2|y_m|}{S_1^2}}, \quad m = 0 \dots N/2, \quad (4.47)$$

with y_m being m -th element of the complex vector of length $N/2 + 1$ that is the output of the DFT calculation. Given that the loading process of the cavity is not of interest for this particular analysis the first time steps are not considered for the calculation of the spectra. In order to calculate the frequency response or transfer function several linear spectra are calculated, each of them for a lateral motion of the grating at a single frequency. The value of the linear spectrum at the specific modulation frequency is determined for each of the different simulations and plotted against the modulation frequency to get the transfer function. A transfer function of the lateral side motion noise to the error signal detected at the forward reflected port for a side motion modulation index of $m = 0.04$ is shown in Figure 4.6. Analogous to the previously discussed frequency domain representation, also the time domain method predicts a linear increase of the noise coupling with the frequency f .

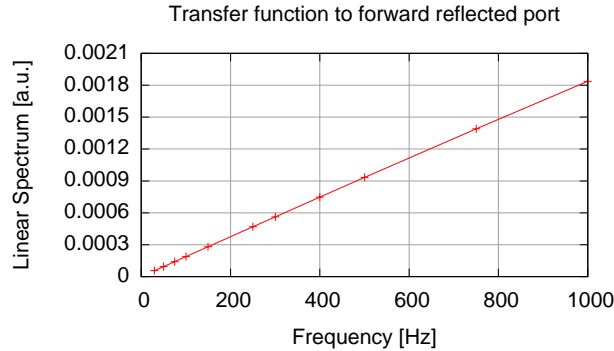


Figure 4.6 — The time domain representation also shows that for a fixed side motion amplitude of the grating the noise increases linearly with f .

4.4 Experimental verification of side motion phase noise

The following experiment was performed at the 10 m prototype [55] at the University of Glasgow. Apart from the input optics, every optical component in this system is suspended as a multi-stage pendulum similar to the ones used in GEO600 [12] to provide seismic isolation and allow freedom of motion. A schematic of the set-up is shown in Figure 4.7.

In order to investigate the side motion induced phase effects at a 3-port-grating, one arm of the prototype was commissioned as a diffractively coupled cavity. A 1×1 cm grating with a period of $p = 1450$ nm was etched on a standard 1" substrate, which was then overcoated with a high reflective multilayer system. The grating substrate was mounted on a jig, which was then attached to the suspended aluminum test mass as shown in Figure 4.8. The diffraction efficiencies of the grating are given in Table 3.2.

Two different methods were used to move the grating sideways, while the grating is held at resonance. For the first method, a magnet-coil actuator was attached to the side of the aluminum test mass as shown in Figure 4.9.

The displacement of the grating due to a fixed amplitude driving the magnet-coil actuator was measured using a laser-doppler vibrometer (Polytec Vibrometer with a OFV505 sensor head and a OFV5000 controller). The calibrated displacement measurement is shown in Figure 4.10.

Given that the test mass is suspended as a multi-stage pendulum, the amount of displacement for a fixed excitation at the coil drops off as $1/f^2$ above the pendulum resonance frequency. The achieved displacement of the grating over the frequency range shown is small compared to the grating period of 1450 nm and the approximation $m \ll 1$ is valid for this experimental set-up. Therefore the frequency domain representation can be used to model the coupling of the expected phase noise to the output port. Owing to the imperfect alignment of the magnet-coil actuator with respect to the center of mass of the test mass, the grating does not move perpendicular to the beam circulating inside the cavity. In order to produce a pure translational displacement a drive signal was applied

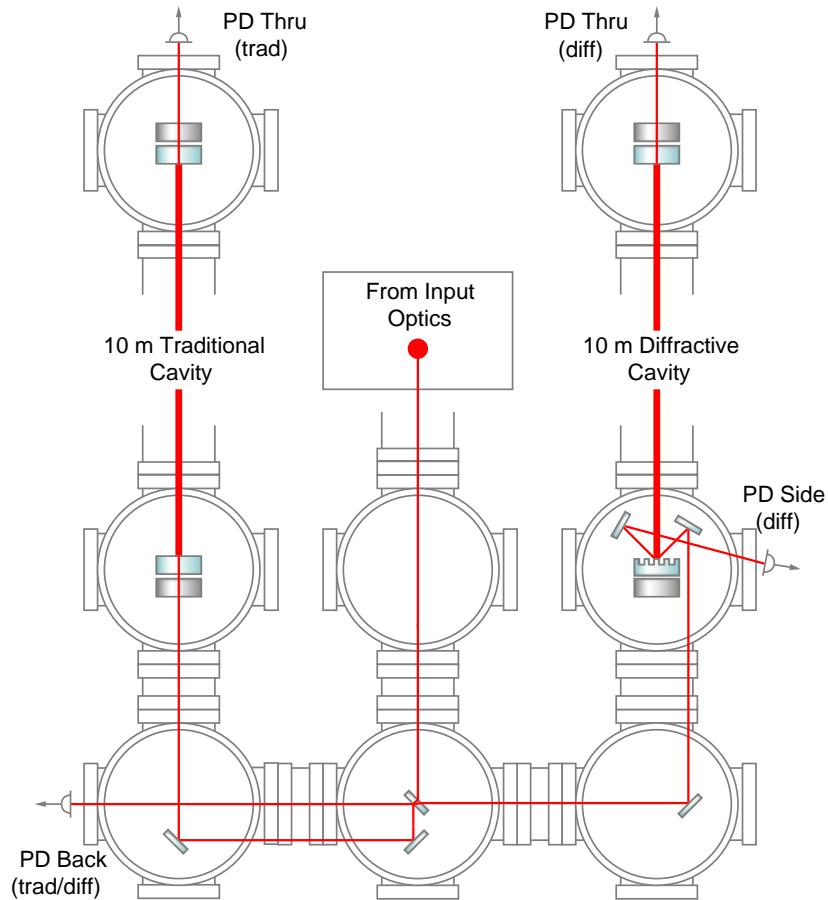


Figure 4.7 — Schematic of the set-up at the Glasgow 10 m prototype. One arm was commissioned as a diffractively coupled cavity.

to the side actuator and the back coils shown in Figure 4.11 (a) were adjusted to cancel any additional twisting and/or longitudinal motion introduced by the lateral actuator. For more details on the suspension design see [12].

Another method that could be used to introduce a lateral displacement of the grating perpendicular to the circulating beam is given by rotating the grating using the aforementioned back coils only (see Figure 4.11 (b)). By driving a rotational signal into the back coils, the mass is driven around the center of mass and translates the grating surface across the incident beam. Though this method produces a small amount of longitudinal motion, careful adjustment of the actuator strength to balance the rotation, leads to a reduction of the longitudinal component. For a proper balancing of the driving signals to the back coils, the translational component is the dominant feature on the detected signal. The coupling of this phase noise to the forward reflected port is observed using the demodulated signal (10 MHz) at the set-up shown in Figure 3.12. The measured coupling is compared to the frequency domain model in Figure 4.12. Since



Figure 4.8 — Picture of the suspended grating. The 1" substrate was mounted on a jig which was in turn attached to the aluminum test mass.

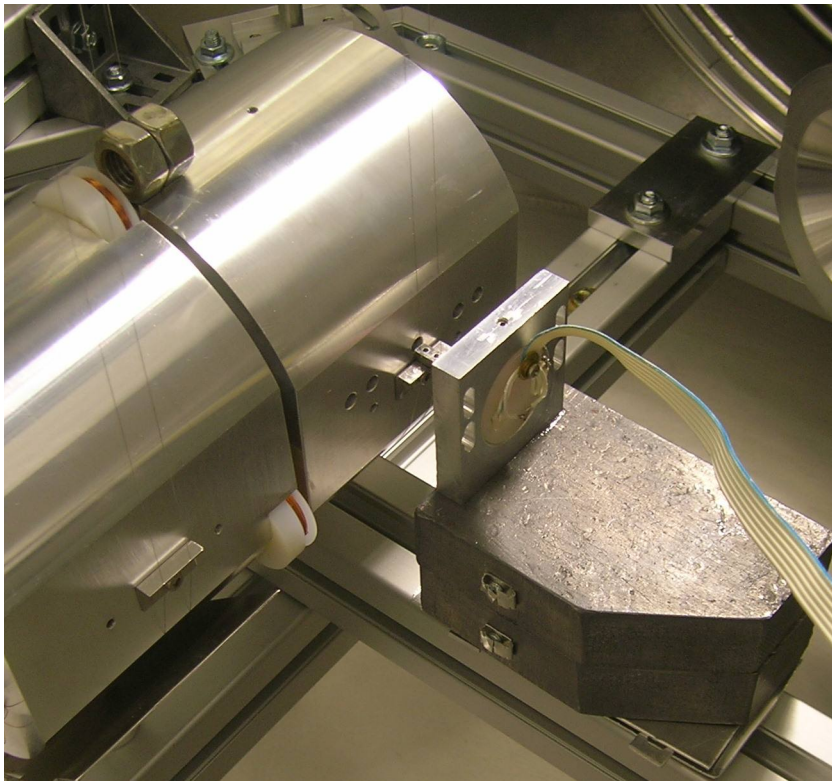


Figure 4.9 — Magnet-coil actuator for the side motion of the grating. A magnet was glued to the side of the aluminum test mass, and a coil was attached to a stack of lead and rubber blocks to isolate it from the frame of the suspension. By applying a periodic signal the whole test mass can be moved sideways.

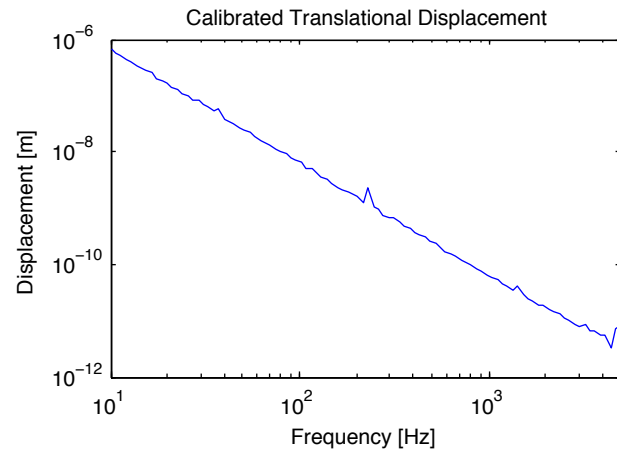


Figure 4.10 — Calibrated translational displacement measured with a laser-doppler vibrometer.

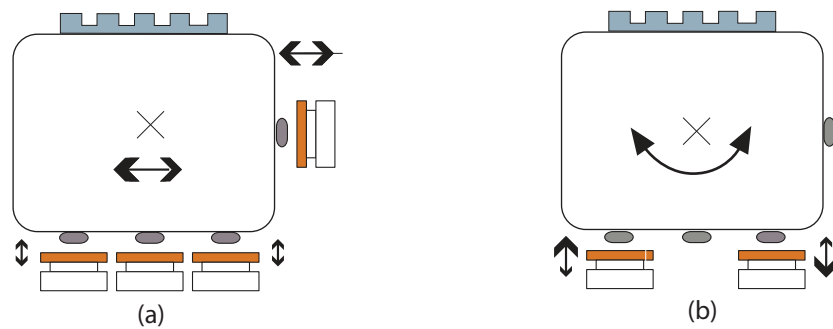


Figure 4.11 — (a) A magnet coil actuator was attached to the side of the test mass. The residual longitudinal motion can be compensated using the three coils that are attached to the back of the test mass. (b) Back coil actuation drives the mass rotationally causing side-to-side motion of the front surface. For proper balancing of the driving signal the small signal from longitudinal motion is dominated by the larger translational signal that is produced.

the displacement for a fixed amplitude driving falls off with $1/f^2$ due to the effect of the suspension, both actuation methods lead to a noise drop-off with a $1/f$ -slope. Both measurements agree very well with the theoretical prediction that was based on the frequency domain description derived in Section 4.2. The method using the magnet-coil actuator attached to the side of the test mass is only in agreement with the theoretical predictions in the low frequency part. Above 300 Hz the response is dominated by an internal mode of the aluminum test mass with a resonant frequency of ≈ 1.4 kHz [62]. While using only the back coils to generate the lateral displacement does produce a small excitation of this internal mode, the motion of the front surface is small in comparison to that produced by pure side driving. Thus the mode does not dominate the detected side signal response over the frequency range shown. Although this method naturally produces a smaller motion than the pure side method, it allows us to probe the coupling across a wider frequency range. The clear agreement between the theoretical prediction and experimental results indicates that the coupling of the is well understood.

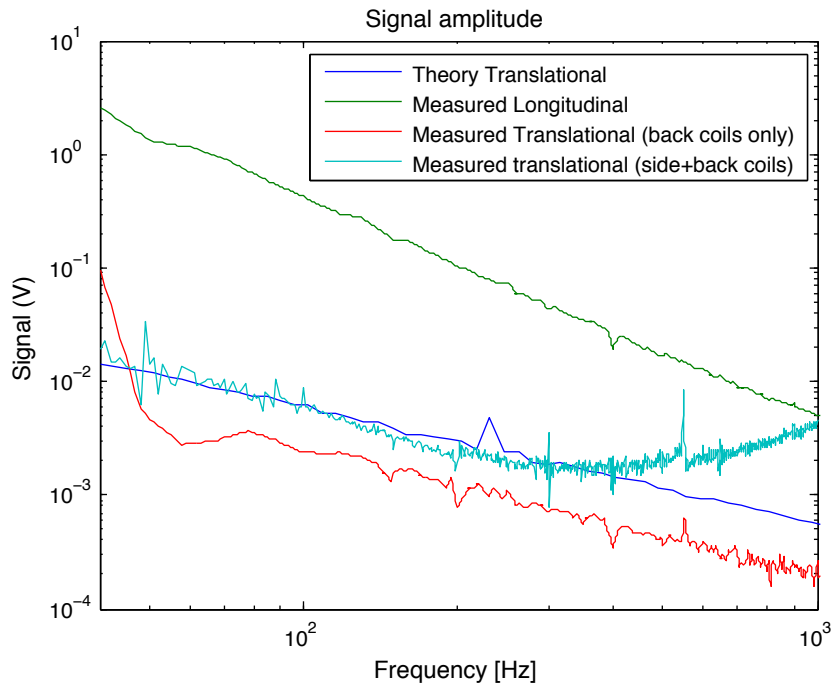


Figure 4.12 — Measured and predicted responses at the forward-reflected port for translational motion of the grating.

Power recycling

Fabry-Perot resonators are widely used in today's laser-interferometric gravitational wave detectors to increase the storage time of the light in the arms of a Michelson interferometer. In order to increase the sensitivity of such detectors even further, recycling techniques like power recycling are used, where a high reflecting mirror is placed between laser and Michelson interferometer, forming a linear three mirror cavity with the resonators in the arms of the interferometer [63]. In this chapter the implications on cavity properties are investigated when a 3-port-grating coupled cavity is used in a coupled set-up analogue to a linear three mirror cavity. In the first part of this chapter, the properties of power recycled 3-port-grating cavities are analyzed theoretically and compared to a linear three mirror cavity. In particular the impact of the balancing between η_2 and η_0 on the coupling between the two resonators is investigated. In the second part the experimental realization of a power recycled grating cavity with a low η_2^2 value is presented. It is shown, that power recycling can also be used to enhance the circulating power in a 3-port grating coupled arm cavity.

5.1 Two cavities coupled by a conventional mirror

The topology of a Michelson interferometer that uses recycling techniques can be quite complex. In order to understand the key components it is often useful to simplify the system by looking at only one arm of the interferometer. In this case power recycling can be understood as a linear three mirror cavity as shown in figure 5.1. In the following only the basic properties of three mirror cavities, that are necessary in order to point out similarities and differences to a 3-port-grating cavity, are presented. A comprehensive description of the properties of three mirror cavities can be found in [48].

The fields at the two ports of each mirror m_i are entitled a_i and b_i for the field propagating towards and a'_i and b'_i away from the mirror. This set-up consists of two coupled resonators with the first resonator being composed by the first and the second mirror (m_1 and m_2) and the second resonator is formed by the second and third mirror (m_2 and m_3). According to the possible application of such a coupled resonator set-up

in a gravitational wave detector the first cavity will be denoted as recycling cavity, while the second cavity is called arm cavity. Throughout this chapter it is assumed that all components are loss-less and that the incident light field matches the eigenmode of the resonator set-up perfectly.

The length of each cavity can be written as $L_i = \lambda(l_i + \Phi_i/(2\pi))$, where l_i is an integer denoting the macroscopic length of the cavity in multiples of the wavelength λ , and the tuning parameter Φ_i is restricted to the range $-\pi < \Phi_1 < \pi$ giving the microscopic length as a fractional part of the wavelength. The tuning Φ_i can therefore be interpreted as a measure for the phase delay due to the propagation of the light field along the cavity of length L_i . Throughout this investigation no signal or modulation sidebands are considered, so the integral part of the cavity length can be omitted. Thus, the phase change associated with one round-trip along the cavity is accounted for by multiplying the relevant field with the factor $\exp(2i\Phi_i)$. In order to understand the

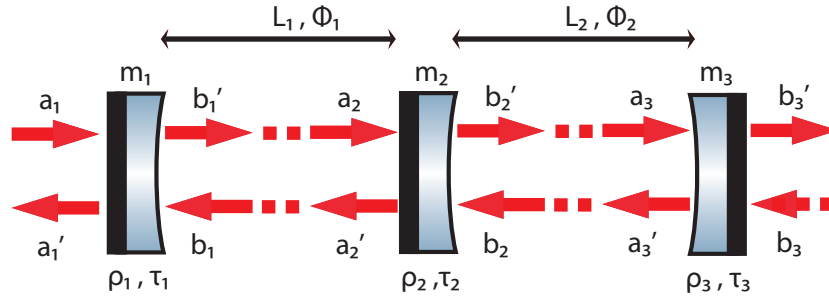


Figure 5.1 — Labeling of the fields at a three mirror coupled cavity

interaction between two resonators it is convenient to start with the fields at the second cavity assuming that there is only one input field at a_1 ($b_3 = 0$). The fields can thus be written as:

$$a'_2 = i\tau_2 b_2 + \rho_2 a_2, \quad (5.1)$$

$$b'_2 = i\tau_2 a_2 + \rho_2 b_2, \quad (5.2)$$

$$b_2 = \rho_3 e^{2i\Phi_2} b'_2. \quad (5.3)$$

Inserting equation 5.3 into 5.2 yields the field inside the second cavity:

$$b'_2 = CF_2(\Phi_1, \Phi_2) = \frac{i\tau_2}{1 - \rho_2 \rho_3 e^{2i\Phi_2}} a_2(\Phi_1). \quad (5.4)$$

This expression is equivalent to the well-known case of a two mirror cavity but a fundamental difference lies in the input field $a_2 = CF_1(\Phi_1, \Phi_2) e^{i\Phi_1}$. This field is the carrier field inside the first cavity, which is not constant because it depends on the detuning of both cavities Φ_1 and Φ_2 . As seen from m_1 the second cavity can be interpreted as a compound mirror with a reflection coefficient ρ_{m2m3} that can be derived from:

$$a'_2 = \underbrace{\frac{\rho_2 - \rho_3 e^{2i\Phi_2}}{1 - \rho_2 \rho_3 e^{2i\Phi_2}}}_{\rho_{m2m3}} CF_1(\Phi_1, \Phi_2) e^{i\Phi_1}. \quad (5.5)$$

The compound mirror reflectivity is a complex number that depends not only on the reflectivities of m_2 and m_3 but also on the detuning of the second cavity. Therefore the compound mirror reflectivity is not fixed but can be tuned by changing the detuning Φ_2 .

By using the compound mirror reflectivity $\rho_{m_2m_3}$, the field inside the first cavity is given by the well known equation for a two mirror cavity:

$$CF_1(\Phi_1, \Phi_2) = b'_1 = \frac{i\tau_1}{1 - \rho_1\rho_{m_2m_3}e^{2i\Phi_1}}a_1. \quad (5.6)$$

Therefore the field that is either reflected at or transmitted through the three mirror cavity can be written as:

$$\rho_{3MC} = \frac{\rho_1 - \rho_{m_2m_3}e^{2i\Phi_1}}{1 - \rho_1\rho_{m_2m_3}e^{2i\Phi_1}}a_1, \quad (5.7)$$

$$\tau_{3MC} = -\frac{\tau_2\tau_3e^{i\Phi_2}}{1 - \rho_2\rho_3e^{2i\Phi_2}}CF_1(\Phi_1, \Phi_2) \cdot e^{i\Phi_1}. \quad (5.8)$$

Analogue one can also find a similar expression for the compound mirror reflectivity of the first cavity consisting of m_1 and m_2 as seen from m_3 to be:

$$\rho_{m_2m_1} = \frac{\rho_2 - \rho_1e^{2i\Phi_1}}{1 - \rho_1\rho_2e^{2i\Phi_1}}. \quad (5.9)$$

The resonance of a two mirror cavity corresponds to the tuning $\Phi(\text{mod}\pi) = 0$, where the accumulated phase delay per round trip is $0(\text{mod}\pi)$. At this tuning the carrier field inside the resonator, and thus the field transmitted through the cavity, is maximized. Accordingly the resonance condition of a three mirror cavity corresponds to local maxima in the transmitted field. The round trip phase delay of the first resonator of a three mirror cavity is composed of the phase delay given by the round trip length of the cavity ($2L_1$) and the phase shift that is due to the reflection of the field at the second cavity ($\arg[\rho_{m_2m_3}(\Phi_2)]$). Therefore the resonance condition of the first cavity is given by:

$$\Phi_1^{\text{res}} = -\frac{1}{2}\arg[\rho_{m_2m_3}(\Phi_2)]. \quad (5.10)$$

In order to obtain the resonance state of the first resonator, the microscopic position of m_1 has to be chosen such that it compensates the phase shift due to the reflection of the field at the second cavity. Accordingly, the resonant tuning of the second cavity can be calculated as:

$$\Phi_2^{\text{res}} = -\frac{1}{2}\arg[\rho_{m_2m_1}(\Phi_1)]. \quad (5.11)$$

Figure 5.2 illustrates the resonance pattern of a three mirror cavity with mirror reflectivities chosen to be $\rho_1^2 = 0.7$, $\rho_2^2 = 0.8$ and $\rho_3^2 = 0.9$. The three dimensional plot shows the transmitted power (color coded) as a function of the tunings Φ_1 and Φ_2 . The resonance pattern is periodic in $\Phi_1 \text{mod}\pi$ and in $\Phi_2 \text{mod}\pi$ and point symmetric about the origin. The structure of the resonance pattern is dominated by two resonance branches given by the phase shifts in reflection of the two resonators (Equations 5.10) and (5.11). Figure 5.3

shows the compound mirror reflectivities according to equation (5.5) and (5.9) as a function of the tunings Φ_1 and Φ_2 , respectively. The global maximum of the transmitted power in Figure 5.2 is located at $\Phi_1 = -25^\circ$ and $\Phi_2 = -6.5^\circ$ and because of the present symmetry also at $\Phi_1 = 25^\circ$ and $\Phi_2 = 6.5^\circ$. For this set of tunings the compound mirror reflectivities of first and second resonator fulfill the condition:

$$|\rho_{m_2m_3}(\Phi_2)| = \rho_1, \quad (5.12)$$

$$|\rho_{m_2m_1}(\Phi_1)| = \rho_3. \quad (5.13)$$

At this operating point all the incoming light is transmitted through the three mirror cavity.

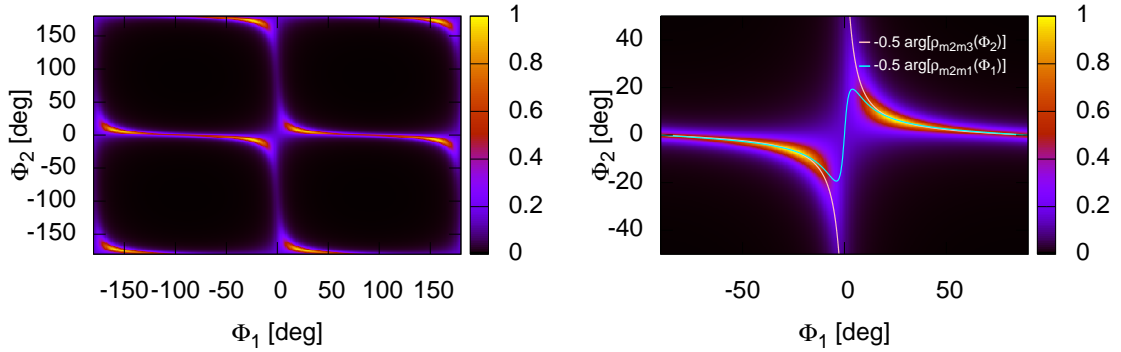


Figure 5.2 — Transmitted power at a three mirror cavity with $\rho_1^2 = 0.7$, $\rho_2^2 = 0.8$ and $\rho_3^2 = 0.9$ as a function of the tunings Φ_1 and Φ_2 . The resonance branches are determined by the phase needed to compensate the phase shift occurring at the reflection at each of the resonators. Note that the right figure contains the same information as the figure on the left apart from the different scaling that was used.

For the application in a gravitational wave detector the reflectivity of the end mirror m_3 is typically close to unity and the reflectivity of m_2 is chosen to obtain a desired bandwidth of the arm cavity. In order to obtain impedance matching the reflectivity of m_1 needs to be matched to $|\rho_{m_2m_3}|^2$ at the operating point of the arm cavity. A typical set of reflectivities that meet the requirements of the arm cavities in a gravitational wave detector is $\rho_2^2 = 0.95$ and $\rho_3^2 = 0.99995$. With this choice, impedance matching is obtained at $\rho_1^2 = 0.996$ for $\Phi_1 = 90^\circ$ and $\Phi_2 = 0^\circ$. For this parameter set the internal power inside the arm cavity will be enhanced compared to the non-recycled arm cavity (1 W input power, internal power in arm 78 W), by a factor of ≈ 256 to 20 kW in the arm cavity.

5.2 Two cavities coupled by a 3-port-grating

In the following investigation the second mirror of a three mirror cavity is replaced by a 3-port-grating. The fields at the several ports of the coupled set-up are labeled according

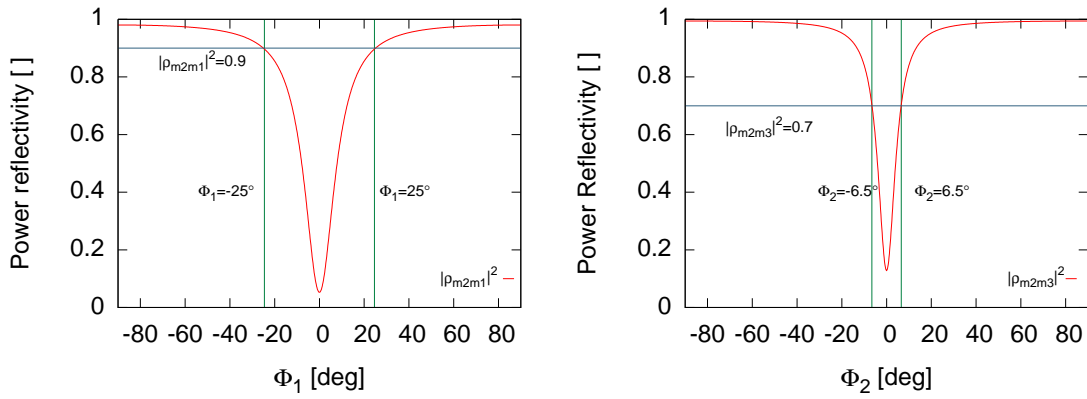


Figure 5.3 — Compound mirror power reflectivities $|\rho_{m2m1}|^2$ and $|\rho_{m2m3}|^2$ as a function of Φ_1 and Φ_2 , respectively. The global maximum of the transmitted power occurs at the set of tunings where the compound mirrors matches the reflectivity of the respective single mirror.

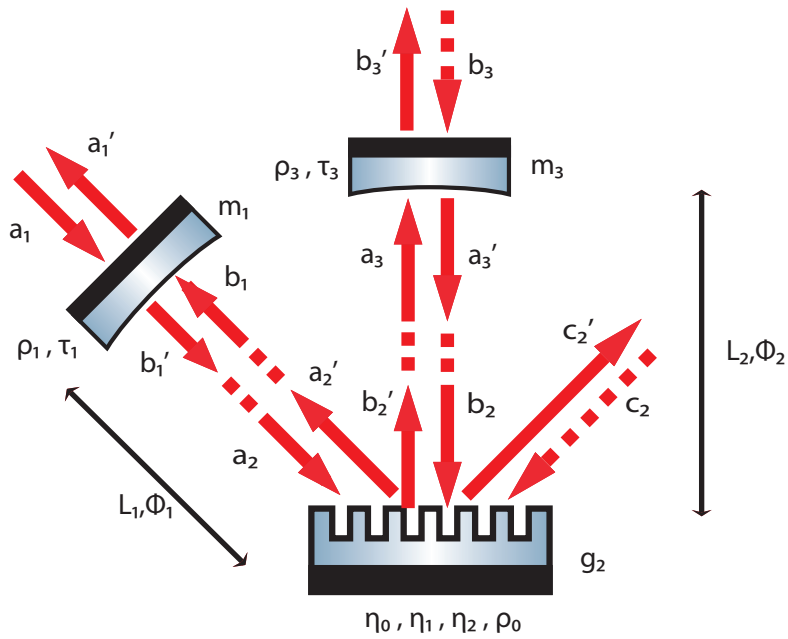


Figure 5.4 — Light-field amplitudes at a power recycled 3-port-grating cavity

to Figure 5.4. In analogy to the previous section the light fields at the arm cavity can be written as:

$$a'_2 = \eta_2 e^{i\phi_2} a_2 + \eta_1 e^{i\phi_1} b_2, \quad (5.14)$$

$$b'_2 = \eta_1 e^{i\phi_1} a_2 + \rho_0 b_2, \quad (5.15)$$

$$b_2 = \rho_3 e^{i\Phi_2} b'_2. \quad (5.16)$$

The carrier field inside the arm cavity can be derived as:

$$b'_2 = \text{CF}_2(\Phi_1, \Phi_2) = \frac{\eta_1 e^{i\phi_1}}{1 - \rho_0 \rho_3 e^{2i\Phi_2}} a_2. \quad (5.17)$$

Again the internal fields of both cavities are not independent of each other, and the compound mirror reflectivity of the second cavity ρ_{g2m3} can be derived from:

$$a'_2 = \underbrace{\left(\frac{\rho_3 \eta_1^2 e^{2i(\phi_1 + \Phi_2)}}{1 - \rho_0 \rho_3 e^{2i\Phi_2}} + \eta_2 e^{i\phi_2} \right)}_{\rho_{g2m3}} a_2. \quad (5.18)$$

By using the compound mirror reflectivity of the second cavity the carrier field inside the first cavity is given by:

$$b'_1 = \text{CF}_1(\Phi_1, \Phi_2) = \frac{i\tau_1}{1 - \rho_1 \rho_{g2m3} e^{2i\Phi_1}} a_1. \quad (5.19)$$

One can also derive the compound mirror reflectivity of the first cavity consisting of m_1 and g_2 :

$$\rho_{g2m1} = \frac{\rho_1 \eta_1^2 e^{2i(\phi_1 + \Phi_1)}}{1 - \rho_1 \eta_2 e^{i(\phi_2 + 2\Phi_1)}} + \rho_0. \quad (5.20)$$

In contrast to the three mirror cavity, the power recycled 3-port-grating cavity has three output ports. In addition to the back reflected field to the input laser source a'_1 , and the light field that is transmitted through the arm cavities end mirror b'_3 , there is the forward reflected port, where the light exits the resonators at the additional port of the grating c'_2 . Analogue to Equations (5.7) and (5.8) the carrier transfer function for the back-reflected (G_b), forward-reflected (G_f) and transmitted port (G_t) are given by:

$$G_b(\Phi_1, \Phi_2) = \frac{a'_1}{a_1} = \left(\rho_1 - \frac{\tau_1^2 \rho_{g2m3} e^{2i\Phi_1}}{1 - \rho_1 \rho_{g2m3} e^{2i\Phi_1}} \right), \quad (5.21)$$

$$G_t(\Phi_1, \Phi_2) = \frac{b'_3}{a_1} = -\frac{\tau_1 \tau_3 \eta_1 e^{i(\phi_1 + \Phi_1 + \Phi_2)}}{(1 - \rho_0 \rho_3 e^{2i\Phi_2})(1 - \rho_1 \rho_{g2m3} e^{2i\Phi_1})}, \quad (5.22)$$

$$G_f(\Phi_1, \Phi_2) = \frac{c'_2}{a_1} = \left[\left(\eta_0 e^{i\Phi_1} + \frac{\rho_3 \eta_1^2 e^{i(2\phi_1 + \Phi_1 + 2\Phi_2)}}{1 - \rho_0 \rho_3 e^{2i\Phi_2}} \right) \cdot \frac{i\tau_1}{1 - \rho_1 \rho_{g2m3} e^{2i\Phi_1}} \right]. \quad (5.23)$$

The light field at the forward reflected port can be written as:

$$\rho_{3\text{PR}}^{\text{forw}} = c'_2 = \eta_1 e^{i\phi_1} \rho_3 \cdot \text{CF}_2(\Phi_1, \Phi_2) e^{2i\Phi_2} + \eta_0 \cdot \text{CF}_1(\Phi_1, \Phi_2) e^{i\Phi_1}. \quad (5.24)$$

In the following investigation the coupling between the two resonators is analyzed for gratings with different balancing of η_0 and η_2 but the same ρ_0 . Since the balancing of η_2 and η_0 affects the light field that is back-reflected from the grating cavity as shown in Chapter 2, the choice of η_2 has a severe impact on the coupling of the two resonators.

Case 1: $\eta_2 = \eta_{2\min}$

For the comparison of the different power recycled 3-port-grating cavities with the three mirror cavity, the reflectivities of m_1 ($\rho_1^2 = 0.7$) and m_3 ($\rho_3^2 = 0.9$) remain unchanged. The reflectivity of the grating for normal incidence was chosen to match the reflectivity of m_2 in the previous three mirror cavity investigation ($\rho_0^2 = 0.8$). Therefore it is ensured that the bandwidth of the isolated arm cavities is the same for both studies. Note that due to the additional port of the grating only half of the light is coupled into the arm cavity ($\eta_1^2 = 0.1$) compared to the three mirror cavity ($\tau_2^2 = 0.2$). As a consequence the internal power inside the non-recycled 3-port-grating cavity will be lower by a factor of two. Figure 5.5 shows the resonance pattern of a power recycled 3-port-grating cavity with $\eta_2 = \eta_{2\min} = (1 - \rho_0)/2 = 0.0527$. The three dimensional plot shows the transmitted power (color coded) as a function of the tunings Φ_1 and Φ_2 . The resonance pattern is periodic in $\Phi_1 \bmod \pi$ and in $\Phi_2 \bmod \pi$. In contrast to the three mirror cavity a significant power enhancement is only present around the global maximum at $\Phi_1 = 90^\circ$ and $\Phi_2 = 0^\circ$. Although this operating point marks the global maximum only about 70% of the light is transmitted through the resonator. This can be understood when looking at the compound mirror reflectivities shown in Figure 5.6.

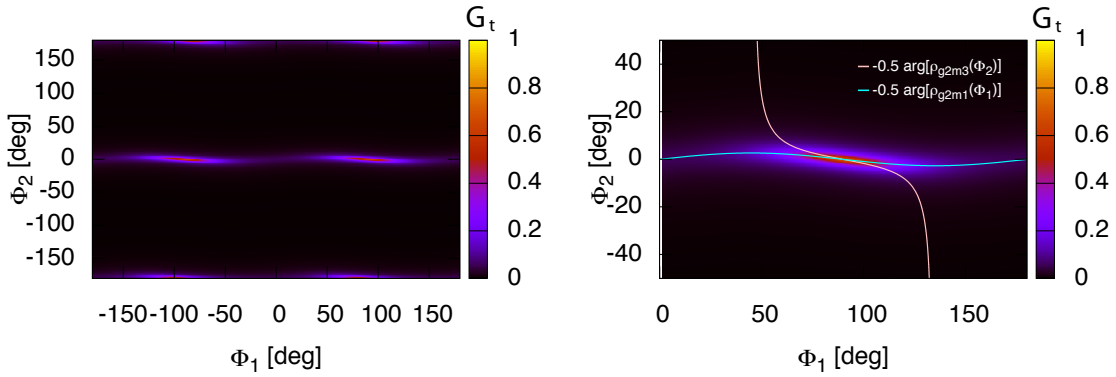


Figure 5.5 — Power transfer function to the transmission port of a power recycled 3-port cavity with $\rho_1^2 = 0.7$, $\rho_0^2 = 0.8$, $\eta_2 = \eta_{2\min}$ and $\rho_3^2 = 0.9$ as a function of the tunings Φ_1 and Φ_2 . In contrast to the three mirror cavity a significant power enhancement is only present around the global maximum at $\Phi_1 = 90^\circ$ and $\Phi_2 = 0^\circ$, and not along the whole resonance branch.

For a grating with $\eta_2 = \eta_{2\min}$ the reflectivity of the second cavity behaves diametrical opposed to the three-mirror case. For a detuning of $\Phi_2 = 0^\circ$ the arm cavity is resonant, leading to a high power gain inside the second cavity while at the same time the compound mirror power reflectivity $|\rho_{g2m3}|^2$ is at a maximum. This maximum is however

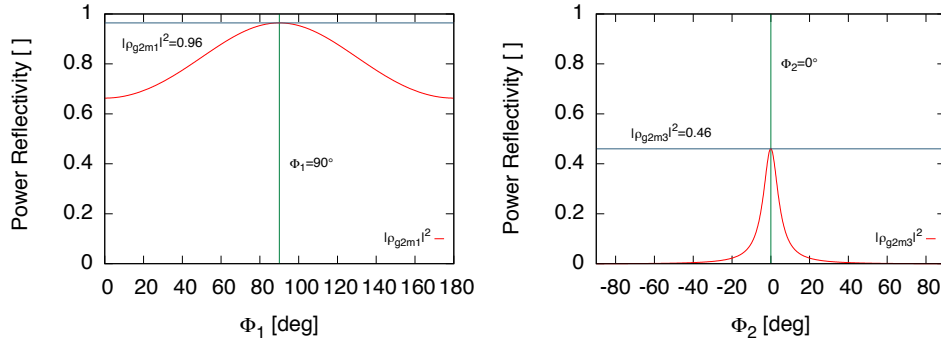


Figure 5.6 — Compound mirror power reflectivities $|\rho_{g2m1}|^2$ and $|\rho_{g2m3}|^2$ for the $\eta_{2\min}$ -configuration as a function of Φ_1 and Φ_2 respectively. The resonance of the second cavity $\Phi_2 = 0^\circ$ corresponds to a maximum of the compound mirror reflectivity of the resonator.

below ρ_1^2 , because impedance matching is not possible in this configuration. The compound mirror power reflectivity of the second cavity rapidly decreases for off resonant tunings, leading to a power recycling cavity with almost no power enhancement and thereby explaining the presence of the strictly confined resonance island around the global maximum. Note that the operating point leading to the largest power in the arm cavity ($\Phi_1 = 90^\circ$ and $\Phi_2 = 0^\circ$) is independent of the chosen reflectivities for gratings at $\eta_{2\min}$.

With respect to a possible application in a gravitational wave detector, for a choice of $\rho_0^2 = 0.95$ and $\rho_3^2 = 0.99995$ the largest power enhancement is achieved when the reflectivity of the recycling mirror meets $\rho_1^2 = |\rho_{g2m3}(\Phi_2 = 0^\circ)|^2 = 0.998$. For this choice of parameters compared to the non-recycled cavity (for 1 W input power, internal power ≈ 39 W) the power in the arm cavity is enhanced by a factor of ≈ 512 to an internal power of ≈ 20 kW. The power-recycling gain is a factor of two larger than for the three mirror cavity. Therefore it is possible to regain the factor of two that was lost due to the coupling and the same power level inside the arm cavity can be reached as in the three mirror cavity case. However in a Michelson interferometer set-up the power at the beam splitter will be larger by a factor of two, hence the use of an all-reflective beam splitter as realized in [39] is recommended.

Case 2: $\eta_2 = \eta_{2\max}$

Figure 5.7 shows the resonance pattern of a power recycled 3-port-grating cavity with $\eta_2 = \eta_{2\max} = (1 + \rho_0)/2 = 0.9472$. The three dimensional plot shows the transmitted power (color coded) as a function of the tunings Φ_1 and Φ_2 . The resonance pattern is periodic in $\Phi_1 \bmod \pi$ and in $\Phi_2 \bmod \pi$ and point symmetric about the origin. The shape of the resonance pattern is similar to the one of the three mirror cavity. The local maxima are aligned along the resonance branch given by the detuning needed to compensate the phase shift at reflection at each resonator. The global maximum of the transmitted power is located at $\Phi_1 = 78^\circ$, $\Phi_2 = -6.5^\circ$ and $\Phi_1 = 102^\circ$, $\Phi_2 = 6.5^\circ$, respectively. but

only about half of the light is transmitted through the resonator. In addition to the transmission port (b'_3) and the reflection port (a'_1) there is also the forward reflected port (c'_2), where light can be coupled out of the resonator. The light power $|a'_1|^2$ and $|c'_2|^2$ are shown in Figure 5.8 as a function of Φ_1 and Φ_2 . Although almost no light is back reflected at the operating point that corresponds to the global maximum in transmission, a significant portion of light is coupled out via the additional port. Hence the power enhancement in the arm cavity is limited by this additional loss channel.

For a grating with $\eta_2 = \eta_{2\max}$, the compound mirror reflectivities show a similar behavior like a three mirror cavity (see Figure 5.9). The reflectivity of the grating cavity is maximal on anti-resonance ($\Phi_2 = 90^\circ$) and minimal for $\Phi_2 = 0^\circ$. The global maximum of the transmitted power does not correspond to the tuning where $|\rho_{g2m3}|^2$ matches ρ_1^2 . For all tunings the compound mirror power reflectivity of the first cavity is lower than ρ_3^2 , so that the power recycled cavity will not be impedance matched regardless of the choice of ρ_1 as long as $\rho_0 < \rho_3$. On the other hand, $|\rho_{g2m3}|^2$ can be close to unity for a large detuning of the arm cavity, which in conjunction with a proper choice of ρ_1 will lead to a very large power enhancement inside the recycling cavity. Since a high carrier power is preferred in the arm cavity rather than in the recycling cavity, the $\eta_{2\max}$ -configuration is not well suited for power recycling.

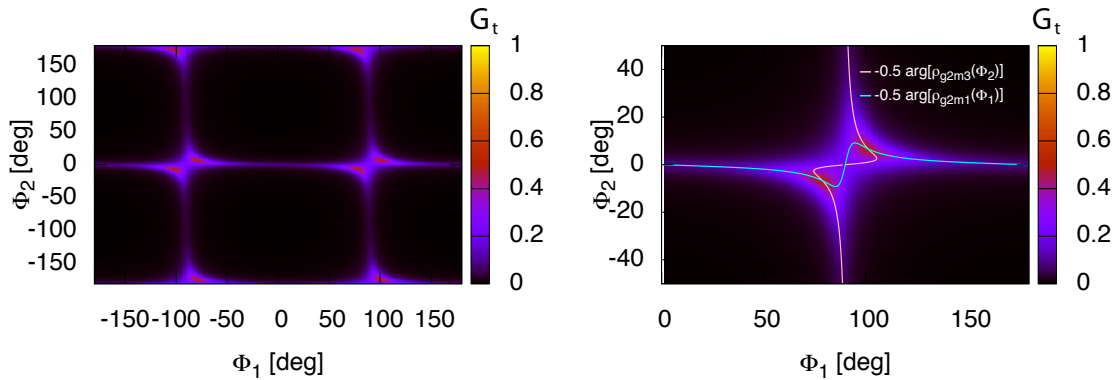


Figure 5.7 — Power transfer function to the transmission port of a power recycled 3-port cavity with $\rho_1^2 = 0.7, \rho_0^2 = 0.8, \eta_2 = \eta_{2\max}$ and $\rho_3^2 = 0.9$ as a function of the tunings Φ_1 and Φ_2 . The local maxima of the transmitted power are aligned along the resonance branches. The global maximum is located at $\Phi_1 = 78^\circ, \Phi_2 = -6.5^\circ$ and $\Phi_1 = 102^\circ, \Phi_2 = 6.5^\circ$. At this operating point only about half of the light is transmitted.

Case 3: $\eta_2 = \eta_0$

Figure 5.10 shows the resonance pattern of a power recycled 3-port-grating cavity with $\eta_2^2 = \eta_0^2 = 0.45$. The pattern does not show the symmetry that is present in the $\eta_{2\max}$ -configuration. Again this can be understood when looking at the compound mirror power reflectivities shown in Figure 5.11. In contrast to the previously investigated configurations, $|\rho_{g2m3}|^2$ is not symmetric around the resonance of the arm cavity ($\Phi_2 =$

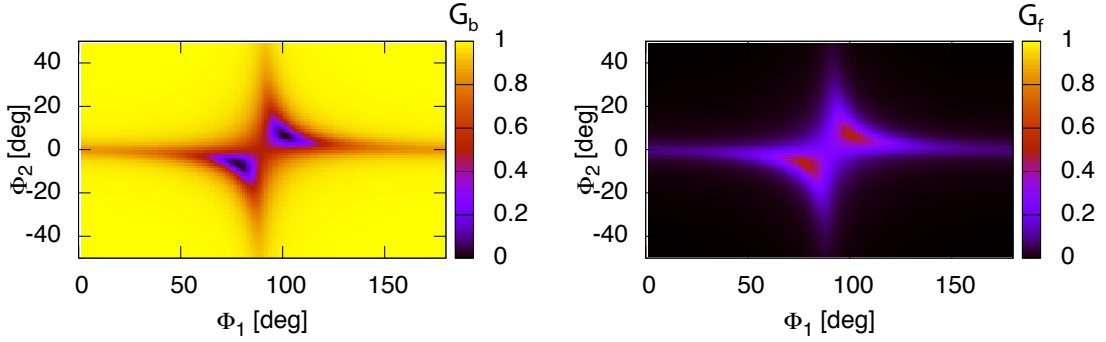


Figure 5.8 — Power transfer function to forward and back reflected port of a power recycled 3-port cavity with $\rho_1^2 = 0.7, \rho_0^2 = 0.8, \eta_2 = \eta_{2\max}$ as a function of the tunings Φ_1 and Φ_2 . At the operating point that corresponds to the global maximum in transmission, a significant amount of light is coupled out via the forward reflection port, thereby limiting the stored power in the arm cavity.

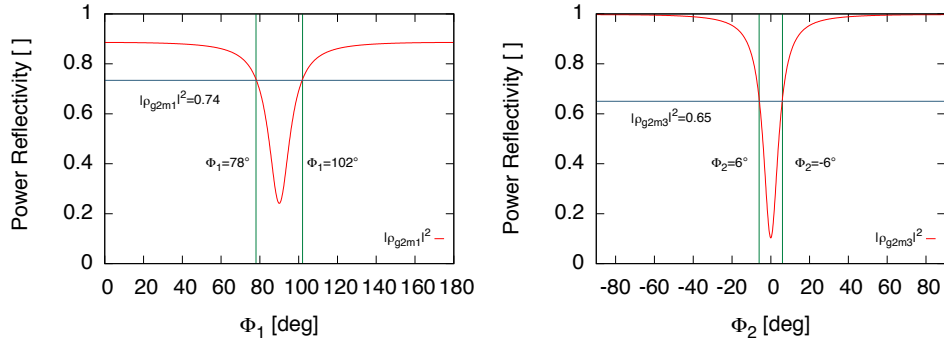


Figure 5.9 — Compound mirror power reflectivities $|\rho_{g2m1}|^2$ and $|\rho_{g2m3}|^2$ for the $\eta_{2\max}$ -configuration as a function of Φ_1 and Φ_2 respectively.

0°). As a consequence no resonance doublets occur as seen in the $\eta_{2\max}$ -configuration, because only at a negative detuning the compound mirror power reflectivity is in a regime that allows for significant power enhancement in the recycling cavity.

For a cavity with the parameters $\rho_0^2 = 0.95, \eta_2^2 = \eta_0^2 = 0.475$ and $\rho_3^2 = 0.99995$ the reflectivity of the recycling mirror has to be chosen to $\rho_1^2 = 0.999$ to obtain the configuration with the highest power gain for a given bandwidth of the arm cavity. At the operating point $\Phi_1 = 112^\circ, \Phi_2 = -0.7^\circ$ the internal power of the arm cavity is enhanced by a factor of ≈ 512 , leading to the same power level as in the three mirror cavity with the same bandwidth (20000 W internal power for 1 W input power).

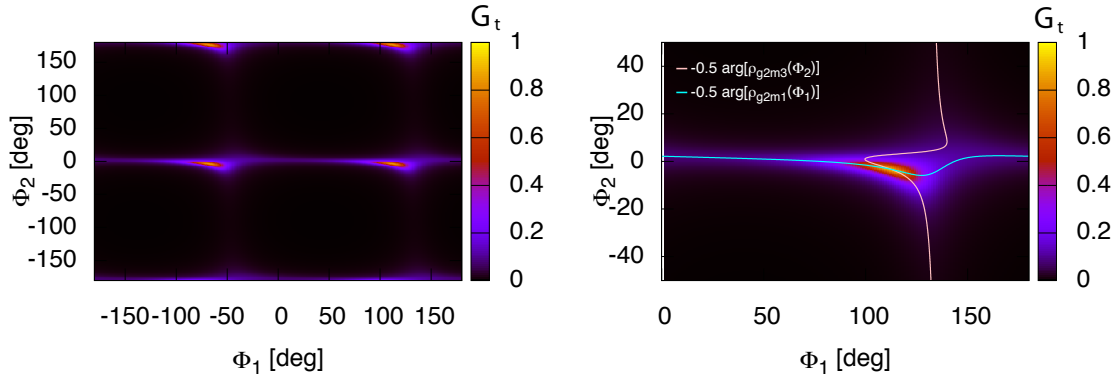


Figure 5.10 — Power transfer function to the transmission port of a power recycled 3-port cavity with $\rho_1^2 = 0.7, \rho_0^2 = 0.8, \eta_2^2 = \eta_0^2 = 0.45$ and $\rho_3^2 = 0.9$ as a function of the tunings Φ_1 and Φ_2 . There are no resonance doublets present. The operating point $\Phi_1 = 113^\circ, \Phi_2 = -3.3^\circ$ corresponds to the global maximum of the internal power in the arm cavity.

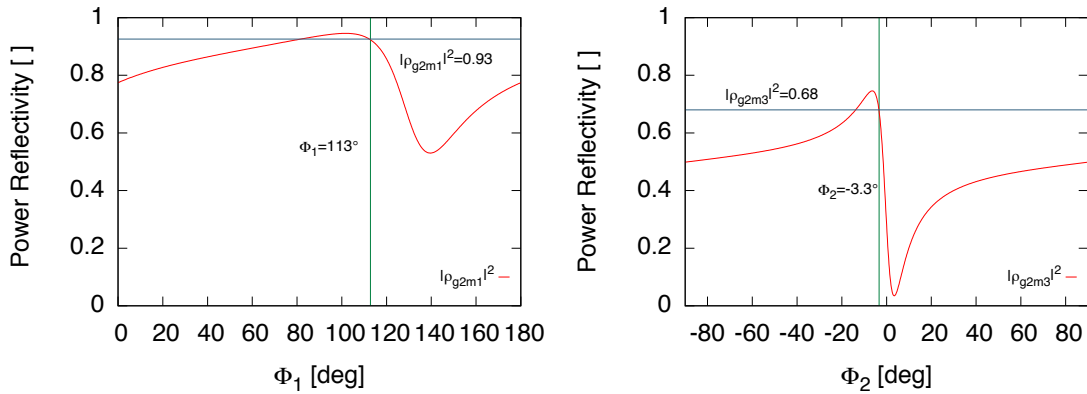


Figure 5.11 — Compound mirror power reflectivities $|\rho_{g2m1}|^2$ and $|\rho_{g2m3}|^2$ for $\eta_2^2 = \eta_0^2$ as a function of Φ_1 and Φ_2 respectively. Note that $|\rho_{g2m3}|^2$ is not symmetric around $\Phi_1 = 0^\circ$.

5.3 Experimental realization of a power recycled 3-port-grating coupled cavity

5.3.1 Geometrical considerations

In contrast to conventional mirrors, diffraction at a grating into an order > 0 changes the geometrical parameters of the beam if angle of incidence and diffraction angle are different. This leads to restrictions to the geometrical set-up of a power recycled 3-port-grating cavity, that are discussed in the following.

The arm cavity is a half-symmetric resonator consisting of a spherical end mirror (m_3) and a flat grating (g_2). The two components form a stable resonator if the stability criterion [64] is fulfilled:

$$1 \geq g_{g_2} g_{m_3} \geq -1 \quad (5.25)$$

$$\text{with } g_{g_2} = 1 - \frac{L_2}{R_{c,g_2}} = 1, \quad g_{m_3} = 1 - \frac{L_2}{R_{c,m_3}}, \quad (5.26)$$

where R_{c,m_3} denotes the radius of curvature of the end mirror. In a half-symmetric resonator the beam waist of the round eigenmode of the cavity is positioned at the flat component with a waist size:

$$w_0^2 = \frac{L_2 \lambda}{\pi} \sqrt{\frac{g_{m_3}}{1 - g_{m_3}}}. \quad (5.27)$$

If a round light beam is incident on a grating in 2nd-order Littrow configuration, the beam that is diffracted into the 1st diffraction order at an emergent angle of 0° will be elliptical. The angle of incidence (θ_{in}) does not match the emergent angle (θ_{out}) which results in a distortion of the beam in one dimension. The relation between the waist size of input and output beam in the affected dimension is given by:

$$w_{\text{out}} = \frac{\cos(\theta_{\text{out}})}{\cos(\theta_{\text{in}})} w_{\text{in}}. \quad (5.28)$$

Therefore the ratio between x- and y-direction waist size is completely determined by the 2nd order Littrow angle (for the used grating: 47.2°). In order to match the mode of the incoming beam to the round eigenmode of the arm cavity, the incident beam needs to have a degree of ellipticity that is exactly compensated by the beam deformation that is applied to the beam when diffracted into the 1st order. As a consequence the radii of curvature of the power recycling mirror need to be different in x- and y- direction, because the eigenmode of the power recycling cavity is elliptical. For a given eigenmode of the arm cavity and length of the recycling cavity L_1 , the desired radii of curvature of the recycling mirror are given by:

$$R_{c,y} = L_1 + \frac{\pi^2 w_{0,y}^4}{\lambda^2 L_1}, \quad (5.29)$$

$$R_{c,x} = L_1 + \frac{\pi^2 w_{0,x}^4}{\lambda^2 L_1} = L_1 + \frac{\pi^2 w_{0,y}^4}{\lambda^2 L_1 (\cos \theta_{\text{in}})^4}. \quad (5.30)$$

The configuration that was chosen for the experiment is shown in Figure 5.12.

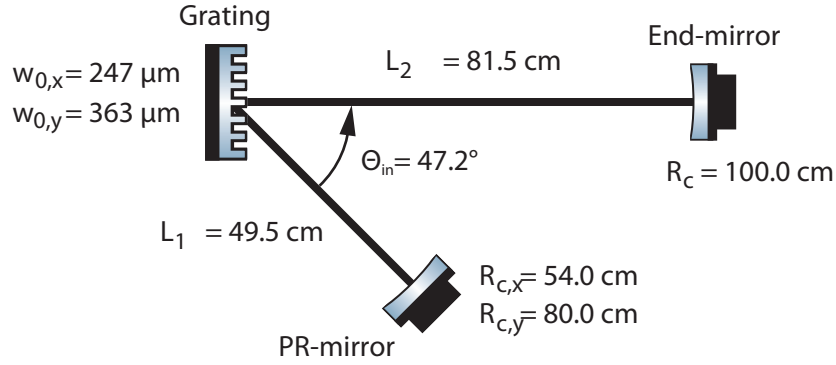


Figure 5.12 — Geometrical configuration of the experiment. The 2nd order Littrow angle determines the ratio of x- and y- direction waist size at the grating. The length of the arm and the radius of curvature of the end mirror defines the waist size at the grating. Together with the length of the power recycling cavity these parameters determine the radii of curvature of the power recycling mirror.

5.3.2 Experimental set-up

The experimental set-up is shown in Figure 5.13. The laser light from a 1.2 W Nd:YAG source is spatially and temporally filtered by a mode-cleaner as described in [54]. An electro-optical modulator (EOM) is used to imprint 15 MHz phase-modulation sidebands for locking both cavities using the Pound-Drever-Hall method (PDH) (see Chapter 3). For each dimension two cylindrical lenses are employed to generate the elliptical beam profile that is needed in order to mode-match the incoming beam to the eigenmode of the recycling cavity. An additional spherical lens was installed to compensate the beam distortion caused by the substrate of the power recycling mirror. A dielectric multilayer system was applied to the power recycling mirror providing a reflectivity of $\rho_1^2 = 0.96$. The high reflecting end mirror had a transmissivity of $\tau_3^2 = 7$ ppm. The power recycling mirror as well as the end mirror was mounted onto a piezo-electrical transducer (PZT) in order to change the microscopic mirror position and thereby the tuning of both resonators. In contrast to the theoretical description the grating is not loss-less. The total optical loss of the grating could be determined to be $A = 0.00268 \pm 0.00606$. One loss channel that could be measured separately is the residual transmission, which amounts to $\tau_0^2 = 122.9 \pm 9.2$ ppm. Since the transmission at this additional port is larger than the transmission of the end mirror this port was used to detect the transmitted internal field of the arm cavity. The diffraction efficiencies of the grating were found to be $\eta_1^2 = 0.0591 \pm 0.003$ and $\eta_2^2 = 0.00096 \pm 0.00005$. The 0th order diffraction efficiency for normal incidence was determined by a finesse measurement as described in [43] to be $\rho_0^2 = 0.87904 \pm 0.00273$. When the power recycling mirror is tuned far from the resonance condition of the recycling cavity, the recycling mirror acts just like an attenuator in front of the arm cavity. In this configuration the arm cavity properties can be determined without being influenced by the recycling cavity. The finesse of the arm cavity of $\mathcal{F}_{\text{arm}} = 49.3 \pm 1.6$ results from the measured line-width of $\text{FWHM}_{\text{arm}} = 3.73 \pm 0.12$ MHz.

The arm cavity can be locked to the resonant state using the standard PDH method with an error signal detected at the forward reflected port c'_2 . While the arm cavity is locked the power recycling cavity length is scanned in order to determine the finesse of the recycling cavity. The measured linewidths of the recycling cavity of $\text{FWHM}_{\text{PR}} = 5.79 \pm 1.24$ MHz yields a finesse of $\mathcal{F}_{\text{PR}} = 52.3 \pm 14.3$.

With the arm cavity stabilized on resonance also the recycling cavity can be locked using an error signal detected at the reflection port a'_1 . In this hierarchical locking a robust stabilization of both cavities could be achieved. When the recycling set-up is held on resonance the internal power inside the arm can be determined by extrapolating from the power transmitted at the grating. Compared to the non recycled arm cavity the power inside the arm was increased by a factor of ≈ 15.8 due to power recycling. This value is smaller than the theoretical predicted value of ≈ 24 . The deviation mainly originates from imperfect mode matching. The total loss of the grating was determined by a finesse measurement. With this method only the loss of the grating under normal incidence is accessible. Since the power recycling cavity uses the reflecting property of the grating from a different angle, there might be previously unaccounted losses that are also responsible for the deviation in the power recycling factor. However it could be shown that the technique of power recycling can also be used with 3-port-grating cavities and that the internal power in the arm can be significantly increased.

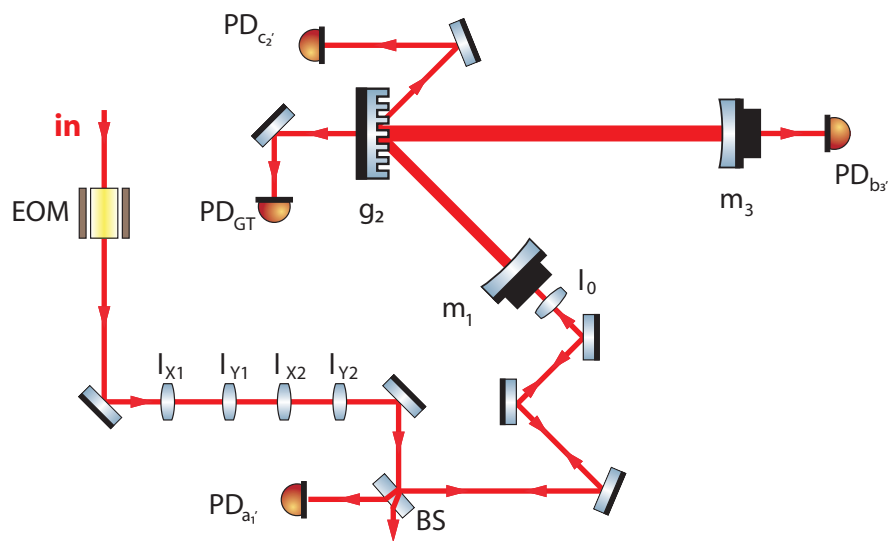


Figure 5.13 — Experimental set-up of a 3-port-grating cavity with power recycling. Phase modulation sidebands at 15 MHz are imprinted on the light to generate an error signal for length control of the system. Two cylindrical lenses for each dimension are needed to provide mode-matching to the eigenmode of the cavity. An additional spherical lens is used to compensate the beam distortion due to the substrate of the recycling mirror.

5.3.3 Comparison with simulations

Given that the theoretical description of the 3-port-grating always assumes a loss-less optical device, there will be always deviations between the simulation and the actual experimental data. Table 5.1 compares the measured values with the parameters chosen for the theoretical model. For this set of fixed parameters, the state of the cavity depends on the tuning of both the arm cavity (Φ_2) and the tuning of the recycling cavity (Φ_1). In the simulation the dependence of the cavity state of these two degrees of freedom can be visualized by a three dimensional plot as introduced in Section 5.2 where the third dimension is given by the power at the according port. In the experiment the dependence can be visualized by changing one of the two tunings with a low frequency (< 1 Hz), while the other degree of freedom is varied at a significantly larger frequency (≈ 1 kHz). Since the data that can be recorded from a photodetector is a two-dimensional data set, containing the voltage at a given time, the resulting picture is comparable to a two dimensional "lateral view" of a three dimensional plot. Figures 5.14-5.19 compare the modeled and measured power as a function of the two tunings Φ_1 and Φ_2 . It can be seen that the model is qualitatively in good agreement with the experimental results. Therefore the behavior of 3-port-grating cavities with power recycling is well understood.

Parameter	Measured Value	Simulation Parameter
η_0^2	0.92368 ± 0.0450	0.9399
η_1^2	0.05914 ± 0.00303	0.05914
η_2^2	0.00096 ± 0.00005	0.00096
ρ_0^2	0.87904 ± 0.00273	0.88172
Total loss	0.00268 ± 0.00606	0
FSR _{arm} (w/o PR)	184.01 ± 0.23 MHz	184.01 MHz
FWHM _{PR} (w/o PR)	3.73 ± 0.12 MHz	3.76 MHz
Finesse	49.3 ± 1.6	48.98
FSR _{PR} ($\Phi_{\text{arm}} = 0$)	302.82 ± 0.56 MHz	302.82 MHz
FWHM _{PR} ($\Phi_{\text{arm}} = 0$)	5.79 ± 1.24 MHz 5.05 MHz	
Finesse	52.3 ± 14.3	60.013
Power in arm/Input Power	15.8	24

Table 5.1 — Comparison of measured values and parameters chosen for the simulations.

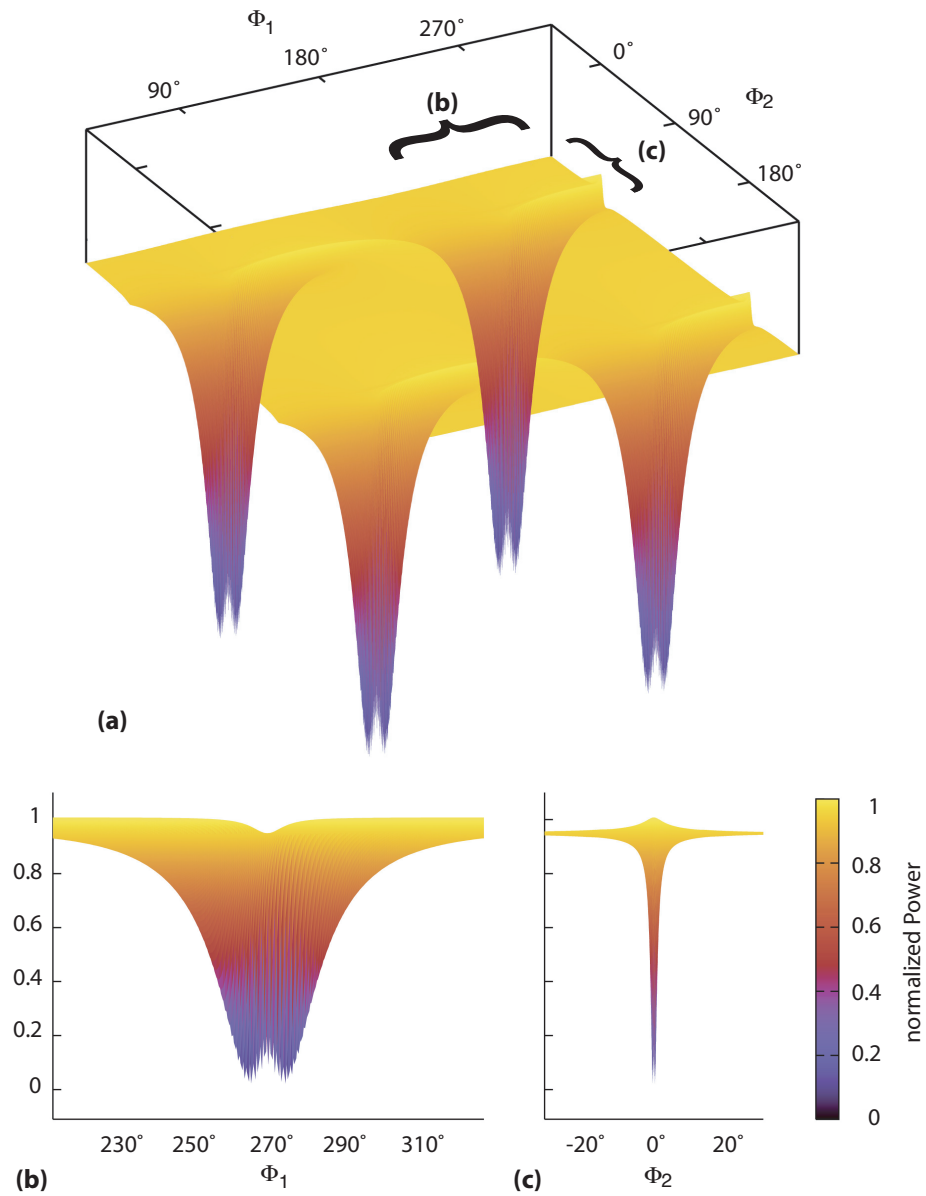


Figure 5.14 — Simulation of the power at the back reflected port $|a'_1|^2$ as a function of the tunings Φ_1 and Φ_2 for normalized input power. The figures (b) and (c) show the lateral view of the three dimensional plots.

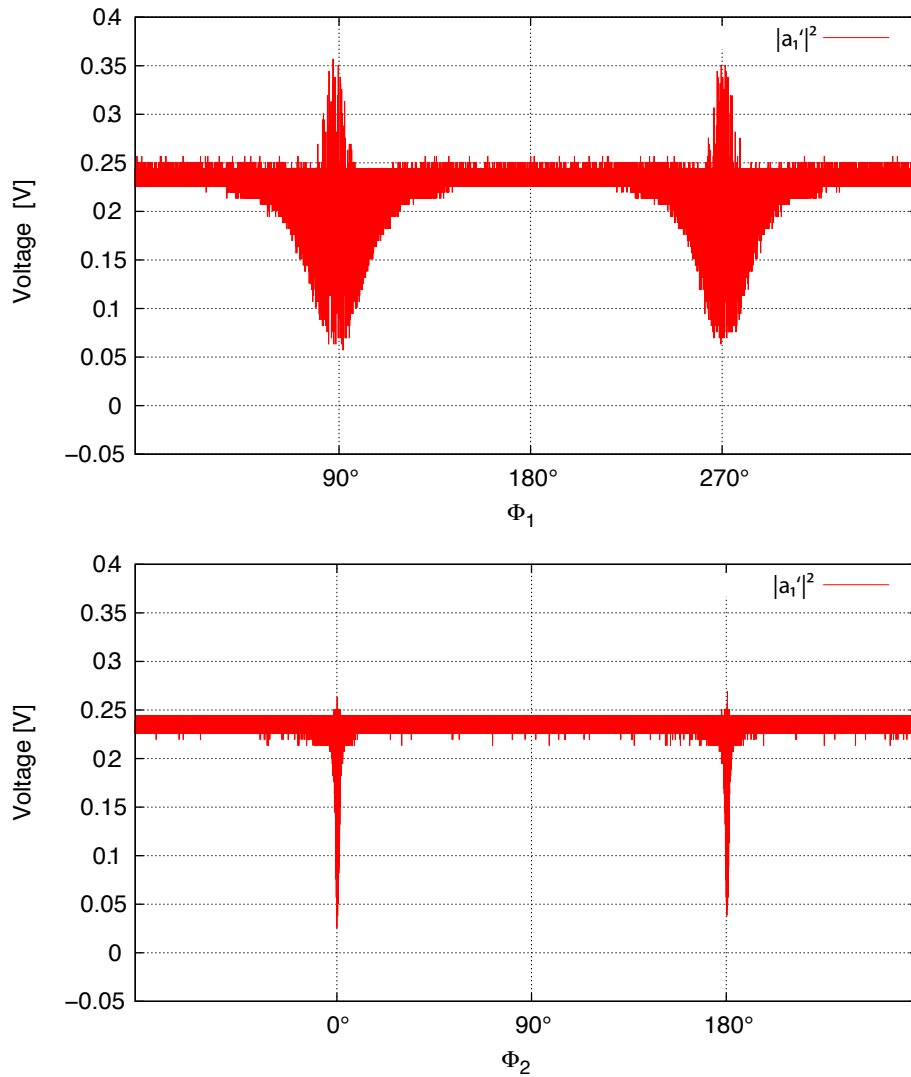


Figure 5.15 — Measured power at the back reflected port $|a_1'|^2$ in dependence of the tunings Φ_1 and Φ_2 . The "lateral view" is generated by choosing considerably different scanning frequencies for the microscopic mirror positions. The overshoot of the signal around the resonance could be traced back to the high scanning frequency used. The effect could be decreased by using a significantly lower scanning frequency [65]

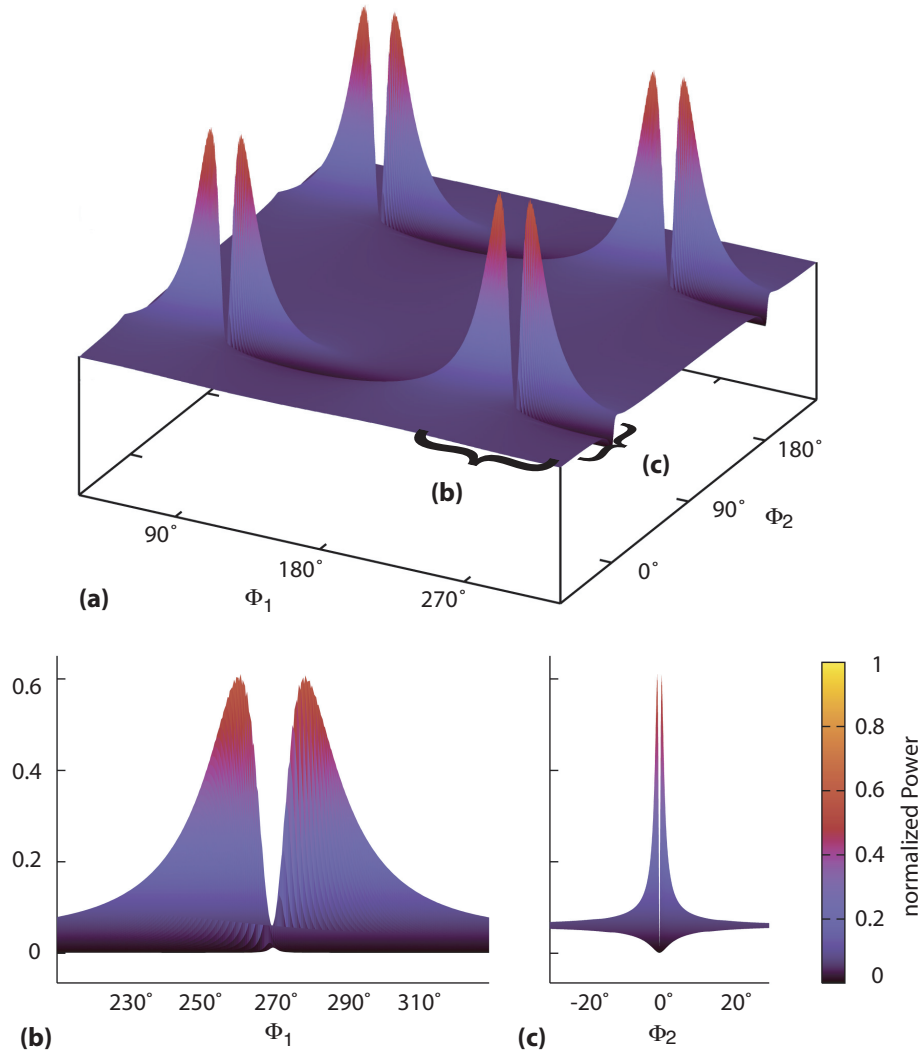


Figure 5.16 — Simulation of the power at the forward reflected port $|c'_2|^2$ as a function of the tunings Φ_1 and Φ_2 for normalized input power. The figures (b) and (c) show the lateral view of the three dimensional plots.

5.3

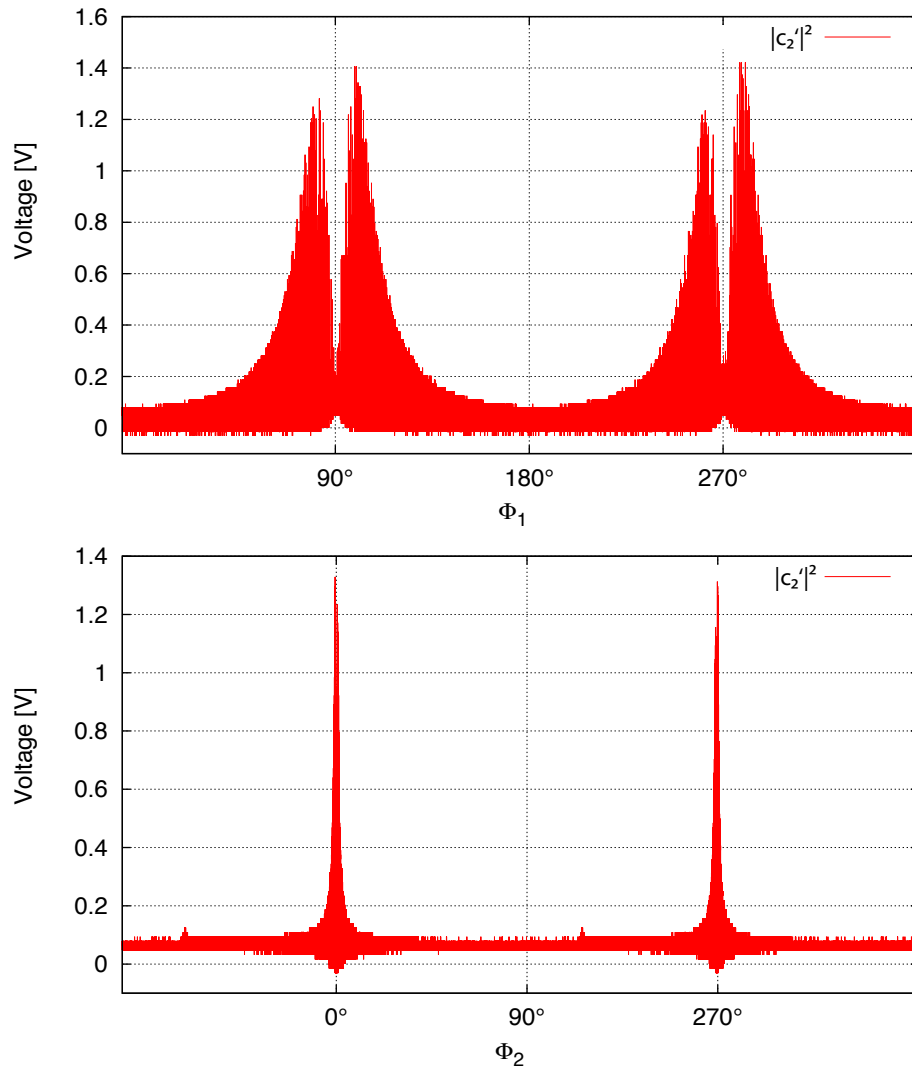


Figure 5.17 — Measured power at the forward reflected port $|c_2'|^2$ in dependence of the tunings Φ_1 and Φ_2 . The "lateral view" is generated by choosing considerably different scanning frequencies for the microscopic mirror positions. The different peak heights in the upper picture could be traced back to non-linearities in the PZT used to scan the cavities [65].

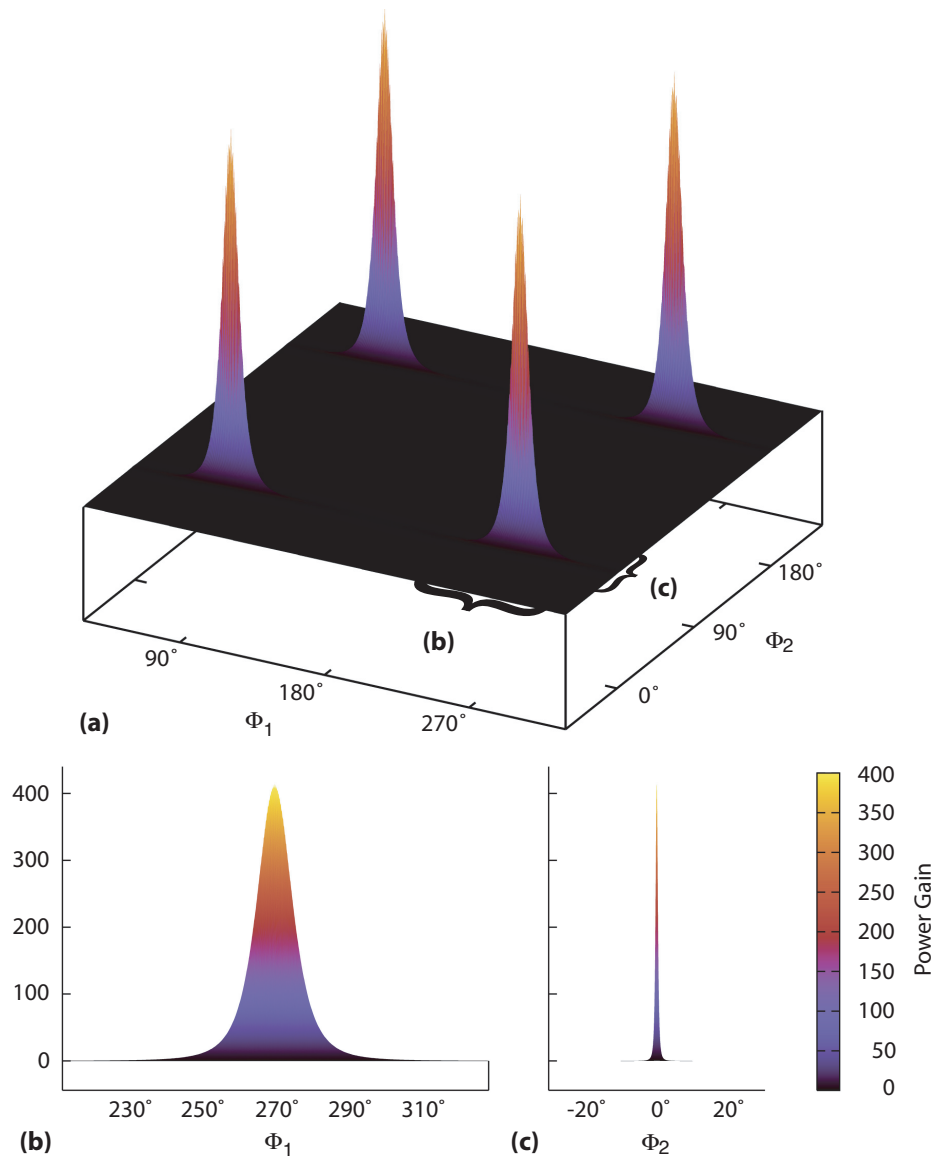


Figure 5.18 — Simulation of the internal power inside the arm cavity $|b_2|^2$ as a function of the tunings Φ_1 and Φ_2 for normalized input power. The figures (b) and (c) show the lateral view of the three dimensional plots.

5.3

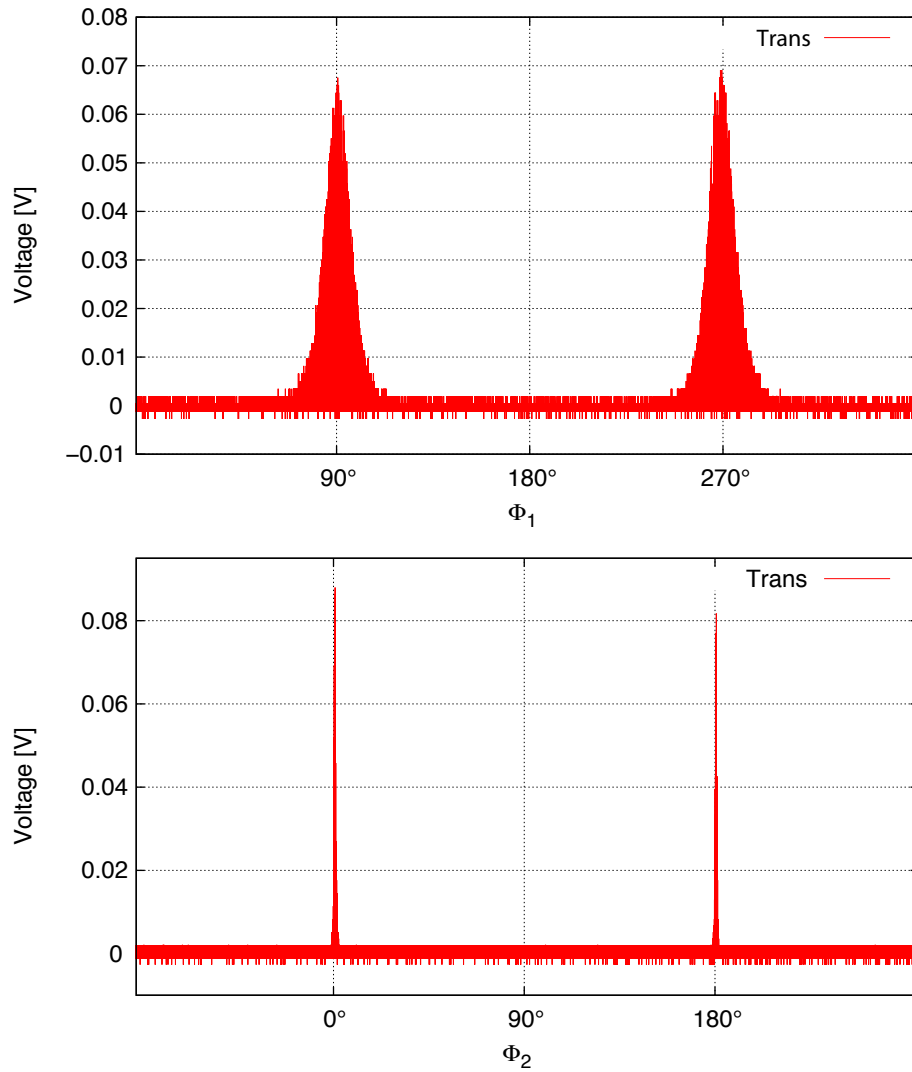


Figure 5.19 — Measured light power that is transmitted at the grating in dependence of the tunings Φ_1 and Φ_2 . This light field is proportional to the internal light power in the arm cavity $|b_2|^2$. The "lateral view" is generated by choosing considerably different scanning frequencies for the microscopic mirror positions.

	Dependence on Φ_1	Dependence on Φ_2
Forward Port	1	0.065
Back Port	-0.064	1

Table 5.2 — Normalized control matrix of the control scheme used in the experiment

5.3.4 Control of Power-Recycled 3-port Cavities

In the previously described experiment only a single modulation frequency of 15 MHz was used to generate the control signals for the arm cavity length as well as the length of the recycling cavity. The PDH error signals can be calculated analogue to Chapter 3 using the transfer functions for carrier and sideband fields. The transfer functions for the carrier fields can be found by rearranging Equations (5.21)-(5.23)

$$G_b(\omega_0) = \frac{a'_1}{a_1} = \left(\rho_1 - \frac{\tau_1^2 \rho_{g2m3} e^{2i\Phi_1}}{1 - \rho_1 \rho_{g2m3} e^{2i\Phi_1}} \right), \quad (5.31)$$

$$G_t(\omega_0) = \frac{b'_3}{a_1} = -\frac{\tau_1 \tau_3 \eta_1 e^{i(\Phi_1 + \Phi_1 + \Phi_2)}}{(1 - \rho_0 \rho_3 e^{2i\Phi_2})(1 - \rho_1 \rho_{g2m3} e^{2i\Phi_1})}, \quad (5.32)$$

$$G_f(\omega_0) = \frac{c'_2}{a_1} = \left[\left(\eta_0 e^{i\Phi_1} + \frac{\rho_3 \eta_1^2 e^{i(2\Phi_1 + \Phi_1 + 2\Phi_2)}}{1 - \rho_0 \rho_3 e^{2i\Phi_2}} \right) \cdot \frac{i\tau_1}{1 - \rho_1 \rho_{g2m3} e^{2i\Phi_1}} \right]. \quad (5.33)$$

In order to obtain the transfer functions for upper and lower sidebands again Φ_1 and Φ_2 need to be replaced by the corresponding value for the sideband frequency according to Equations (3.23) and (3.24):

$$G(\omega_0) \Rightarrow G(\omega_0 - \omega_m) : \Phi_1 \Rightarrow \Phi_{1,l} \text{ and } \Phi_2 \Rightarrow \Phi_{2,l}, \quad (5.34)$$

$$G(\omega_0) \Rightarrow G(\omega_0 + \omega_m) : \Phi_1 \Rightarrow \Phi_{1,u} \text{ and } \Phi_2 \Rightarrow \Phi_{2,u}. \quad (5.35)$$

The error signal H_{ω_m} at each port can be calculated using Equation (3.19). In the experiment a hierarchical control scheme was used, where the arm cavity was locked first using the signal detected at the forward reflected port. Afterwards the lock of the recycling cavity was acquired using the error signal detected at the back reflected port. In contrast to a fully suspended set-up, the mirror position does not fluctuate to a great extend. Therefore the system can be controlled even if the error signals for the different degrees of freedom (Φ_1, Φ_2) are not decoupled.

A measure for the decoupling of error signals is given by the control matrix [66]. This matrix contains the slope of the error signal at the desired operating point at each detection (control) point or output port of the cavity. For the sake of clarity each row is normalized to the element that is chosen to use for the control of one particular degree of freedom. Therefore the error signals are completely decoupled when the control matrix is diagonal. The control matrix for the used configuration is shown in Table 5.2. It can be seen that the signals are not completely decoupled.

For conventional three mirror cavities a lot of different techniques haven been found that aim at decoupling the control signals [67] [68]. The most intuitive technique uses phase modulation sidebands that are anti-resonant in the second cavity

(e.g. $f_{\text{mod}} = \text{FSR}_2/2$), and are therefore directly reflected at the second mirror without interacting with the arm cavity. Hence the error signal generated by this set of sidebands is independent of the tuning of the arm cavity. Due to the different coupling between the two resonators in the grating coupled set-up (for gratings with $\eta_2 \approx \eta_{2\text{min}}$), this technique does not decouple the error signals in the grating set-up. Sidebands that are anti-resonant in the arm cavity are not reflected back from the arm cavity, because the compound mirror reflectivity of the arm cavity as seen from the recycling mirror is maximized at the resonance, and rapidly degrades away from the resonance. Only light fields that are resonant in the arm cavity are reflected back towards the recycling mirror. However one can take advantage of the different signs of the error signals at the different ports. From Table 5.2 it can be deduced, that the off-diagonal elements of the control matrix have opposite sign. If the two signals detected at the forward and back reflected port are added up with the appropriate gain, the error signals for the two degrees of freedom can be easily decoupled, without using additional modulation frequencies. Although the coupling between the resonators is significantly different compared to the cavities consisting of conventional mirrors, it is also possible to decouple the error signals for the different degrees of freedom of 3-port-grating cavity with power recycling.

Resonant sideband extraction

In this chapter the compatibility of 3-port-grating cavities with the technique of resonant sideband extraction is analyzed. Therefore the transfer functions of gravitational wave induced signals to the output ports of 3-port-grating cavities is compared to the signal transfer of conventional mirror cavities. It is shown that placing a signal extraction mirror in the back-reflected port of a 3-port-grating cavity does not lead to a decrease of the storage time of the signal sidebands in the arm cavity. An alternative topology is proposed, where extraction mirrors are placed in the forward as well as the back-reflected port of the 3-port-grating cavity. This more complex topologies enables resonant sideband extraction at 3-port-grating arm cavities.

6.1 Introduction

Apart from increasing the stored carrier light power in the arm cavities of a Michelson interferometer, there is an additional application were coupled cavities are used to increase the sensitivity of laser interferometric gravitational wave detectors. Assuming that both arm cavities are tuned to resonance and the Michelson interferometer is operated at the "dark-fringe", then the carrier light will interfere constructively towards the laser and destructively at the signal output port. A suitably polarized incident gravitational wave will phase modulate the light stored in the arms, and will thus produce upper and lower sidebands with a frequency offset against the carrier that is given by the gravitational wave frequency. These sidebands are generated with opposite phase in both arms. In the "dark-fringe" mode, the interferometer separates the carrier and the gravitational wave induced sidebands. The carrier light is directed towards the laser, where the light is back-reflected by the power-recycling mirror. The sidebands are directed towards the signal extraction mirror that is placed in the output port of the Michelson (see Figure 6.1).

Since cavities act as a low-pass filter, a high finesse arm-cavity will lead to a high power gain inside the arm, while at the same time the bandwidth of the cavity is reduced. The signal extraction mirror forms a coupled cavity with the arm cavities, providing

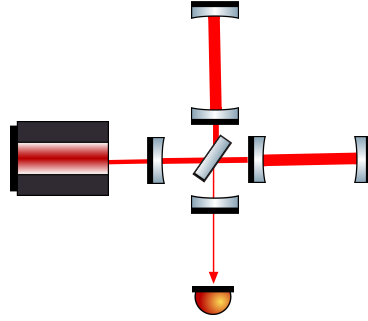


Figure 6.1 — Schematic of the Advanced LIGO topology. The major upgrade of the LIGO detector will use an additional signal extraction mirror at the output port of the detector. This mirror forms a coupled cavity with the arm cavities of the resonator. Since the detector is operated on the dark-fringe, no carrier light will be present at the output port of the cavity, and there will be no interaction of the extraction cavity with the power-recycling cavity.

the possibility to decrease the effective reflectivity of the arm cavities coupling mirror for the sidebands, while maintaining the large power gain of the carrier field [69]. In this chapter, the signal transfer functions of resonators coupled by a 3-port-grating are investigated with respect to an application in a resonant sideband extraction (RSE) configuration, which is considered to be one of the key techniques of today's laser interferometric gravitational wave detectors. In order to compare different topologies one has to investigate the transfer functions to the detection port for gravitational wave induced sidebands with the angular frequency Ω . The normalized transfer function is given by [48]:

$$\mathbf{G}(\Omega) = G(\Omega) + G^*(-\Omega), \quad (\text{amplitude quadrature}) \quad (6.1)$$

$$\mathbf{G}(\Omega) = -i(G(\Omega) - G^*(-\Omega)). \quad (\text{phase quadrature}) \quad (6.2)$$

The transfer functions for upper and lower sidebands are composed by three terms

$$G(\Omega) = CF(\Phi) \times G^{\delta\Phi}(\Omega) \times SF(\Phi + \Omega L/c), \quad (6.3)$$

where CF denotes the carrier amplitude derived in Chapter 5, and $G^{\delta\Phi}$ depicts the gravitational wave induced modulation per round trip. In the following investigation of different topologies, the carrier field amplitude and the cavity length are considered to be the same for all configurations. Hence, only the SF term in Equation (6.3), that contains the information about the interaction of the cavity with the cavity, needs to be considered throughout the comparison. Thus the simplified form of the normalized signal transfer function for phase and amplitude quadrature readout are given by:

$$\mathbf{G}(\Omega) = SF(\Omega) + SF(-\Omega)^*, \quad (6.4)$$

$$\mathbf{G}(\Omega) = i(SF(\Omega) - SF(-\Omega)^*). \quad (6.5)$$

6.2 Conventional mirror settings

6.2.1 Signal transfer of a two mirror cavity

The interaction of a gravitational wave of the angular frequency Ω with an arm cavity of a gravitational wave detector can be interpreted as a signal sideband injection inside the arm as depicted in Figure 6.2. Typically the end mirror reflectivity ρ_2^2 is close to unity, thus one is only interested in the signal coupling to the output in reflection of the cavity (a_1'). The signal transfer function of a two mirror cavity can be written as [48]:

$$SF_{2m}(\pm\Omega) = \frac{a_1'(\pm\Omega)}{in_{\text{signal}}} = \frac{i\tau_1 e^{i(\Phi \pm \frac{\Omega L}{c})}}{1 - \rho_1 \rho_2 e^{2i(\Phi \pm \frac{\Omega L}{c})}} \quad (6.6)$$

Figure 6.3 shows the signal transfer function of a 4 km arm cavity with $\rho_1^2 = 0.995$ and $\rho_2^2 = 0.999925$. For $\Phi = 0^\circ$ the transfer function for upper and lower sideband are identical leading to a broadband response. If the cavity is detuned with respect to the carrier resonance to a frequency f_{tar} by $\Phi = \Phi_{\text{tar}} = 2\pi f_{\text{tar}} L/c$ the response is increased at the target frequency at the cost of a decreased response at frequencies away from f_{tar} . In order to reach a high sensitivity the arm cavity of a gravitational wave detector

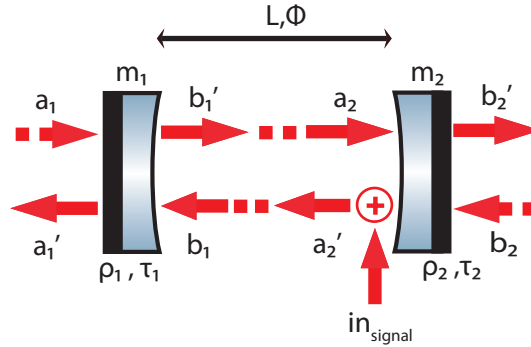


Figure 6.2 — The interaction of a gravitational wave with a two mirror cavity can be interpreted as a signal sideband injection into the arm.

is supposed to be tuned to the carrier resonance, because the signal transfer function given by Equation (6.3) is proportional to the strength of the carrier in the arm. As a consequence detuning the arm cavity is not a favorable option to increase the sensitivity.

6.2.2 Signal transfer of a two resonators coupled by a conventional mirror

Since in a Michelson interferometer operated on the dark fringe carrier and signal sidebands are separated, one can make use of the properties of coupled cavities, to enhance the signal sidebands without affecting the carrier field. The signal extraction mirror in the signal port of the interferometer forms a coupled cavity with the cavities in the arms of the Michelson. Given that there is no interaction of the RSE cavity with the

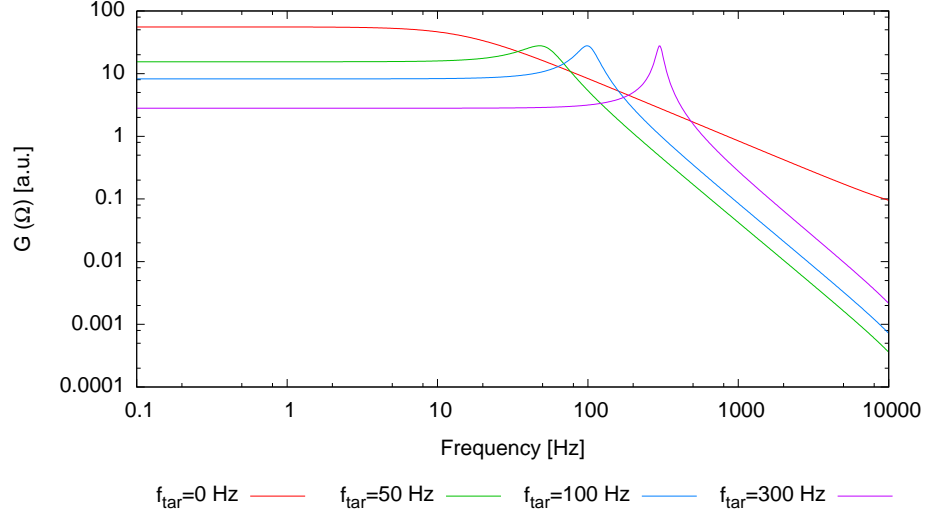


Figure 6.3 — Signal transfer function of a two mirror cavity with $\rho_1^2 = 0.995$ and $\rho_2^2 = 0.999925$. For $\Phi = 0^\circ$ the cavity shows a broadband response. By detuning the cavity the response around the target frequency can be increased at the cost of a lower response at other frequencies.

power recycling cavity, the RSE configuration can be analyzed as a single three mirror coupled cavity as discussed in the previous chapter. Since there is no carrier in the extraction cavity, it can be assumed that the gravitational wave injects phase modulation sidebands only in the arms as depicted in Figure 6.4. The signal transfer function of a three mirror coupled cavity can be derived from Equation (5.8) to:

$$\text{SF}_{3\text{mc}}(\pm\Omega) = \frac{a'_1(\pm\Omega)}{i\text{in}_{\text{signal}}} = -\frac{\tau_1 \tau_2 e^{i(\Phi_1 \pm \frac{\Omega L_1}{c})}}{(1 - \rho_1 \rho_{m2m3} e^{2i(\Phi_1 \pm \frac{\Omega L_1}{c})}) \cdot (1 - \rho_2 \rho_3 e^{2i(\pm \frac{\Omega L_2}{c})})} \quad (6.7)$$

In order to tune the extraction cavity to a frequency f_{tar} , Φ_1 has to be set according to:

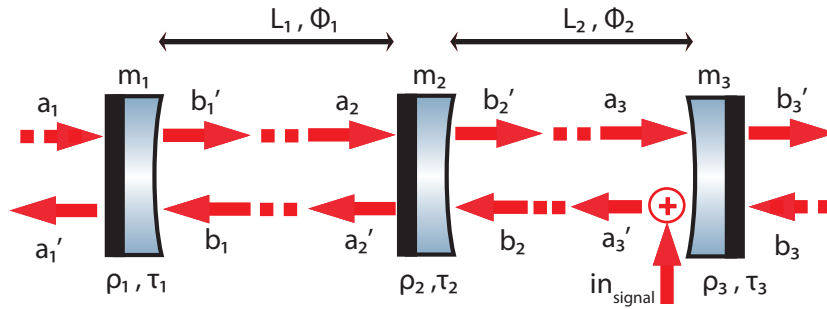


Figure 6.4 — The Michelson interferometer operated at the dark fringe separates carrier and signal field. Since there is now carrier in the extraction cavity, the interaction of a gravitational wave with the RSE configuration can be interpreted as a three mirror coupled cavity with signal sideband injection only into the arm.

$$\Phi_1 = -0.5 \arg(\rho_{m2m3}(2\pi f_{\text{tar}} L_1 / c)), \quad (6.8)$$

with ρ_{m2m3} given by Equation (5.9).

Figure 6.5 shows the signal transfer function of a signal extraction configuration with $\rho_1^2 = 0.93$, $\rho_2^2 = 0.995$ and $\rho_3^2 = 0.999925$ for a tuning to different target frequencies. The chosen parameters are based on the ones currently in discussion for Advanced LIGO [70]. The length of the arm cavity L_2 is chosen to be 4 km, while the extraction cavity has a length of $L_1 = 8.3$ m.

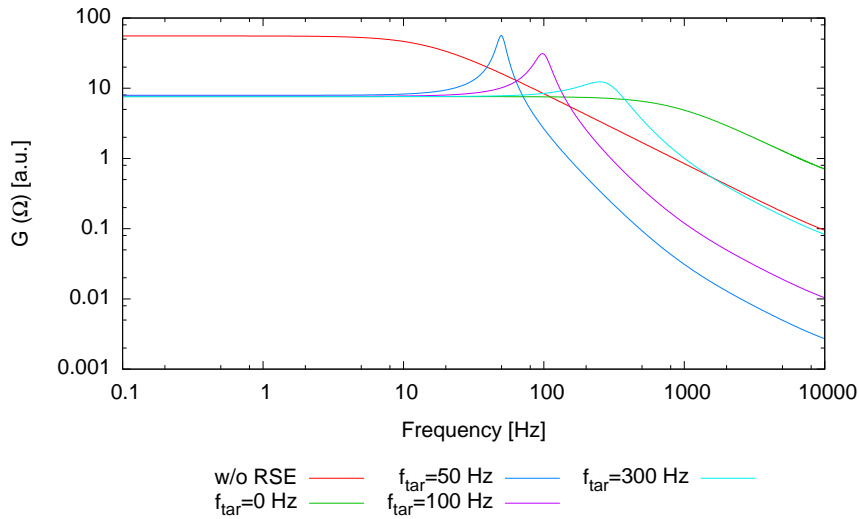


Figure 6.5 — Signal transfer function of a RSE configuration with $\rho_1^2 = 0.93$, $\rho_2^2 = 0.995$ and $\rho_3^2 = 0.999925$ for tuning to different target frequencies. As a comparison the red curve shows the signal transfer function of the arm cavity without RSE.

Compared to the arm cavity without RSE, the bandwidth of the coupled cavity is increased when the RSE-cavity is in place. This can be understood by looking at the compound mirror reflectivities as introduced in Section 5.1. Figure 6.6 shows the compound mirror power reflectivity of the RSE cavity and the arm cavity according to Equation (5.5) and (5.9) as a function of signal frequency. In this example, the RSE cavity was tuned to 300 Hz. The presence of the RSE cavity lowers the reflectivity of the arm cavity coupling mirror for the signal sidebands. As a consequence the effective finesse and thus the storage time of the signal sidebands are decreased. The signal sidebands are extracted from the arm cavity.

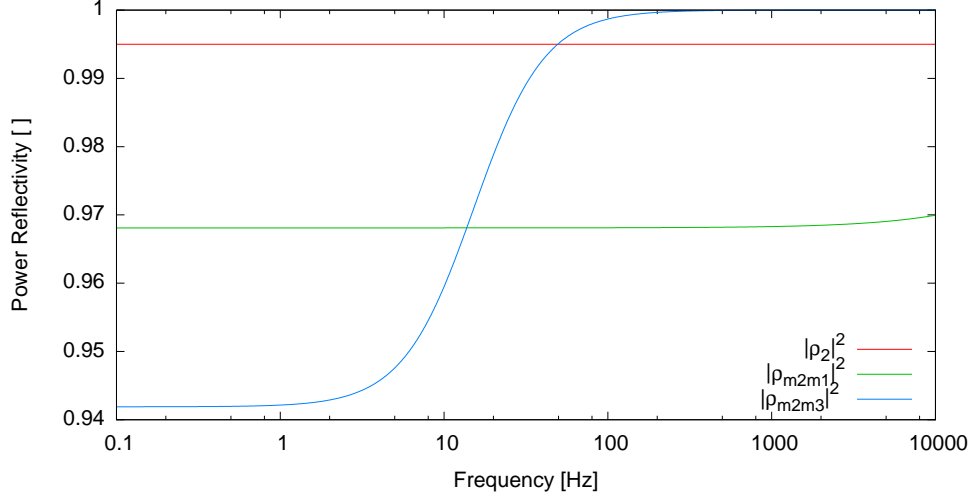


Figure 6.6 — Compound mirror power reflectivity of RSE-configuration tuned to 300 Hz. The RSE-cavity lowers the reflectivity of m_2 for the signal sidebands. The effective finesse and thus the storage time of the signal sidebands are decreased.

6.3 3-port-grating settings

6.3.1 Signal transfer of a 3-port-grating cavity

In the previous chapter it was shown that an $\eta_{2\min}$ -configuration is favorable for an application in a power-recycled Michelson interferometer. Thus the following investigation will be restricted to this configuration only. Although it is not possible to reach the minimum allowed value of η_2 with a real grating, previous experimental results show, that it is possible to fabricate gratings that have very small values of η_2 . Hence it is reasonable to investigate only this case. Analogous to the previous discussion, the interaction of a gravitational wave with a 3-port-grating cavity can be interpreted as a phase modulated sideband injection inside the cavity as depicted in Figure 6.7. For the comparison of a 3-port-grating cavity with a conventional two mirror cavity one needs to take into account that for the same choice of reflectivities (ρ_1 of the two mirror cavity corresponds to ρ_0 of the grating), the internal power inside the grating cavity will be a factor of two lower than in the conventional cavity, because only half of the light is coupled into the grating cavity via the 1st diffraction order ($\eta_1^2 = 0.5 \cdot \tau_1^2$). In order to achieve the same power level as in a conventional two mirror cavity, the laser power input needs to be a factor of two higher. Under this condition the approximation made in Equations (6.4) and (6.5) are still feasible. The signal transfer function of a 3-port-grating cavity is given by:

$$\text{SF}_{3p}(\pm\Omega) = \frac{a'_1(\pm\Omega)}{\text{in}_{\text{signal}}} = \frac{c'_1(\pm\Omega)}{\text{in}_{\text{signal}}} = \frac{\eta_1 e^{i(\phi_1 + \Phi \pm \frac{\Omega L}{c})}}{1 - \rho_0 \rho_2 e^{2i(\Phi \pm \frac{\Omega L}{c})}} \quad (6.9)$$

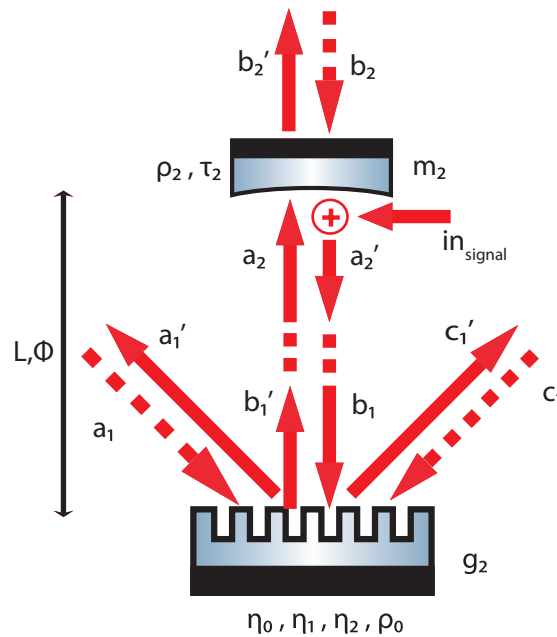


Figure 6.7 — The interaction of a gravitational wave with a 3-port-grating cavity can be interpreted as a signal sideband injection into the arm. The signal is split equally into the forward and back reflected port.

Figure 6.2 shows the signal transfer function of a 4 km 3-port-grating arm cavity with $\rho_0^2 = 0.995$ and $\rho_2^2 = 0.999925$. In contrast to a two mirror cavity, the signal is split equally into the forward and back reflected port of the cavity. Therefore the signal has to be read-out at both ports and added up in order to gain the full information about the signal.

6.3.2 Signal transfer of two cavities coupled by a 3-port-grating

If a mirror is placed in the signal port of a Michelson interferometer with 3-port-grating arm cavities, the setup can be reduced to a three component system analogue to Section 6.2.2. Again the interaction of the gravitational wave can be interpreted as a sideband injection in the arm cavity as depicted in Figure 6.9.

In Chapter 5 it was shown that power-recycling offers the possibility to regain the factor of two in carrier power that is lost due to the coupling into the arm cavity by increasing the power recycling gain. Hence it is possible to reach the same carrier power level as in a conventional arm cavity with the same linewidth and finesse. As a consequence the approximation (6.4) and (6.5) is also valid for the grating coupled arm cavities, and the different topologies can be compared by only considering the SF-terms. The signal transfer function for the signal output port of the Michelson interferometer

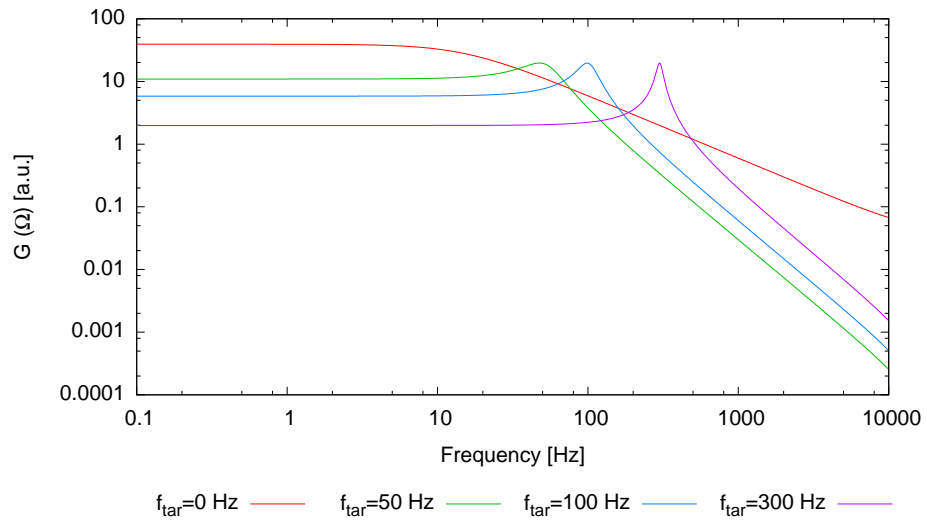


Figure 6.8 — Signal transfer function of a 4 km 3-port-grating arm cavity in $\eta_{2\min}$ -configuration with $\rho_0^2 = 0.995$ and $\rho_2^2 = 0.999925$. The overall signal is the same as in the two mirror cavity case but it is split equally to the forward and back reflected port of the cavity.

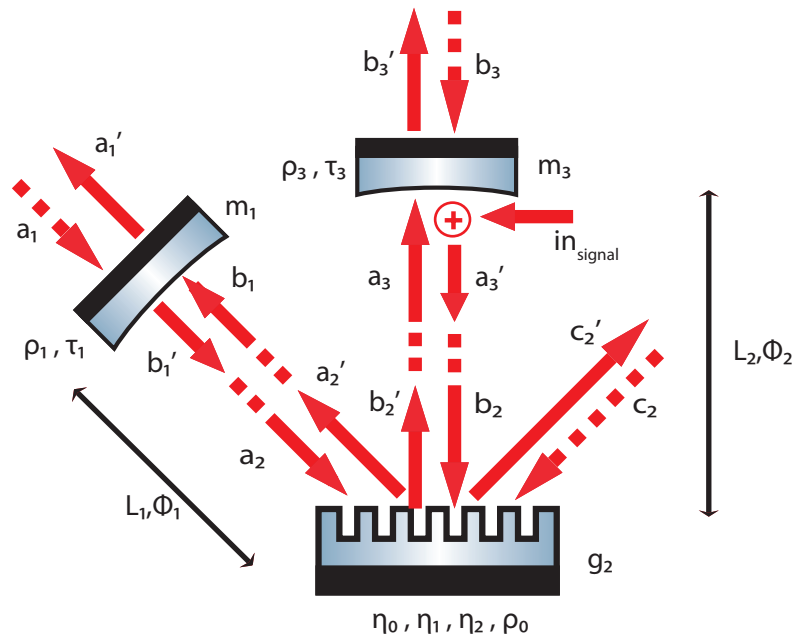


Figure 6.9 — Two resonators coupled by a 3-port-grating. Since there is no carrier light field present at the output port of the Michelson interferometer, the interaction of a gravitational wave with the system can be interpreted as a signal sideband injection solely into the arm.

can be determined from Equation (5.21):

$$\text{SF}_{\text{back}}(\pm\Omega) = \frac{a'_1(\pm\Omega)}{\text{in}_{\text{signal}}} = \frac{i\tau_1\eta_1 e^{i(\phi_1 + \Phi_1 \pm \frac{\Omega L_1}{c} + \Phi_2 \pm \frac{\Omega L_2}{c})}}{(1 - \rho_1\rho_{g2m3} e^{2i(\Phi_1 \pm \frac{\Omega L_1}{c})}) \cdot (1 - \rho_0\rho_3 e^{2i(\Phi_2 \pm \frac{\Omega L_2}{c})})}. \quad (6.10)$$

At the forward reflected port of the cavity, the two signal fields that are coupled out of the first and the second cavity interfere. The internal signal fields inside each of the cavities are given by:

$$b_2(\pm\Omega) = \frac{e^{i(\Phi_2 \pm \frac{\Omega L_2}{c})}}{1 - \rho_3\rho_{g2m1} e^{2i(\Phi_2 \pm \frac{\Omega L_2}{c})}} \cdot \text{in}_{\text{signal}}, \quad (6.11)$$

$$a_2(\pm\Omega) = \frac{\rho_1\eta_1 e^{i(\phi_1 + 2\Phi_1 \pm 2\frac{\Omega L_1}{c})}}{1 - \eta_2\rho_1 e^{i(\phi_2 + 2\Phi_1 \pm 2\frac{\Omega L_1}{c})}} \cdot b_2. \quad (6.12)$$

The field at the forward reflected port c'_2 follows accordingly:

$$c'_2 = \eta_0 \cdot a_2 + \eta_1 e^{i\phi_1} \cdot b_2. \quad (6.13)$$

Thus the signal transfer function of the forward reflected port can be written as:

$$\text{SF}_{\text{forward}}(\pm\Omega) = \frac{c'_2(\pm\Omega)}{\text{in}_{\text{signal}}} = \left(\eta_1 e^{i\phi_1} + \frac{\eta_0\eta_1\rho_1 e^{i(\phi_1 + 2\Phi_1 \pm 2\frac{\Omega L_1}{c})}}{1 - \eta_2\rho_1 e^{2i(\Phi_1 \pm \frac{\Omega L_1}{c})}} \right) \cdot \frac{e^{i(\Phi_2 \pm \frac{\Omega L_2}{c})}}{1 - \rho_0\rho_{g2m1} e^{2i(\Phi_2 \pm \frac{\Omega L_2}{c})}}. \quad (6.14)$$

Figures 6.10 and 6.11 show the signal transfer function of a 4 km long 3-port-grating arm cavity with an additional mirror as shown in Figure 6.9.

The additional mirror in the signal port does not increase the linewidth of the arm cavity for the signal sidebands. For $\Phi_1 > 0$ the transfer function is almost independent of the tuning Φ_1 . The tuning of the extraction cavity analogue to Equation (6.8) does not show an increase in the response around a target frequency. Again the reason for this fundamental difference of conventional mirror setup and 3-port-grating cavity lies in the different coupling between extraction cavity and arm cavity. In contrast to the RSE-configuration discussed in Section 6.2.2, the presence of the additional resonator does not decrease the effective finesse of the arm cavity for the signal sidebands. Instead the effective finesse is even increased, because the compound mirror reflectivity $|\rho_{g2m1}(f_{\text{tar}=100\text{Hz}})|^2 \approx 0.9572$ is even larger than $\rho_0^2 = 0.995$, and the bandwidth at the back reflected port is even smaller than without the additional mirror. For $\Phi_1 = 0^\circ$ the compound mirror reflectivity is at its maximum ($|\rho_{g2m1}(\Phi_1 = 0^\circ)|^2 \approx 0.9572$). At the forward reflection port, only a very small improvement can be seen at frequencies around the arm cavity linewidth (see Figure 6.11). For this reason a configuration with a 3-port-grating arm cavity in $\eta_{2\text{min}}$ -configuration and a mirror in the signal port of the Michelson interferometer is not comparable with the resonant sideband extraction configuration discussed in Section 6.2.2.

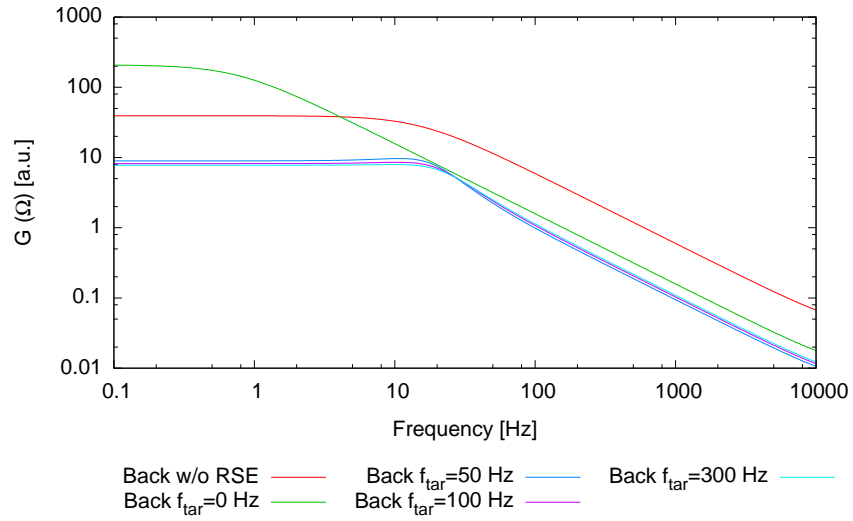


Figure 6.10 — Signal transfer function to the back-reflected port a'_1 of a set-up as shown in Figure 6.9. Cavity parameters: $\rho_1^2 = 0.93$, $\rho_0^2 = 0.995$, $\rho_2^2 = 0.999925$, $L_1 = 8.3$ m and $L_2 = 4000$ m.

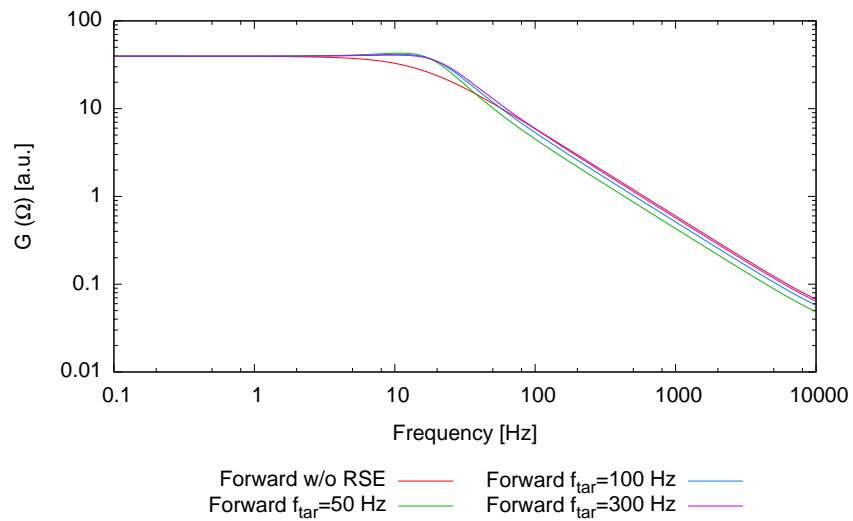


Figure 6.11 — Signal transfer function to the forward-reflected port c'_2 of a set-up as shown in Figure 6.9. Cavity parameters: $\rho_1^2 = 0.93$, $\rho_0^2 = 0.995$, $\rho_2^2 = 0.999925$, $L_1 = 8.3$ m and $L_2 = 4000$ m. The additional mirror does not lead to a significant improvement in sensitivity or bandwidth.

6.4 Resonant sideband extraction for 3-port-grating cavities

Although the standard RSE configuration with one extraction mirror in the signal does not lead to a signal sideband extraction when applied to 3-port-grating arm cavities, it is possible to achieve the same effect with a more complex topology. By placing another mirror in the forward reflection port of the 3-port arm cavity a novel resonator topology is created (see Figure 6.12). This topology is not comparable with the four

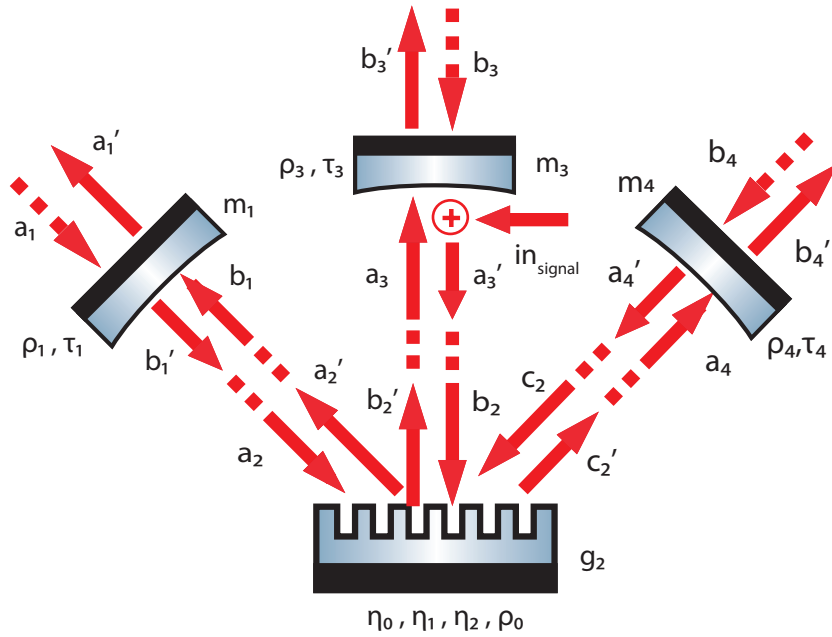


Figure 6.12 — 3-port-grating cavity RSE topology. Extraction mirrors in both output ports of the 3-port-grating arm cavity are needed, to provide a significant sideband extraction effect.

mirror resonator discussed in [48], because the field inside the first resonator composed by m_1 and g_2 and the third resonator between g_2 and m_4 directly couples into the arm cavity (g_2 and m_3) and vice versa. Apart from that also the light fields of the first and third resonator are directly coupled via the grating. In order to derive the signal transfer function of this complex topology it is convenient to make use of the compound mirror approach introduced in 5. The compound mirror reflectivity ρ_{eff} fulfills the condition:

$$b'_2 = \rho_{\text{eff}} \cdot b_2, \quad (6.15)$$

with ρ_{eff} given by:

$$\rho_{\text{eff}} = \frac{(\eta_1^2 \rho_1 e^{2i(\phi_1 + \Phi_1)} - 2\eta_1^2 \rho_1 \eta_2 \rho_4 e^{i(\phi_2 + 2\phi_1 + 2\Phi_1 + 2\Phi_3)} + 2\eta_1^2 \rho_1 \eta_0 \rho_4 e^{2i(\phi_1 + \Phi_1 + \Phi_3)} + \rho_0 - \rho_0 \eta_2 \rho_1 e^{i(\phi_2 + 2\Phi_1)} - \rho_0 \eta_2 \rho_4 e^{i(\phi_2 + 2\Phi_3)} + \rho_0 \eta_2^2 \rho_4 \rho_1 e^{2i(\phi_2 + \Phi_1 + \Phi_3)} - \rho_0 \rho_1 \eta_0^2 \rho_4 e^{2i(\Phi_1 + \Phi_3)} + \eta_1^2 \rho_4 e^{2i(\phi_1 + \Phi_3)})}{\underbrace{1 - \eta_2 \rho_1 e^{i(\phi_2 + 2\Phi_1)} - \eta_2 \rho_4 e^{i(\phi_2 + 2\Phi_3)} + \eta_2^2 \rho_4 \rho_1 e^{2i(\phi_2 + \Phi_3)} - \rho_1 \eta_0^2 \rho_4 e^{2i(\Phi_1 + \Phi_3)}}_{:=\gamma}}.$$

The internal field inside the arm cavity for a signal input into the arm can thus be written as:

$$b_2 = \frac{e^{i\Phi_2}}{1 - \rho_0 \rho_{\text{eff}} e^{2i\Phi_2}} \cdot \text{in}_{\text{signal}}. \quad (6.16)$$

With the knowledge of b_2 one can also derive the internal signal fields inside first and third resonator:

$$b_1 = \gamma \eta_1 e^{i(\phi_1 + \Phi_1)} \cdot (1 - \eta_2 \rho_4 e^{i(\phi_2 + 2\Phi_3)} + \eta_0 \rho_4 e^{2i\Phi_3}) \cdot b_2. \quad (6.17)$$

$$a_4 = \gamma \eta_1 e^{i(\phi_1 + \Phi_3)} \cdot (1 - \eta_2 \rho_1 e^{i(\phi_2 + 2\Phi_1)} + \eta_0 \rho_1 e^{2i\Phi_1}) \cdot b_2. \quad (6.18)$$

Accordingly the SF-terms of the signal transfer functions are given by:

$$\text{SF}_{\text{back}}(\Omega) = \frac{i\tau_1 b_1}{\text{in}_{\text{signal}}}, \quad (6.19)$$

$$\text{SF}_{\text{forward}}(\Omega) = \frac{i\tau_4 a_4}{\text{in}_{\text{signal}}}. \quad (6.20)$$

Note that the Φ_i need to be replaced by $\Phi_i + \Omega L_i / c$ in order to get the correct frequency response for the signal sidebands. Figure 6.13 shows the absolute value of the transfer function $\mathbf{G}(\Omega)$ for $\rho_1^2 = \rho_4^2 = 0.93$. For the illustrated simulation the detuning of first and third resonator were chosen identical ($\Phi_1 = \Phi_3$). Due to the present symmetry, the transfer functions for back and forward port are identical. In order to increase the sensitivity of the instrument both signal ports can be added. It can be seen that this configuration shows a similar behavior than the conventional resonant sideband extraction configuration. For $\Phi_1 = \Phi_3 = 0^\circ$, the configuration shows a broadband response, and by detuning both extraction cavities simultaneously, the transfer function can be tuned to a high sensitivity at a certain frequency.

The bandwidth of the RSE setup can be tuned with the choice of the reflectivity of m_1 and m_4 as shown in Figure 6.14 for the broadband case $\Phi_1 = \Phi_3 = 0^\circ$. A higher reflectivity of m_1 and m_4 leads to a larger bandwidth. If ρ_1^2 and ρ_4^2 exceed the reflectivity ρ_0^2 of the grating, the bandwidth can not be increased any further.

It could be shown that with extraction mirrors placed in forward as well as back-reflected port of a 3-port-grating cavity, a configuration is found that allows for resonant sideband extraction from 3-port grating cavities. A schematic of a full interferometer

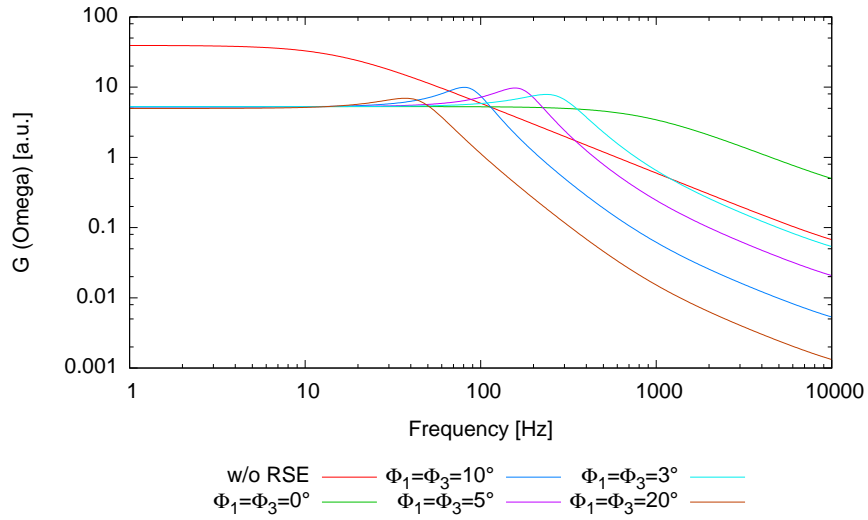


Figure 6.13 — Signal transfer function of 3-port-grating RSE configuration, with $\rho_1^2 = \rho_4^2 = 0.93$. Due to the present symmetry the transfer function of forward and back- reflected port, b'_4 and a'_1 , respectively, are identical.

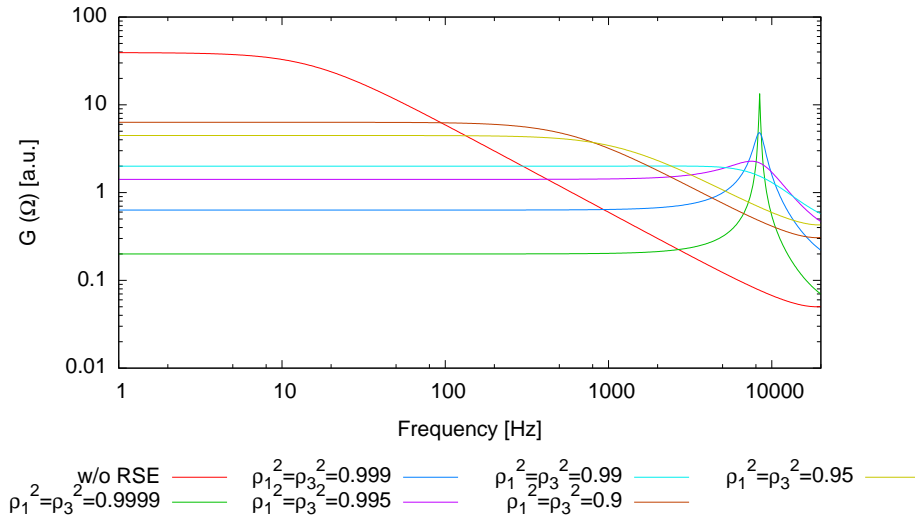


Figure 6.14 — Signal transfer function of the 3-port-grating RSE configuration for different choices of extraction mirror reflectivities ρ_1^2, ρ_4^2 . By increasing the reflectivity of m_1 and m_4 the bandwidth of the RSE setup can be increased. When the extraction mirror reflectivity exceeds the reflectivity of the grating ρ_0^2 , the bandwidth can not be increased any further.

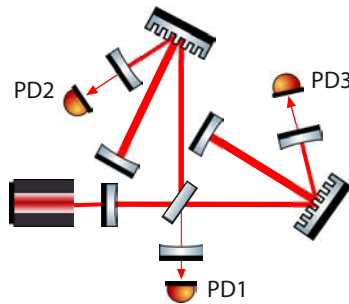


Figure 6.15 — Schematic of a full interferometer using resonant sideband extraction with 3-port-grating arm cavities. Extraction mirrors are placed in the back-reflected port of the grating cavity (a common mirror for both arms in the signal port of the Michelson interferometer), as well as in the forward reflected port (individual mirrors for each arm cavity). The signal is detected at three photodetectors

using this technique is shown in Figure 6.15. In this configuration the signal is detected by three different photodetectors at each of the output ports of the interferometer. The detected signals need to be superposed electronically in an appropriate way to extract the gravitational wave information. With the description of this RSE scheme as a four component cavity it was assumed that also the forward reflection port does not contain any carrier field. For real interferometers though there will be a small amount of residual carrier light in the forward port. This residual carrier light can be removed to avoid a coupling between power recycling cavity and the resonant sideband extraction cavities by overlapping the forward reflected beams of both arm cavities at a beamsplitter. When this second Michelson interferometer is also operated at the dark fringe, a common RSE mirror for both arms can be placed in the differential port of the beamsplitter, without any coupling between signal and carrier fields in the interferometer. In this setup, only two photodetectors (one at each output port of each Michelson interferometer) are needed to extract the signal from the interferometer. This topology will be rather complex, and due to geometrical limitations it is likely that additional optical components for beam steering will be needed. However it could be shown, that 3-port-grating cavities are also compatible with the technique of resonant sideband extraction.

Summary and Outlook

In this work a thorough analysis of 3-port-grating cavities is given with regard to potential applications in future laser interferometric gravitational wave detectors. Due to the additional port of a 3-port-grating, in comparison to a conventional mirror, different phase relations between input and output ports are valid. In Chapter 2 it is shown that the derived phase relations are able to explain the observed behavior of 3-port-grating cavities. The commonly used techniques used for length sensing and control of conventional cavities are extended to reliably control all-reflective 3-port-grating cavities in Chapter 3. Translational phase noise, a noise source not present in traditional interferometers is verified analytically and experimentally in Chapter 4. The phase relations at a 3-port-grating also have extensive consequences, when 3-port-grating cavities are used together with advanced interferometric techniques like power recycling and resonant sideband extraction. In Chapter 5, the behavior of two resonators, that are coupled via a 3-port-grating are investigated with regard to an application in a power recycling configuration. It is shown analytically as well as experimentally, that by using coupled resonators it is possible to significantly increase the stored power in a 3-port-grating arm cavity. In Chapter 6 a configuration that enables resonant sideband extraction in an interferometer with 3-port-grating arm cavities is proposed.

All the experiments presented in this thesis were done with gratings with a total optical loss dominated by scattering of $\approx 0.2\%$. Future work should be dedicated to reduce this loss further, in order to meet the strict requirements on optics for laser interferometric gravitational wave detectors.

So far, all experiments were done using symmetric (binary) gratings. This symmetry leads to the fact, that the diffraction efficiencies of ± 1 st order are equal. Due to this symmetry of the grating, gravitational wave induced signal sidebands are split equally in forward and back-reflected port of the 3-port-grating cavity. Therefore the resonant sideband configuration for these binary gratings is more complex than in traditional interferometers, as it is shown in Chapter 6. In order to preserve the complete signal information, extraction mirrors in both output ports of the cavity are needed. As shown in Chapter 5, the power recycling gain in a 3-port-grating cavity configuration needs to be a factor of two higher than in the comparable traditional cavity, which leads to a high thermal load at the beamsplitter of the interferometer. This is also a consequence of

the symmetry of binary gratings. Therefore, future work should consider non-binary and as a consequence non-symmetric gratings. As preliminary work for the study of interferometer topologies using non-symmetric gratings, the generic 3-port scattering matrix was derived in Chapter 2.

In contrast to a conventional coupling mirror, transmission is a loss channel of 3-port-grating couplers. The high-reflecting dielectric multilayer stack must be designed such that it provides an almost perfect reflectivity for all beams present at the grating. Therefore typically more coating layers are needed than in the traditional mirror case, which leads to a higher coating thermal noise contribution of the coupling component. Apart from improving the coating materials even further a promising path to solve this problem is to unite the ideas of all-reflective optical components with the concept of grating waveguide mirrors that provide high reflectivity with a strongly reduced coating thickness.

Lateral displacement of gratings leads to a noise source that is not present in traditional cavities. First investigations already revealed, that this noise couples differently, depending on the output port of the 3-port-grating cavity [57]. Future work should be targeted at minimizing the noise coupling by careful mechanical and optical design of all-reflective interferometers.

Time-domain Simulation

For the time-domain representation of a 3-port grating cavity, the following code was developed. The simulation code is written in C, and uses the FFTW subroutine for the calculation of the Discrete Fourier Transform (DFT)[60]. Furthermore the window functions given in [61] are utilized. For the implementation of the window functions, the window.h header-file written by Gerhard Heinzl was used.

```
#include <stdio.h>
#include <stdlib.h>
#include <math.h>
#include <complex.h>
#include "field.h"
#include <fftw3.h>
#include "window.h"
#include "fft.h"
#include <string.h>

// constants
#define lambda 1064e-9
#define c 299792458.0

int main(void)
{
    int modfreq,K,factor ,skip , e2s ,wf;
    double a_input ,taum,rhom,eta1 ,eta2 ;
    double eta2max ,eta2min ,eta2mid ,rho0 ,mrf ;
    double mrf2 ,phi_demod ,phi_demod2 ,f_mod ,f_mod2 ,L;
    double xaxis_l ,xaxis_u ,mifactor ,mod_index;
    int stack;
    a_input=1;
```

```

wf=16;
int lfactor=1;
L=9.822 * lfactor;

eta1=sqrt(0.00077);
eta2=sqrt(0.00018);

rho0=sqrt(0.9972119); // actual value
taum=sqrt(0.00004);

e2s=0;
rho0=sqrt(1-(2*eta1*eta1));
eta2max=(1+rho0)/2 -1e-9; // e2s=2
eta2min=(1-rho0)/2+1e-9; // e2s=1
eta2mid=eta2max-((eta2max-eta2min)/2); // e2s=3

//RF sidebands set 1
f_mod=10e6;
mrf=0.1;
phi_demod=M_PI;

//RF sidebands set 2
f_mod2=15.2e6;
mrf2=0;
phi_demod2=M_PI/2.0;

lfactor=1;
L=9.822 * lfactor;
xaxis_l=50;
xaxis_u=1e7;

stack=10000;

K=31000000; // number of samples

factor=1; // factor sampling frequency decrease
skip=7000; // skip first values of timeseries
modfreq=300;
mod_index=0.5; // mod index of sidemotion

```

```
mifactor=1; // factor for mod_index out of cavity
fieldcalc(stack ,mifactor ,lfactor ,eta1 ,eta2 ,f_mod ,
f_mod2 ,mrf ,mrf2 ,phi_demod ,
phi_demod2 ,modfreq , mod_index ,L, rhom,K
,factor ,skip , wf, e2s ,xaxis_1 ,xaxis_u );

return 0;
}
```

```

#include <stdio.h>
#include <stdlib.h>
#include <math.h>
#include <complex.h>
#include <fftw3.h>
#include "window.h"
#include "fft.h"
#include <string.h>
#define lambda 1064e-9
#define c 299792458.0

int fieldcalc(int stack, double mifactor, int lfactor, double eta1
, double eta2, double f_mod, double f_mod2, double mrf, double
mrf2, double phi_demod, double phi_demod2, int modfreq, double
mod_index, double L, double rhom, int K, int factor, int skip,
int wf, int e2s, double xaxis_l, double xaxis_u)
{
int n;
double a_input=1;
double complex an, anout, trans, c1, c3, a22, rho0mp;
double complex an_usb1, an_usb2, an_lsb1, an_lsb2;
double complex a22_usb1, a22_lsb1, a22_usb2, a22_lsb2;
double complex anout_usb1, anout_lsb1, anout_usb2;
double complex anout_lsb2, trans_usb1, trans_lsb1, trans_usb2;
double complex trans_lsb2, c3_usb1, c3_lsb1, c3_usb2, c3_lsb2;
double complex c1_usb1, c1_lsb1, c1_usb2, c1_lsb2, c1_rf1;
double complex C1_demod_rf1, c1_rf2, C1_demod_rf2, c3_rf1;
double complex C3_demod_rf1, c3_rf2, C3_demod_rf2;
double complex trans_rf1, Trans_demod_rf1, trans_rf2,
Trans_demod_rf2;
double C1, C3, Intra, Trans;
double omega_mod;
double J_0, J_1, J2_0, J2_1, f_carr, f_sb_l, f_sb_u, f_sb2_l, f_sb2_u;
double complex a_in_sb1, a_in_sb2, a_in;
double PHI_usb1, PHI_lsb1, PHI_usb2, PHI_lsb2;
double phi11, phi12, phi13, phi22, phi12out;
int uwe, i, j;

double complex Intraa[stack], C3a[stack], C1a[stack], Transa[stack
];
double Trans_demod_rf1a[stack], C3_demod_rf1a[stack],
C1_demod_rf1a[stack], Trans_demod_rf2a[stack], C3_demod_rf2a[

```

```

    stack ], C1_demod_rf2a [ stack ];
double taum=sqrt(1-(rhom * rhom));
omega_mod=2*M_PI*modfreq;
double FSR = c / 2.0 / L;
printf("L=%e\n", L);
printf("FSR=%e\n", FSR);
    FILE *fp;
    FILE *fp1;
    FILE *fp2;
    FILE *fp3;
    FILE *fp4;
    FILE *fp5;
    FILE *fp6;
    FILE *fp7;
    FILE *fp8;
    FILE *fp9;

    int type=wf;
    double PHI=0;
    double a=eta2;
    double b=eta1/sqrt(1-(a * a));
    double rho0 = sqrt(1-2*(eta1 * eta1));
    double eta0=sqrt((1-(a * a))*(1-(b * b)));
    // print out some information
    // double F = M_PI*sqrt(rhom*rho0)/(1 - rhom*rho0);
    // printf("Cavity linewidth           : %lf MHz\n", FSR/F
    *1e-6);
    // printf("Phase modulation frequency: %lf MHz\n",
    omega_mod*1e-6);
    //
    double L1=L;
char suffix[100]="_";
char under[]="_";
char hz[]="Hz";
char khz[]="kHz";
char mhz[]="MHz_idx";
char pi[]="pi";
char rf1[]="RF1_";
char rf2[]="RF2_";
char lf[]="lf";
char mif[]="mif";
char *prefix[10];

```

```

        // prefix = (char**) malloc(50* sizeof(
            char*));

// if(modfreq > 999)
// {
//     sprintf(suffix, "%s%d", suffix, modfreq/1000);
//     strcat(suffix, khz);
// }
// if(modfreq < 1000)
// {
//     sprintf(suffix, "%s%d", suffix, modfreq);
//     strcat(suffix, hz);
// }

strcat(suffix, under);
// sprintf(suffix, "%s%d", suffix, mod_index);
sprintf(suffix, "%s%1.2f", suffix, mod_index);
strcat(suffix, pi);
strcat(suffix, under);

if(mrf > 0)
{
    strcat(suffix, rf1);
    sprintf(suffix, "%s%.2f", suffix, f_mod
        /1e6);
    strcat(suffix, mhz);
    sprintf(suffix, "%s%.1f", suffix, mrf);

    strcat(suffix, under);
}
if(mrf2 > 0)
{
    strcat(suffix, rf2);
    sprintf(suffix, "%s%.2f",
        suffix, f_mod2/1e6);
    strcat(suffix, mhz);
    sprintf(suffix, "%s%.1f",
        suffix, mrf2);
    strcat(suffix, under);
}

```

```
        strcat(suffix, lf);
        sprintf(suffix, "%s%d", suffix, lfactor);
            strcat(suffix, under);
            strcat(suffix, mif);
        sprintf(suffix, "%s%.1f", suffix, mifactor);
        strcat(suffix, under);
    if (e2s==0)
    {
        char e2sc[]="GLA.txt";
        strcat(suffix, e2sc);
    }
    if (e2s==1)
    {
        char e2sc[]="e2min.txt";
        strcat(suffix, e2sc);
    }

    if (e2s==2)
    {
        char e2sc[]="e2max.txt";
        strcat(suffix, e2sc);
    }
    if (e2s==3)
    {
        char e2sc[]="e2mid.txt";
        strcat(suffix, e2sc);
    }
    if (e2s==4)
    {
        char e2sc[]="F187.txt";
        strcat(suffix, e2sc);
    }

        if (e2s==5)
        {
            char e2sc[]="mifactor100.txt";
            strcat(suffix, e2sc);
        }
        uwe=0;

        for (uwe=0;uwe<10;uwe++)
        {
```

```

        prefix[uwe] = (char*)malloc(100*sizeof(
            char));
    }

    strcpy(prefix[0], "C1");
    strcpy(prefix[1], "C3");
    strcpy(prefix[2], "Trans");
    strcpy(prefix[3], "Intra");
    strcpy(prefix[4], "C1demod_rf1");
    strcpy(prefix[7], "C1demod_rf2");
    strcpy(prefix[5], "C3demod_rf1");
    strcpy(prefix[8], "C3demod_rf2");
    strcpy(prefix[6], "Transdemod_rf1");
    strcpy(prefix[9], "Transdemod_rf2");

    i=0;
    for(i = 0; i < 10; i++)
    {
        strcat(prefix[i], suffix
            );
        //      printf(" uhi:%i:\ t%s\n",
            i, prefix[i]);
    }

fp= fopen(prefix[0], "w");
fp1=fopen(prefix[1], "w");
fp2=fopen(prefix[2], "w");
fp3=fopen(prefix[3], "w");
fp4=fopen(prefix[4], "w");
fp5=fopen(prefix[5], "w");
fp6=fopen(prefix[6], "w");

fp7=fopen(prefix[7], "w");
fp8=fopen(prefix[8], "w");
fp9=fopen(prefix[9], "w");

// start the actual calculation
mod_index=mod_index*M_PI;
    a22=0.0;
    an=0.0;
    a22_usb1=0.0;
    a22_lsb1=0.0;

```



```

a22_usb2=0.0;
a22_lsb2=0.0;

phi12 = 0.0;
phi11 = 2*phi12;
phi13 = acos(-b*b/(2*a)*sqrt((1-a*a)/(1-b*b)));
phi22 = acos(a*(b*b/(2*a*a)*(1-a*a)/(1-b*b) - 1));
printf("phi22=%e\n",phi22 );
rho0mp = -a*b*b*cexp(I*(2*phi12 - phi11)) + (1 - b*b)*
    cexp(I*phi22);
PHI = PHI - phi11 - carg(rho0mp);
printf("PHI=%e\n",PHI_usb1);

f_carr = c/lambda;

    a_in=a_input;
    double omega_rf1=2.0*M_PI*10e6;
    double omega_rf2=2.0*M_PI*15.2e6;
    double complex p[3];
    p[0]=0;
    p[1]=0;
    p[2]=0;
for(n = 0; n < K+1; n++)
{
    phi12 = mod_index * M_PI * sin(n /( 2.0 * FSR)
        * omega_mod) + mod_index * M_PI ;
    phi11 = 2.0*phi12;

    phi12out=phi12;
    rho0mp = -a*b*b*cexp(I*(2*phi12 - phi11)) + (1
        - b*b)*cexp(I*phi22);
a_in=a_input * cexp(I * mrf * cos(2.0 * M_PI * f_mod *
    n/(2.0* FSR))) *
    cexp(I * mrf2 * cos(2.0 * M_PI * f_mod2 * n/(2.0 * FSR
        )));
    a22=an;

```

```

//an = eta1*cexp(I*phi12)*a_in + rhom*cexp(I*
    PHI)*rho0mp*an;

an = eta1*cexp(I*phi12)*a_in + rhom*cexp(I*PHI)
    *rho0mp*p[2];
p[0]=an;
p[2]=p[1];
p[1]=p[0];

    Intraa[i]=cabs(an) * cabs(an);
//    trans=an * cexp(0.5*I*PHI) * I * taum;
    trans=p[1]*cexp(0.5*I*PHI)* I * taum;
    Transa[i]=cabs(trans) * cabs(trans);
//    anout= a22 * rhom * cexp(I * PHI);
anout= p[2]*rhom*cexp(I * PHI);
    c3= (eta0 * a_in * cexp(I * phi13)) + (anout *
        eta1 * cexp(-I * phi12out)) ;
    C3a[i]= cabs(c3) * cabs(c3);

    c1= (eta2 * a_in * cexp(I * phi11)) +( anout *
        eta1 * cexp(I * phi12out ) );
    C1a[i]= cabs(c1) * cabs(c1);

    Trans_demod_rf1a[i]=Transa[i]*cos(n/(2.0 * FSR)
        *omega_rf1+phi_demod);
    Trans_demod_rf2a[i]=Transa[i]*cos(n/(2.0 * FSR)
        *omega_rf2+phi_demod2);

    C3_demod_rf1a[i]=C3a[i]*cos(n/(2.0 * FSR)*
        omega_rf1+phi_demod);
    C3_demod_rf2a[i]=C3a[i]*cos(n/(2.0 * FSR)*
        omega_rf2+phi_demod2);

    C1_demod_rf1a[i]=C1a[i]*cos(n/(2.0 * FSR)*
        omega_rf1+phi_demod);
    C1_demod_rf2a[i]=C1a[i]*cos(n/(2.0 * FSR)*
        omega_rf2+phi_demod2);

i++;

```

```

if (i==stack)
{
    for(j = 0; j < stack; j++)
    {
        //      fprintf(fp , "%e\n" ,C1a[j]);
        //      fprintf(fp1 , "%e\n" ,C3a[j] );
        //      fprintf(fp2 , "%e\n" ,Transa[j]);
        //      fprintf(fp3 , "%e\n" ,Intraa[j]);
        fprintf(fp4 , "%e\n" ,C1_demod_rf1a[j]);
        fprintf(fp5 , "%e\n" ,C3_demod_rf1a[j] );
        fprintf(fp6 , "%e\n" ,Trans_demod_rf1a[j]);
        //      fprintf(fp7 , "%e\n" ,C1_demod_rf2a[j]);
        //      fprintf(fp8 , "%e\n" ,C3_demod_rf2a[j]);
        //      fprintf(fp9 , "%e\n" ,Trans_demod_rf2a[j]);

    }
    i=0;
}

fclose(fp);
fclose(fp1);
fclose(fp2);
fclose(fp3);
fclose(fp4);
fclose(fp5);
fclose(fp6);
fclose(fp7);
fclose(fp8);

fft_func(modfreq,K, skip , type , factor ,FSR, suffix , prefix , mrf ,mrf2 ,
        L1);
//plotter(suffix , prefix , xaxis_l , xaxis_u , mrf , mrf2 ,K, factor);

return 0;
}

```

```

plotter(char suffix[100],char *prefix[10],double xaxis_l,double
        xaxis_u,double mrf,double mrf2,int K, int factor)
{
    int limit= K/factor;
    char suffix2[100];
    strcpy(suffix2 , suffix);
    char* prefix2[10];
    int j;
    for (j=0;j<10;j++)

        {
        prefix2[j] = (char*)malloc(100*sizeof(char));
        }

    strcpy(prefix2[0],"ls_C1");
    strcpy(prefix2[1],"ls_C3");
    strcpy(prefix2[2],"ls_Trans");
    strcpy(prefix2[3],"ls_Intra");
    strcpy(prefix2[4],"ls_C1demod_rf1");
    strcpy(prefix2[7],"ls_C1demod_rf2");
    strcpy(prefix2[5],"ls_C3demod_rf1");
    strcpy(prefix2[8],"ls_C3demod_rf2");
    strcpy(prefix2[6],"ls_Transdemod_rf1");
    strcpy(prefix2[9],"ls_Transdemod_rf2");

    for(j = 0; j < 10; j++)
    {
        strcat(prefix2[j],suffix2);
        //printf("uhi:%i:\t%s\n",j,prefix2[j]);
    }

    FILE *fout;
    fout = popen("gnuplot -persist", "w");
    fprintf(fout, "set term pdf noenhanced size 13cm,10cm;"
        );
    fprintf(fout, "set output 'ts_%.pdf';",suffix);
    fprintf(fout, "set ylabel 'Voltage [V]';");
    fprintf(fout, "set xlabel 'Number of sample []';");
    fprintf(fout, "set title 'TS %s';",suffix);
    fprintf(fout, "set xrange [0:%d];",limit);
    fprintf(fout, "plot '%s' w l title 'C1','%s' w l title
        'C3','%s' w l title 'Trans';\n",prefix[0],prefix[1],
        prefix[2]);
}

```

```

fprintf(fout, "reset;");
fprintf(fout, "set term pdf noenhanced size 13cm,10cm;"
);
fprintf(fout, "set output 'ls_%.pdf';", suffix);
fprintf(fout, "set xlabel 'Frequency [Hz]';");
fprintf(fout, "set ylabel 'Voltage [V]';");
fprintf(fout, "set logscale x;");
fprintf(fout, "set logscale y;");
fprintf(fout, "set xrange [%f:%f];", xaxis_l, xaxis_u);
fprintf(fout, "set title 'ls_%.';", suffix);
fprintf(fout, "plot '%s' w l title 'C1', '%s' w l title
'C3', '%s' w l title 'Trans';\n", prefix2[0], prefix2
[1], prefix2[2]);

if (mrf>0)
{
    fprintf(fout, "reset;");
    fprintf(fout, "set term pdf noenhanced size 13
cm,10cm;");
    fprintf(fout, "set output 'ls_demod_rf1_%.pdf
';", suffix);
    fprintf(fout, "set xlabel 'Frequency [Hz]';");
    fprintf(fout, "set ylabel 'Voltage [V]';");
    fprintf(fout, "set logscale x;");
    fprintf(fout, "set logscale y;");
    fprintf(fout, "set xrange [%f:%f];", xaxis_l,
xaxis_u);
    fprintf(fout, "set title 'ls_demod_rf1_%.';",
suffix);
    fprintf(fout, "plot '%s' w l title 'C1', '%s' w
l title 'C3', '%s' w l title 'Trans';\n",
prefix2[4], prefix2[5], prefix2[6]);
}

if (mrf2>0)
{
    fprintf(fout, "reset;");
    fprintf(fout, "set term pdf noenhanced size 13
cm,10cm;");
    fprintf(fout, "set output 'ls_demod_rf2_%.pdf
';", suffix);
    fprintf(fout, "set xlabel 'Frequency [Hz]';");
    fprintf(fout, "set ylabel 'Voltage [V]';");

```

```
        fprintf(fout, "set logscale x;");
        fprintf(fout, "set logscale y;");
        fprintf(fout, "set xrange [%f:%f];", xaxis_l,
                xaxis_u);
        fprintf(fout, "set title 'ls_demod_rf2_%s '",
                suffix);
        fprintf(fout, "plot '%s' w l title 'C1', '%s' w
                l title 'C3', '%s' w l title 'Trans';\n",
                prefix2[7], prefix2[8], prefix2[9]);

    }

    fclose(fout);

}
```

```

#include <stdio.h>
#include <stdlib.h>
#include <fftw3.h>
#include <math.h>
#include "complex.h"
#include "window.h"
#include <string.h>
#define TWOPI 6.28318530717959

int fft_func(int modfreq,int Samples_tot, int skip,int type,int
            fact,double FSR,char suffix[100],char *prefix[10], double
            mrf,double mrf2,double L)
{
int test=0;
double fs;

skip=7000;
char suffix2[100];
// Filename Construction
strcpy(suffix2,suffix);
//char** prefix2;
char* prefix2[10];
char* prefix3[6];
int j;
//prefix2 = (char**)malloc(50*sizeof(char*));
for (j=0;j<10;j++)

{
prefix2[j] = (char*)malloc(100*sizeof(char));
}
for (j=0;j<6;j++)

{
prefix3[j] = (char*)malloc(100*sizeof(char));
}

strcpy(prefix2[0],"ls_C1");
strcpy(prefix2[1],"ls_C3");
strcpy(prefix2[2],"ls_Trans");
strcpy(prefix2[3],"ls_Intra");
strcpy(prefix2[4],"ls_C1demod_rf1");
strcpy(prefix2[5],"ls_C3demod_rf1");

```

```

strcpy (prefix2 [6], "ls_Transdemod_rf1");
strcpy (prefix2 [7], "ls_C1demod_rf2");
strcpy (prefix2 [8], "ls_C3demod_rf2");
strcpy (prefix2 [9], "ls_Transdemod_rf2");

strcpy (prefix3 [0], "ls_C1demodpeak_rf1_m_idx0.1 pi . txt");
strcpy (prefix3 [1], "ls_C3demodpeak_rf1_m_idx0.1 pi . txt");
strcpy (prefix3 [2], "ls_Transdemodpeak_rf1_m_idx0.1 pi . txt");
strcpy (prefix3 [3], "ls_C1peak_rf1_m_idx0.1 pi . txt");
strcpy (prefix3 [4], "ls_C3peak_rf1_m_idx0.1 pi . txt");
strcpy (prefix3 [5], "ls_Transpeak_rf1_m_idx0.1 pi . txt");

for (j = 0; j < 10; j++)
{
    strcat (prefix2 [j], suffix2);
}

// Variables for FFT

int N=Samples_tot-skip;
int Uwe=(Samples_tot/fact)-skip;
N=Uwe;

char test1 [80];
double* value= malloc (Samples_tot*sizeof (double));
    if (value==NULL)
    {
        printf ("Alarm!\n");
    }

fcomplex a;

double total=0;

int half;
double req_psl1=25;
char name [20];
double psl1, rov, nenbw1, nenbw2, winsum, winsum2, w3db, flatness;
double *x;
int nfft;
int i, len;

```



```

double *psd;
double *freq;

half=0;
nfft=N; // Number of samples

double fres;

FILE *fp;
FILE *fp1;
FILE *fp2;
FILE *fp3;
FILE *fp4;
FILE *fp5;
FILE *fp6;
FILE *fp7;
FILE *fp8;
FILE *fp9;
fftw_complex *in, *out;
fftw_plan p;

//      double L=9.822;
      double c=299792458;
      //fs =FSR/fact; // hard coded
      fs=FSR*2;
      fres=fs/N;
printf("fres:%e\n", fres);
printf("fs:%e\n", fs);

in = (fftw_complex*) fftw_malloc(sizeof(fftw_complex) * N);
out = (fftw_complex*) fftw_malloc(sizeof(fftw_complex) * N);

// window function
if (half)
len = nfft / 2 + 1;
else
len = nfft;
x = malloc (len * sizeof (double));
//assert (x != NULL);
set_window (type, req_psl1, name, &psl1, &rov,
            &nenbw1, &w3db, &flatness);
makewin (nfft, half, x, &winsum, &winsum2, &nenbw2);

```

```

int count2=0;

/* FFT all ports */
// read time series
psd = malloc (((N/2)+1) * sizeof (double));
freq = malloc (((N/2)+1) * sizeof (double));

int anzahl;
// if(mrf==0)
// {
//     anzahl=4;
// }
// if(mrf>0)
// {
//     anzahl=7;
// }
// }
// if(mrf2>0)
// {
//     anzahl=10;
// }
// }
// for(count2=0;count2<anzahl; count2++)
for(count2=4;count2<7;count2++)
{

    i=0;

    fp=fopen(prefix[count2],"r");
    while (feof(fp) == 0)
        {
            fgets(test1 , 80, fp);

                value[i]=atof(test1);
                i=i+1;
            }
    fclose(fp);
    if( remove( prefix[count2]) == -1 )
        perror( "Error deleting File" );
    else
        puts( "File deleted" );
//     cut time series for FFT
//     and multiply with window function

```

```

for(i = 0; i < N; ++i)
{
    //value[i+3000]=value[i+3000]-gesamt;
    in[i][0]=value[i+skip];/*x[i];
    in[i][1]=0;

    total=total+in[i][0];
}

for(i = 0; i < N; ++i)
{
    //value[i+3000]=value[i+3000]-gesamt;
    in[i][0]=(in[i][0]-(total/N))*x[i];

}
// FFT
p = fftw_plan_dft_1d(N, in , out , FFTW_FORWARD,
    FFTW_ESTIMATE);

fftw_execute(p); /* repeat as needed */

// calculate PSD and save
//free(x);
// psd = malloc (((N/2)+1) * sizeof (double));
// freq = malloc (((N/2)+1) * sizeof (double));
fp2=fopen(prefix2[count2], "w");

    for(i = 0; i < N/2 *1/20; ++i)
{
    a.r=out[i][0];
    a.i=out[i][1];

    psd[i]=sqrt((2*Cabs(a)*Cabs(a)/(winsum*winsum))
        );
    freq[i]=i*fres;

    fprintf(fp2, "%.8e %.8e\n", freq[i], psd[i]);

if(count2==0 && fres*i>modfreq && test==0)
{
fp3=fopen(prefix3[3], "a");
if(psd[i]>psd[i-1])

```

```

{
fprintf(fp3, "%.8e %.8e\n", freq[i], psd[i]);
}
else fprintf(fp3, "%.8e %.8e\n", freq[i-1], psd[i-1]);
fclose(fp3);
test=1;
}

if(count2==1 && fres*i>modfreq && test==0)
{
fp3=fopen(prefix3[4], "a");
if(psd[i]>psd[i-1])
{
fprintf(fp3, "%.8e %.8e\n", freq[i], psd[i]);
}
else fprintf(fp3, "%.8e %.8e\n", freq[i-1], psd[i-1]);
fclose(fp3);
test=1;
}
if(count2==2 && fres*i>modfreq && test==0)
{
fp3=fopen(prefix3[5], "a");
if(psd[i]>psd[i-1])
{
fprintf(fp3, "%.8e %.8e\n", freq[i], psd[i]);
}
else fprintf(fp3, "%.8e %.8e\n", freq[i-1], psd[i-1]);
fclose(fp3);
test=1;
}

if(count2==4 && fres*i>modfreq && test==0)
{
fp3=fopen(prefix3[0], "a");
if(psd[i]>psd[i-1])
{
fprintf(fp3, "%.8e %.8e\n", freq[i], psd[i]);
}
else fprintf(fp3, "%.8e %.8e\n", freq[i-1], psd[i-1]);
fclose(fp3);
}

```

```
test=1;
}
if(count2==5 && fres * i >modfreq && test==0)
{
fp3=fopen(prefix3[1], "a");
if(psd[i]>psd[i-1])
{
fprintf(fp3, "%.8e %.8e\n", freq[i], psd[i]);
}
else fprintf(fp3, "%.8e %.8e\n", freq[i-1], psd[i-1]);
fclose(fp3);
test=1;
}
if(count2==6 && fres*i>modfreq && test==0)
{
fp3=fopen(prefix3[2], "a");
if(psd[i]>psd[i-1])
{
fprintf(fp3, "%.8e %.8e\n", freq[i], psd[i]);
}
else fprintf(fp3, "%.8e %.8e\n", freq[i-1], psd[i-1]);
fclose(fp3);
test=1;
}
}
fclose(fp2);
fclose(fp3);
test=0;

}

    fftw_destroy_plan(p);
    fftw_free(in); fftw_free(out);
    fclose(fp);

    free(x);
    free(psd);
    free(freq);
    return 0;
}
```


Bibliography

- [1] A. Einstein
„*Approximative integration of the field equations of gravitation*“
Sitzungsbericht Preuss. Akad. Wiss. Berlin, 688 (1916).

- [2] R. A. Hulse
„*The discovery of the binary pulsar (PSR 1913+16)*“
Rev. Mod. Phys. **66**, 699 (1994).

- [3] J. H. Taylor
„*Binary Pulsars and relativistic gravity*“
Rev. Mod. Phys. **66**, 711 (1994).

- [4] P. Aufmuth, K. Danzmann
„*Gravitational wave detectors*“
New Journal of Physics **7**, 202 (2005).

- [5] J. Weber
„*Evidence for discovery of Gravitational Radiation*“
Phys. Rev. Lett. **22**, 1320 (1969).

- [6] P. Astone
„*Resonant mass detectors: present status*“
Class. Quantum Grav. **19**, 1227 (2002).

- [7] K. Danzmann and the LISA Science Team
„*LISA - An ESA cornerstone mission for the detection and observation of gravitational waves*“
Advances in Space Research **32**, 1233 (2003).

- [8] B. Abbott et al.
„*LIGO: the Laser Interferometer Gravitational-Wave Observatory*“
Reports on Progress in Physics **72**, 076901 (2009).

- [9] F. Acernese et al.
„*Status of VIRGO*“
Class. Quantum Grav. **21**, S385 (2004).

- [10] H. Grote for the LIGO Scientific Collaboration
„The status of GEO600“
Class. Quantum Grav. **25**, 114043 (2008).
- [11] R. Takahashi et al.
„Status of TAMA300“
Class. Quantum Grav. **21**, S403 (2004).
- [12] S. Goßler
„The suspension systems of the interferometric gravitational-wave detector GEO 600“
Ph.D thesis, Universität Hannover, (2004).
- [13] S. A. Hughes, K. S. Thorne
„Seismic gravity-gradient noise in interferometric gravitational-wave detectors“
Phys. Rev. D **58**, 122002 (1998).
- [14] H. B. Callen, T. A. Welton
„Irreversibility and Generalized Noise“
Phys. Rev. **83**, 34 (1951).
- [15] G. M. Harry, A. M. Gretarsson, P. R. Saulson, S. E. Kittelberger, S. D. Penn, W. J. Startin, S. Rowan, M. M. Fejer, D. R. M. Crooks, G. Cagnoli, J. Hough, N. Nakagawa
„Thermal noise in interferometric gravitational wave detectors due to dielectric optical coatings“
Class. Quantum Grav. **19**, 897 (2002).
- [16] D. R. M. Crooks, G. Cagnoli, M. M. Fejer, A. Gretarsson, G. Harry, J. Hough, N. Nakagawa, S. D. Penn, R. Route, S. Rowan, P. H. Sneddon
„Experimental measurements of coating mechanical loss factors“
Class. Quantum Grav. **21**, S1059 (2004).
- [17] G. M. Harry, H. Armandula, E. Black, D. R. M. Crooks, G. Cagnoli, J. Hough, P. Murray, S. Reid, S. Rowan, P. Sneddon, M. M. Fejer, R. Route, S. D. Penn
„Thermal noise from optical coatings in gravitational wave detectors“
Appl. Opt. **45**, 1569 (2006).
- [18] F. Ya. Khalili
„Reducing the mirrors coating noise in laser gravitational-wave antennae by means of double mirrors“
Phys. Lett. A **334**, 67 (2005).
- [19] A. Bunkowski, O. Burmeister, D. Friedrich, K. Danzmann, R. Schnabel
„High reflectivity grating waveguide coatings for 1064 nm“
Class. Quantum Grav. **23**, 7297, (2006).
- [20] F. Brückner, T. Clausnitzer, O. Burmeister, D. Friedrich, E.-B. Kley, K. Danzmann, A. Tünnermann, R. Schnabel

- „Monolithic dielectric surfaces as new low-loss light-matter interfaces“*
Opt. Lett. **33**, 264 (2008).
- [21] V. B. Braginsky, M. L. Gorodetsky, S. P. Vyatchanin
„Thermo-refractive noise in gravitational wave antennae“
Phys. Lett. A **271**, 303 (2000).
- [22] V. B. Braginsky, M. L. Gorodetsky, S. P. Vyatchanin
„Thermodynamical fluctuations and photo-thermal shot noise in gravitational wave antennae“
Phys. Lett. A **264**, 1 (1999).
- [23] E. D. Black, A. Villar, K. G. Libbrecht
„Thermoelastic-Damping Noise from Sapphire Mirrors in a Fundamental-Noise-Limited Interferometer“
Phys. Rev. Lett. **93**, 241101 (2004).
- [24] M. Evans, S. Ballmer, M. Fejer, P. Fritschel, G. Harry, G. Ogin
„Thermo-optic noise in coated mirrors for high-precision optical measurements“
Phys. Rev. D **78**, 102003 (2008).
- [25] K. Kazuaki and the LCGT Collaboration
„The status of LCGT“
Class. Quantum Grav. **23**, S215 (2006).
- [26] H. Vahlbruch
„Squeezed Light for Gravitational Wave Astronomy“
Ph.D Thesis, Leibniz Universität Hannover, Hannover (2008).
- [27] V. B. Braginsky and F. Ya. Khalili
„Quantum Measurements“
Cambridge University Press, Cambridge, (1992).
- [28] S. Hild, H. Lück, W. Winkler, K. Strain, H. Grote, J. Smith, M. Malec, M. Hewitson, B. Willke, J. Hough, K. Danzmann
„Measurement of a low-absorption sample of OH-reduced fused silica“
Appl. Opt. **45**, 7269 (2006).
- [29] K. A. Strain, K. Danzmann, J. Mizuno, R. G. Nelson, A. Rüdiger, R. Schilling, W. Winkler
„Thermal lensing in recycling interferometric gravitational wave detectors“
Phys. Lett. A **194**, 124 (1994).
- [30] W. Winkler, K. Danzmann, A. Rüdiger, R. Schilling
„Heating by optical absorption and the performance of interferometric gravitational-wave detectors“
Phys. Rev. A **44**, 7022 (1991).

- [31] R. W. P. Drever
„Concepts for extending the ultimate sensitivity of interferometric Gravitational Wave Detectors Using Non-Transmissive Optics with Diffractive or Holographic Coupling“
Proceedings of the Seventh Marcel Grossman Meeting on General Relativity
M. Keiser and R.T. Jantzen (ed.), World Scientific, Singapore (1995).
- [32] C. Palmer
„Diffraction Gratings Handbook“
Thermo RGL, Rochester (2002).
- [33] The LIGO Scientific Collaboration & The Virgo Collaboration
„An upper limit on the stochastic gravitational-wave background of cosmological origin“
Nature **460**, 990 (2009).
- [34] J. Smith for the LIGO Scientific collaboration
„The path to the enhanced and advanced LIGO gravitational-wave detectors“
Class. Quantum Grav. **26**, 114013 (2009).
- [35] Einstein Telescope Project webpage
<http://www.et-gw.eu>
- [36] O. Burmeister *„Fabry-Perot Resonatoren mit diffraktiven Einkopplern“*
Diploma thesis, Universität Hannover (2005).
- [37] B. W. Shore, M.D. Perry, J. A. Britten, R. D. Boyd, M. D. Feit, H. T. Nuygen, R. Chow, G. E. Loomis, L. Li
„Design of high-efficiency dielectric reflection gratings“
J. Opt. Soc. Am. A **14**, 1124 (1997).
- [38] K.-X. Sun, R. L. Byer *„All-reflective Michelson, Sagnac, and Fabry-Perot interferometers based on grating beam splitters“*
Opt. Lett. **23**, 567 (1998).
- [39] D. Friedrich, O. Burmeister, A. Bunkowski, T. Clausnitzer, S. Fahr, E.-B. Kley, A. Tünnermann, K. Danzmann, R. Schnabel
„Diffractive beam splitter characterization via a power-recycled interferometer“
Opt. Lett. **33**, 101 (2008).
- [40] S. Fahr, T. Clausnitzer, E.-B. Kley and A. Tünnermann
„Reflective diffractive beam splitter for laser interferometers“
Appl. Opt. **46**, 6092 (2007).
- [41] A. Bunkowski, O. Burmeister, K. Danzmann, R. Schnabel, T. Clausnitzer, E.-B. Kley, A. Tünnermann
„Optical Characterization of ultra-high diffraction efficiency gratings“
Appl. Opt **45**, 23 5795 (2006).

- [42] P. P. Lu, K.-X. Sun, R. L. Byer, J. A. Britten, H. T. Nguyen, J. D. Nissen, C. C. Larson, M. D. Aasen, T. C. Carlson, C. R. Hoaglan
„Precise diffraction efficiency measurements of large-area greater-than-99%-efficient dielectric gratings at the Littrow angle“
 Opt. Lett. **34**, 1708 (2009).
- [43] A. Bunkowski, O. Burmeister, P. Beyersdorf, K. Danzmann, R. Schnabel, T. Clausnitzer, E.-B. Kley, A. Tünnermann
„Low-loss grating for coupling to a high-finesse cavity“
 Opt. Lett. **29**, 2342 (2004).
- [44] A. Bunkowski, O. Burmeister, K. Danzmann, R. Schnabel
„Input-Output relations for a three-port grating coupled Fabry-Perot cavity“
 Opt. Lett. **30**, 1183 (2005).
- [45] A. E. Siegman
„Lasers“
 University Science Books, (1986).
- [46] P. Ditâ
„Parametrisation of unitary matrices“
 J. Phys. A: Math. Gen. **15**, 3465 (1982).
- [47] R. Schnabel, A. Bunkowski, O. Burmeister, K. Danzmann
„Three-port beam splitters-combiners for interferometer applications“
 Opt. Lett. **31**, 658 (2006).
- [48] A. Thüring
„Investigations of coupled and Kerr non-linear optical resonators“
 Ph.D Thesis, Leibniz Universität Hannover, (2009).
- [49] T. Clausnitzer *„Kontrolle der Beugungseffizienzen dielektrischer Gitter“*
 Ph.D Thesis, Friedrich-Schiller Universität Jena, (2007).
- [50] A. Bunkowski, O. Burmeister, K. Danzmann, R. Schnabel, T. Clausnitzer, E.-B. Kley, A. Tünnermann
„Demonstration of three-port grating phase relations“
 Opt. Lett. **31**, 2384 (2006).
- [51] E. D. Black
„An introduction to Pound-Drever-Hall laser frequency stabilization“
 Am. J. Phys. **69**, 79 (2001).
- [52] I. S. Gradshteyn, I. M. Ryzhik
„Tables of Series, Products and Integrals“
 Harri Deutsch (1981).

- [53] G. Heinzl
„Advanced optical techniques for laser-interferometric gravitational-wave detectors“
MPQ Report **243**, (1999).
- [54] B. Willke, N. Uehara, E. K. Gustafson, R. L. Byer
„Spatial and temporal filtering of a 10-W Nd:YAG laser with a Fabry-Perot ring-cavity premode cleaner“
Opt. Lett. **23**, 1704 (1998).
- [55] J. R. Taylor
„Interferometric Experiments Towards Advanced Gravitational Wave Detectors“
Ph.D Thesis, University of Glasgow, (2008).
- [56] S. Wise, V. Quetschke, A.J. Deshpande, G. Müller, D.H. Reitze, D.B. Tanner, B.F. Whiting, Y. Chen, A. Tünnermann, E.-B. Kley, T. Clausnitzer
„Phase effects in the diffraction of light: beyond the grating equation“
Phys. Rev. Lett. **95**, 013901 (2005).
- [57] J. Hallam, S. Chelkowski, A. Freise, S. Hild, B. Barr, K. A. Strain, O. Burmeister, R. Schnabel
„Coupling of lateral grating displacement to the output ports of a diffractive Fabry-Perot cavity“
J. Opt. A: Pure Appl. Opt. **11**, 085502 (2009).
- [58] A. Freise, A. Bunkowski, R. Schnabel
„Phase and alignment noise in grating interferometers“
New Journal of Physics **9**, 433 (2007).
- [59] Homepage of the simulation tool Finesse
<http://www.rzg.mpg.de/adf/>
- [60] Homepage of the FFTW project
<http://www.fftw.org/>
- [61] G. Heinzl, A. Rüdiger, R. Schilling
„Spectrum and spectral density estimation by the Discrete Fourier transform (DFT), including a comprehensive list of window functions and some new at-top windows.“
http://www.rssd.esa.int/SP/LISAPATHFINDER/docs/Data_Analysis/GH_FFT.pdf
- [62] M. Edgar
Personal communication
- [63] P. Fritschel, D. Shoemaker, R. Weiss
„Demonstration of light recycling in a Michelson interferometer with Fabry-Perot cavities“
Appl. Opt. **31**, 1412 (1992).

- [64] H. Kogelnik, T. Li
„Laser Beams and Resonators“
Appl. Opt. **5**, 1550 (1966).
- [65] M. Britzger
„Dreiport-Gitter-Resonator mit Power-Recycling“
Diploma Thesis, Leibniz Universität Hannover, (2007).
- [66] B. W. Barr
„Experimental Investigations into Advanced Configurations and Optical Techniques for Laser Interferometric Gravitational Wave Detectors“
Ph.D. Thesis, University of Glasgow, (2003).
- [67] B. W. Barr, S. H. Huttner, J. R. Taylor, B. Sorazu, M. V. Plissi, K. A. Strain
„Optical modulation techniques for length sensing and control of optical cavities“
Appl. Opt. **46**, 7739 (2007).
- [68] D. S. Rabeling, S. Goßler, J. Cumpston, M. B. Gray, D. E. McClelland
„A new topology for the control of complex interferometers“
Class. Quantum Grav. **23**, S267 (2006).
- [69] J. Mizuno, K.A. Strain, P.G. Nelson, J.M. Chen, R. Schilling, A. Rüdiger, W. Winkler and K. Danzmann
„Resonant sideband extraction: a new configuration for interferometric gravitational wave detectors“
Phys. Lett. A **175**, 273 (1993).
- [70] A. Weinstein
„Advanced LIGO optical configuration and prototyping effort“
Class. Quantum Grav. **19**, 1575 (2002).

Acknowledgements

In the last couple of lines of this thesis I would like to express my gratitude to a number of people who contributed to this work in various ways.

First of all I would like to thank Prof. Roman Schnabel for his dedicated support for all those years. I hope that future generations of students will benefit from his exceptional commitment as well as I did.

I guess everyone who had the opportunity to work at the Albert Einstein Institute Hannover agrees that it is hard to find a better place to do research. I really enjoyed being part of it, and I would like to thank Prof. Karsten Danzmann for the enormous amount of work he put into it to create this place.

I would also like to thank Prof. Kenneth Strain for giving me the opportunity to work in his team at the Institute of Gravitational Research of the University of Glasgow.

A special thanks goes out to the people I have worked with in the laboratory. These include Daniel Friedrich, Michael Britzger, Dr. Bryan Barr, Matt Edgar, Jonathan Hallam and John Nelson.

Over the years a lot of help came from Dr. André Thüring, Nico Lastzka, Dr. Henning Vahlbruch, Boris Hage, Moritz Mehmet, Dr. Simon Chelkowski, Dr. Frank Seifert and Dr. Andreas Freise. Thank you all not only for the countless helpful advices but also for the fun we had working together.

I want to thank my parents and my sister Tanja for their endless support.

Finally I would like to thank Catharina for motivation, patience and love.

Curriculum vitae

Oliver Burmeister
Kortumstr. 6
30171 Hannover

Born on May 26th, 1978 in Hannover, Germany

University studies

- 04/2005 - 10/2009 Scientific Assistant,
Albert-Einstein Institute Hannover
- 04/2005 - 01/2010 Doctoral studies in Physics, Universität Hannover
- 01/2005 Diploma thesis, Universität Hannover,
Fabry-Perot Resonatoren mit diffraktiven Einkopplern
- 10/1998 - 01/2005 Physics studies, Universität Hannover

Military service

09/1997 - 06/1998 Military service. Sanitätsregiment 1, Hildesheim

Education

1997 Abitur, Gymnasium Sarstedt

Publications

— 2004 —

- 1 | A. Bunkowski, O. Burmeister, P. Beyersdorf, K. Danzmann, R. Schnabel, T. Clausnitzer, E.-B. Kley, A. Tünnermann
„Low-loss grating for coupling to a high-finesse cavity“
Opt. Lett. **29**, 2342 (2004).

— 2005 —

- 2 | O. Burmeister
„Fabry-Perot Resonatoren mit diffraktiven Einkopplern“
Diploma Thesis, Universität Hannover (2005).
- 3 | A. Bunkowski, O. Burmeister, K. Danzmann, R. Schnabel
„Input-Output relations for a three-port grating coupled Fabry-Perot cavity“
Opt. Lett. **30**, 1183 (2005).
- 4 | T. Clausnitzer, E.-B. Kley, A. Tünnermann, A. Bunkowski, O. Burmeister, K. Danzmann, R. Schnabel, A. Duparre, S. Gliech
„Low-loss gratings for next-generation gravitational wave detectors“
Proc. SPIE **5870**, 154 (2005).
- 5 | T. Clausnitzer, E.-B. Kley, A. Tünnermann, A. Bunkowski, O. Burmeister, K. Danzmann, R. Schnabel, S. Gliech, and A. Duparré
„Ultra low-loss low-efficiency diffraction gratings“
Opt. Exp. **13**, 4370, (2005).

— 2006 —

- 6 | R. Schnabel, A. Bunkowski, O. Burmeister, K. Danzmann
„Three-port beam splitters-combiners for interferometer applications“
Opt. Lett. **31**, 658 (2006).
- 7 | A. Bunkowski, O. Burmeister, K. Danzmann, R. Schnabel, T. Clausnitzer, E.-B. Kley, A. Tünnermann

- „Diffractive Optics for Gravitational Wave Detectors“*
Journal of Physics, Conference Series **32**, 333 (2006).
- 8 | A. Bunkowski, O. Burmeister, K. Danzmann, R. Schnabel, T. Clausnitzer, E.-B. Kley, A. Tünnermann
„Optical Characterization of ultra-high diffraction efficiency gratings“
Appl. Opt **45**, 23 5795 (2006).
- 9 | A. Bunkowski, O. Burmeister, K. Danzmann, R. Schnabel, T. Clausnitzer, E.-B. Kley, A. Tünnermann
„Demonstration of three-port grating phase relations“
Opt. Lett. **31**, 2384 (2006).
- 10 | A. Bunkowski, O. Burmeister, D. Friedrich, K. Danzmann, R. Schnabel
„High reflectivity grating waveguide coatings for 1064 nm“
Class. Quantum Grav. **23**, 7297, (2006).

— 2007 —

- 11 | B. Abott, . . . , O. Burmeister, . . . , H. zur Mühlen
„Search for gravitational wave radiation associated with the pulsating tail of the SGR 1806-20 hyperflare of 27 December 2004 using LIGO“ Phys. Rev. D **76**, 062003 (2007)
- 12 | B. Abott, . . . , O. Burmeister, . . . , J. Zweizig
„Searching for a stochastic background of gravitational waves with the laser interferometer gravitational-wave observatory“
Astrophysical Journal **659**, 918 (2007).
- 13 | O. Burmeister, D. Friedrich, A. Bunkowski, K. Danzmann, R. Schnabel, T. Clausnitzer, S. Fahr, E.-B. Kley, A. Tünnermann
„Interferometry with gratings“
Conference Proceeding (Rencontres de Moriond Gravitational Waves and Experimental Gravity, La Thuile, Val d’Aosta, Italy, March 11-18, 2007).
- 14 | B. Abott, . . . , O. Burmeister, . . . , J. Zweizig
„First cross-correlation analysis of interferometric and resonant-bar gravitational-wave data for stochastic backgrounds“
Phys. Rev. D **76**, 022001 (2007).
- 15 | B. Abott, . . . , O. Burmeister, . . . , J. Zweizig
„Upper limits on gravitational wave emission from 78 radio pulsars“
Phys. Rev. D **76**, 042001 (2007).
- 16 | B. Abott, . . . , O. Burmeister, . . . , J. Zweizig
„Upper limit map of a background of gravitational waves“
Phys. Rev. D **76**, 082003 (2007).

- 17 | B. Abbott, . . . , O. Burmeister, . . . , J. Zweizig
 „Searches for periodic gravitational waves from unknown isolated sources and Scorpius X-1: Results from the second LIGO science run“ Phys. Rev. D **76**, 082001 (2007).
- 18 | B. Abbott, . . . , O. Burmeister, . . . , J. Zweizig
 „Search for gravitational-wave bursts in LIGO data from the fourth science run“
 Class. Quantum Grav. **23**, 5343 (2007).

— 2008 —

- 19 | D. Friedrich, O. Burmeister, M. Britzger, A. Bunkowski, T. Clausnitzer, S. Fahr, E.-B. Kley, A. Tünnermann, K. Danzmann, R. Schnabel
 „Power-recycled michelson interferometer with a 50/50 grating beam splitter“
 J. Phys.: Conf. Ser., **122**, 012018 (2008).
- 20 | L. Baggio, . . . , O. Burmeister, . . . , J. Zweizig
 „A joint search for gravitational wave bursts with AURIGA and LIGO“
 Class. Quantum Grav. **25**, 095004 (2008).
- 21 | D. Friedrich, O. Burmeister, A. Bunkowski, T. Clausnitzer, S. Fahr, E.-B. Kley, A. Tünnermann, K. Danzmann, R. Schnabel
 „Diffractive beam splitter characterization via a power-recycled interferometer“
 Opt. Lett. **33**, 101 (2008).
- 22 | B. Abbott, . . . , O. Burmeister, . . . , J. Zweizig
 „All-sky search for periodic gravitational waves in LIGO S4 data“
 Phys. Rev. D **77**, 022001 (2008).
- 23 | F. Brückner, T. Clausnitzer, O. Burmeister, D. Friedrich, E.-B. Kley, K. Danzmann, A. Tünnermann, R. Schnabel
 „100% reflectivity from a monolithic dielectric microstructured surface“
 Proc. SPIE **6883**, 68830X (2008).
- 24 | F. Brückner, T. Clausnitzer, O. Burmeister, D. Friedrich, E.-B. Kley, K. Danzmann, A. Tünnermann, R. Schnabel
 „Monolithic dielectric surfaces as new low-loss light-matter interfaces“
 Opt. Lett. **33**, 264 (2008).
- 25 | B. Abbott, . . . , O. Burmeister, . . . , J. Zweizig
 „Search for gravitational waves associated with 39 gamma-ray bursts using data from the second, third, and fourth LIGO runs“
 Phys. Rev. D **77**, 062004 (2008).
- 26 | B. Abbott, . . . , O. Burmeister, . . . , J. Zweizig
 „Search for gravitational waves from binary inspirals in S3 and S4 LIGO data“
 Phys. Rev. D **77**, 062002 (2008).

- 27 | L. Baggio, . . . , O. Burmeister, . . . , J. Zweizig
 „A joint search for gravitational wave bursts with AURIGA and LIGO“
 Class. and Quantum Grav. **25**, 095004 (2008).
- 28 | B. Abbott, . . . , O. Burmeister, . . . , M. Yvert
 „Astrophysically triggered searches for gravitational waves: status and prospects“
 Class. Quantum Grav. **25**, 114051 (2008).
- 29 | B. Abbott, . . . , O. Burmeister, . . . , J. Zweizig
 „Implications for the origin of GRB 070201 from LIGO observations“
 Astrophysical Journal **681**, 1419 (2008).
- 30 | B. Abbott, . . . , O. Burmeister, . . . , J. Zweizig
 „Search of S3 LIGO data for gravitational wave signals from spinning black hole and
 neutron star binary inspirals“
 Phys. Rev. D **78**, 042002 (2008).
- 31 | B. Abbott, . . . , O. Burmeister, . . . , J. Zweizig
 „Beating the spin-down limit on gravitational wave emission from the Crab pulsar“
 Astrophysical Journal Letters **683**, L45 (2008).
- 32 | B. Abbott, . . . , O. Burmeister, . . . , J. Zweizig
 „Search for Gravitational-Wave Bursts from Soft Gamma Repeaters“
 Phys. Rev. Lett. **101**, 211102 (2008).
- 33 | B. Abbott, . . . , O. Burmeister, . . . , J. Zweizig
 „First joint search for gravitational-wave bursts in LIGO and GEO 600 data“
 Class. Quantum Grav. **25**, 245008 (2008).

— 2009 —

- 34 | B. Abbott, . . . , O. Burmeister, . . . , J. Zweizig
 „All-sky LIGO search for periodic gravitational waves in the early fifth-science-run data“
 Phys. Rev. Lett. **102**, 111102 (2009).
- 35 | B. Abbott, . . . , O. Burmeister, . . . , J. Zweizig
 „An upper limit on the stochastic gravitational-wave background of cosmological origin“
 Nature **460**, 990 (2009).
- 36 | B. Abbott, . . . , O. Burmeister, . . . , J. Zweizig
 „LIGO: the Laser Interferometer Gravitational-Wave Observatory“
 Reports on Progress in Physics **72**, 076901 (2009).
- 37 | B. Abbott, . . . , O. Burmeister, . . . , J. Zweizig
 „Observation of a kilogram-scale oscillator near its quantum ground state“
 New Journal of Physics **11**, 073032 (2009).

- 38 | B. Abbott, . . . , O. Burmeister, . . . , J. Zweizig
„Search for gravitational waves from low mass binary coalescences in the first year of LIGO’s S5 data“
Phys. Rev. D **79**, 122001 (2009).
- 39 | B. Abbott, . . . , O. Burmeister, . . . , J. Zweizig
„Stacked Search for Gravitational Waves from the 2006 SGR 1900+14 Storm“
Astrophysical Journal Letters **701**, L68 (2009).
- 40 | F. Brückner, D. Friedrich, T. Clausnitzer, O. Burmeister, M. Britzger, E.-B. Kley, K. Danzmann, A. Tünnermann, R. Schnabel
„Demonstration of a cavity coupler based on a resonant waveguide grating“
Opt. Exp. **17**, 163 (2009).
- 41 | B. Abbott, . . . , O. Burmeister, . . . , J. Zweizig
„The Einstein@Home search for periodic gravitational waves in LIGO S4 data“
Phys. Rev. D **79**, 042003 (2009).
- 42 | J. Hallam, S. Chelkowski, A. Freise, S. Hild, B. Barr, K. A. Strain, O. Burmeister, R. Schnabel
„Coupling of lateral grating displacement to the output ports of a diffractive Fabry–Perot cavity“
J. Opt. A: Pure Appl. Opt. **11**, 085502 (2009).
- 43 | M. P. Edgar, B. W. Barr, J. Nelson, M. V. Plissi, K. A. Strain, O. Burmeister, M. Britzger, K. Danzmann, R. Schnabel, T. Clausnitzer, F. Brückner, E.-B. Kley, A. Tünnermann
„Experimental demonstration of a suspended diffractively coupled optical cavity“
Opt. Lett. **34**, 3184 (2009).